Paleocosmology: Observational Constraints on the Evolution of Galaxies and Large-Scale Structure

by

Eric James Gaidos

Submitted to the Department of Physics
in partial fulfillment of the requirements for the degree of

Doctorate of Philosophy

at the

MASSACHUSETTS INSTITUTE OF TECHNOLOGY

May 1996

Author . . . . . .
Department of Physics
May 23, 1996

Certified by . . . . . .
Claude R. Canizares
Professor
Thesis Supervisor

Accepted by . . . . . .

Paleocosmology: Observational Constraints on the Evolution of Galaxies and Large-Scale Structure

by

Eric James Gaidos

Submitted to the Department of Physics
on May 23, 1996, in partial fulfillment of the
requirements for the degree of
Doctorate of Philosophy

Abstract

The study of galaxies and their clustering is important to understanding their formation and evolution but also to place constraints on cosmological models. I present two surveys and their analyses: The first is an optical CCD imaging survey of 67 Abell clusters to determine the distribution of luminosities and morphologies of the constituent galaxies. A composite luminosity function constructed from the photometric data is well described by a Schechter function with a faint-end slope $\alpha = 1.09 \pm 0.08$ and characteristic absolute magnitude $M_R^* = -21.13 \pm 0.11 + 5 \log h$. A systematic brightening of M^* with higher cluster redshift and/or cluster density is observed. The data suggests an excess over the best-fit Schechter LF at $M_R > -16.5$. The form of the LF found here is in good agreement with field surveys but conflicts with recent claims for a steep LF in clusters. My photometry of Brightest Cluster Galaxies finds a dispersion of 0.06 magnitudes about a secular trend with redshift. The luminosity evolution is more consistent with models with a flat IMF (giant dominated), but a larger photometric sample is needed to substantiate this. I distinguish between disk and spheroidal galaxies using the moments of the surface brightness profiles and estimate the fraction of disk galaxies. The mean fraction is approximately 30% and shows a significant increase in clusters with $z > 0.2$, consistent with the Butcher-Oemler effect. The second survey is an on-going search for X-ray emitting galaxy clusters in archival Einstein IPC images that includes a multi-aperture source detection routine. An algorithm is developed to quantify the certainty of source extent and select X-ray cluster candidates. The surface density of bright X-ray clusters on the sky is consistent with results from the *Rosat* All Sky Survey, although the numbers involved are very small. I present an analysis of CCD imaging follow-up to an X-ray source that appears to be a cluster at a redshift of about 0.3.

Thesis Supervisor: Claude R. Canizares
Title: Professor

ACKNOWLEDGMENTS

I wish to express my sincere thanks to Prof. Claude Canizares, my Thesis Committee Chairman, as well as Prof. John Huchra and Prof. Samir Mathur for their assistance as well as patience in the completion of this thesis. Profs. Charles Steidel and John Tonry provided invaluable advice throughout the course of the project. Thanks go to Prof. Paul Schechter who was daring enough to give a young engineer a crack at astronomy five years ago. The MDM Observatory Time Allocation Committee was very generous in its allotment of telescope time to this thesis project. This project also benefited enormously from the many software packages and databases maintained on the Internet and the many kind people who assisted me in using them. Finally, a most heart-felt thank you to family and friends who supported me both emotionally and intellectually on the long and winding road to a Ph.D; this thesis is dedicated to you.

"...And whether you perceive it or not,
no doubt the Universe is unfolding as it should..."

– Max Ehrmann, *Desiderata*

A NERVOUS REX

Contents

List of Figures

List of Tables

Chapter 1

Galaxies: The Most Ancient of Fossils

The discipline of extragalactic astronomy resembles paleontology and anthropology in that one of its principle concerns is the study of the evolution of populations over periods of time vastly exceeding the human life span. And like those other sciences, it relies on the existence of two kinds of "fossil records" to overcome this obstacle: The first is the ability to observe distant objects directly as they once were (in astronomy, due to the finite speed of light) and compare these with objects at the present epoch which one presumes to be their descendents. The second record is the set of those characteristics of present objects which have preserved information about their formation and evolution. And in a similar fashion these records have their limitations: In the former it is necessary to connect the distant, young objects with nearby, older counterparts; in the latter one must infer past events from limited information in the present.

Galaxies are the observable and innumerable denizens of the Cosmos. They are the gravitationally bound objects in which most of the star formation in the Universe takes place, where heavy-element nucleosynthesis occurs, and where the metal-enriched gas is converted into interesting and complex things like planets and Life and astronomers. They have also existed for most of the estimated age of the Universe; from nuclear chronology and stellar age estimates, our Galaxy is at least 10 Gyr old, and some of its associated globular cluster system at least 12 Gyr old (Scully & Olive 1995; Bolte 1992).

The masses and luminosities of galaxies extend over a range of nearly five orders of magnitude: A galaxy such as our own Milky Way has a mass in excess of 5×10^{11} solar masses (Little & Tremaine 1987) and shines with the light of nearly 10^{10} Suns or 3.8×10^{43} ergs sec^{-1} (Binney & Tremaine 1987). The mean space density of galaxies is about one per cubic mega-parsec (Mpc^3). With photographic plates on the 100 inch Mount Wilson telescope, Edwin Hubble was able to detect galaxies to an apparent red magnitude of about 17 or an equivalent flux level of 2.7×10^{-12} ergs sec^{-1}cm^{-2} and distances of about 300 Mpc. Now, with a little effort (and a 10 meter telescope equipped with solid-state detectors on a Hawaiian mountain-top), one can observe galaxies more than an order of magnitude more distant and at flux levels lower by four orders of magnitude. At this apparent magnitude limit, the density of galaxies on the sky is 7×10^5 deg^{-2} and, in principle, 3×10^{10} galaxies are observable (Smail *et al.* 1995). By observing to cosmologically significant distances and look-back times approaching their estimated ages, we observe galaxies as they were in their youth or even birth (Steidel *et al.* 1996). The numbers of brighter galaxies for which more detailed information such as redshifts and morphologies can be has obtained has also grown. Surveys of nearby galaxies now routinely include thousands of objects (Loveday *et al.* 1992; Marzke *et al.* 1994; Ellis *et al.* 1995; Santiago *et al.* 1996; Lin *et al.* 1996). With such large numbers one can describe galaxies in a statistical fashion, and hope to tease out clues to their origin and evolution as a population even if the life stories of individual galaxies remain unclear.

Since Hubble's publication of *The Realm of the Nebulae* in 1929, in which the observational evidence was presented showing that these "nebulae" were indeed galaxies like our own, the basic questions have centered around the determination of

- The epoch of galaxy formation;
- The processes which gave rised to the great variety of luminosities, morphologies, and constituent stellar populations of galaxies; and
- The relative effects of the initial conditions at the time of formation ("nature"), and the environment of galaxies at later times ("nurture").

The study of the formation and evolution of galaxies (including that of our own) is itself evolving very rapidly and recent, comprehensive reviews are scarce. For a picture of the observational status of the field I suggest the contributions in Thronson & Shull (1992) and the review paper of Koo & Kron (1992). For theoretical fare, the lecture notes of White (1993) are highly recommended. While there is no substitute for the detailed study of individual galaxies, particularly at high redshift, a time-honored approach has been to study galaxies in a statistical fashion as a population or set of populations. This is motivated by the optimistic conviction that although these objects may be the product of a random formation process, the statistics of that process are well defined and contain important information about both galaxy formation and cosmology. In this thesis, as well as in this branch of study, the galaxies of interest are so-called 'normal' galaxies which do not exhibit signs of extraordinary behavior such as an intense starbursts or the activity of a central nucleus or black hole.

A first order description of galaxies is their luminosity and their number distribution with luminosity is called a "luminosity function" (LF). Luminosity is a complicated convolution of the total mass of stars in the galaxy, the star formation history, and the distribution of forming stars with mass (called the Initial Mass Function or IMF), and it means different things for different types of galaxies. The light of early-type elliptical galaxies and the bulges of disk galaxies, in which significant star formation is absent at the present epoch, is dominated by evolved stars who have left the main sequence and give these objects their characteristic redder colors. The luminosity of late-type disk or irregular galaxies arises in large degree from the blue, short-lived O, B, and A stars at the massive end of the main sequence, causing these galaxies to be bluer and their luminosities highly dependent on the star formation rate. While an exact interpretation of luminosity is somewhat ambiguous, it exhibits a strong correlation with the depth of a galaxy's gravitational potential well and therefore its mass, as measured by the stellar velocity dispersion (in elliptical galaxies) (Faber & Jackson 1976) or the circular velocities of neutral hydrogen (in spiral galaxies) (Tully & Fisher 1977), and in both cases being closely proportional

to the fourth power of the velocity. Luminosity is also a relatively simple quantity to measure.

To orient the reader in the succeeding discussions, I encapsulate the observational "facts of life" about galaxy luminosities and morphologies in the following statements:

- Low-luminosity (dwarf) galaxies are more numerous than high-luminosity (giant) galaxies;
- Galaxies much more luminous than a certain cut-off value ($\sim 10^{10} L_{\odot}$) are exceedingly rare;
- Galaxies with different morphologies do not have the same LF;
- Relative representation among the different morphological types varies with the local galaxy density: Elliptical galaxies are more numerous in very dense areas and spirals more numerous in the mean field;
- Concentrations of gravitationally bound galaxies, called galaxy clusters, are the unique home to Brightest Cluster Galaxies, a distinct class of ultraluminous ($\sim 10^{11} - 10^{12} L_{\odot}$) giant elliptical galaxy, sometimes possessing an extended halo.

As I shall show, measurements of the luminosities and morphologies of galaxies, particularly in dense clusters of galaxies, can play a fundamental role in deciphering the mechanisms responsible for these galaxy properties.

1.1 Luminosities & Morphologies as Artifacts...

Any viable theory of galaxy formation and evolution must be able to reproduce the essential characteristics of the galaxy LF, its dependence on galaxy morphology, and its variation with environment. For the interested reader, some details of the theory

of galaxy formation and evolution as they relate to luminosities and morphologies, as well as the relevant references, appear in Appendix A.

The standard theories of galaxy formation propose that the formation of structure in the Universe has proceeded hierarchically and has been dominated by a dissipationless or nearly-dissipationless "dark matter" component which forms gravitationally bound structures or "halos" on larger and larger scales with time. Galaxies are formed when baryonic gas is able to fall into these halos and cool faster than shock heating and pressure are able to bring it to hydrostatic equilibrium (White & Rees 1978). This scenario can be tuned to predict a maximum mass (and luminosity) to galaxies that is consistent with observations, but it also predicts that the galaxies will form at the smallest size possible, in conflict with observations. To salvage this, one theory incorporates feedback from star formation in the form of energy input from the supernovae explosions of a first generation of massive stars (White & Rees 1978). This still predicts a large number of faint galaxies relative to bright ones, such that the slope of the LF is steep.

A second theory prevents the early formation of too many dwarf galaxies by supposing a pre-heating and subsequent adiabatic cooling of the intergalactic medium such that halos can only 'trap' gas when the equivalent temperatures of their gravitational potential wells are 'hotter' than the IGM (Blanchard *et al.* 1992). A flatter LF is produced in this scenario. Thus measurements of the LF slope could be used to rule out one or both of these theories.

The theory must also be consistent with the observed evolution (or lack of evolution) of galaxies. The luminosity evolution of galaxies is divided into two components: The *passive* evolution of the original stellar population as it ages and *active* evolution due to additional star formation, merging with other galaxies, or accretion of satellite galaxies. Passive evolution will make galaxies appear brighter with increasing redshift, whereas merging or accretion will make them appear fainter. Star formation taking place more than $\sim$ 100 Myr (the main-sequence lifetimes of massive stars) in the past will make galaxies appear brighter. Since it is impossible to identify exact distant counterparts to the ancestral states of galaxies at the present epoch, the

evolution of the population as a whole must be examined statistically through the use of a LF. Passive and active evolution of the galaxies will appear as a systematic shift of the entire LF with redshift and a measurable brightening or fading in the cut-off luminosity. Merging, which will deplete faint galaxies and supply brighter ones, can also distort the shape of the LF.

The theory must also be able to provide a plausible explanation for the existence of the extraordinarily luminous Brightest Cluster Galaxies. These objects are giant, elliptical galaxies, often with highly flattened outer isophotes that appear to lie at or near the bottom of the gravitational potential well of the host galaxy cluster; Some have multiple nuclei and others have giant outer envelopes (Tonry 1987; Schombert 1988). If BCGs formed by some special process involving the collapse of the galaxy cluster core at a very early epoch then presumably their luminosity would be independent of the state of the cluster at the observed epoch. If BCGs evolve by cannibalizing giant galaxies which spiral to the cluster core under the influence of dynamical friction (Ostriker & Hausman 1977; Hausman & Ostriker 1978), or by a rain of debris from the collisions of galaxies higher in the cluster potential (Malumuth & Richstone 1984), a correlation with global cluster properties would be expected, i.e., one would expect to see less luminous prototypes in younger clusters . However, the BCGs may asymptote to some final state where the core of the cluster has essentially been depleted of galaxies able to merge with the BCG and the monster, gorged, evolves quiescently thereafter (Merritt 1985).

There are essentially two competing theories for the origin of morphological types (the 'Hubble sequence'). The 'nature ' hypothesis holds that differences in the initial density fluctuation field around galaxies led to variations in the angular momentum of the cooling gas. Low angular momentum gas went into the formation of spheroidal systems while high angular momentum material formed disks. The 'nurture' hypothesis proposes that elliptical galaxies form from the collision and merger of disk galaxies. These theories are not exclusive and may, in fact, both be true to some degree. The contrast in morphological types is most pronounced between dense clusters, where gas-poor early-type elliptical and S0 galaxies predominate, and the

mean field, where the gas-rich late-type spiral and irregular galaxies are in the majority. This observation does not discriminate between these two theories since both the initial conditions and the present-day environment of galaxy clusters is different. However, one can differentiate between the two if the clusters could be 'age-dated' by other observations. If environment plays a dominant role, youthful clusters would have a higher fraction of late-type galaxies than older clusters.

1.2 ...AND AS TOOLS

The luminosity function (LF) is not only a testable prediction of galaxy formation and evolution theories, it is an important observational tool: The integrated LF is the mean cosmic luminosity density ρ_L, which, when multiplied by a mass-to-light ratio of choice gives the fractional baryonic mass contribution to the critical closure density;

$$\Omega_B \sim 0.0027 h^{-2} \frac{(M/L)_\odot}{5} \frac{\rho_L}{1.9 \times 10^8 L\odot Mpc^{-3}} \tag{1.1}$$

which, for example, can be compared to constraints from primordial nucleosynthesis.

The LF has played a central role in the debate over the interpretation of counts of galaxies to faint magnitudes and the "faint blue galaxy problem". Blue-band number counts fainter than $B \sim 19$ reveal a population of objects with an inferred co-moving number density 3-5 times that of the galaxies of the present epoch (Peterson *et al.* 1979; Tyson 1988; Jones *et al.* 1991). Paradoxically, the redshift distribution in deep surveys is consistent with little or no evolution (Colless *et al.* 1990; Glazebrook *et al.* 1995) and samples of high-redshift luminous galaxies show little evolution in either counts or luminosity (Steidel *et al.* 1994). This has led to proposals that a high co-moving number density of more rapidly evolving dwarf galaxies is responsible for the excess in counts, a population that would manifest itself as a steep "faint end" in the galaxy luminosity function (Koo *et al.* 1993; Treyer & Silk 1994; Gronwall & Koo 1995). This possibility has in part motivated attempts to extend measurements of the LF to very low luminosity levels.

At the other extreme, the observation that the intrinsic luminosities of the first-

ranked or Brightest Cluster Galaxies in clusters are extremely homogeneous, with a dispersion of about 0.25 magnitudes (Humason *et al.* 1956) has led to their use as astronomical 'standard candles' for the purpose of distance measurement (Postman & Lauer 1995), tests of world models (Schneider *et al.* 1983a), and the measurement of peculiar velocities (Lauer & Postman 1994). If somehow the homogeneity of BCG luminosities could be understood, and the effects of merging discounted or accounted for, observations of BCGs to high redshift could be a powerful test of combined models of cosmology and stellar evolution. Along the same lines, evidence for the uniformity and quiescent evolution of elliptical galaxies in clusters is now being considered for similar tests (Pahre *et al.* 1996).

1.3 Techniques & Previous Research

1.3.1 Luminosities

In astronomy luminosity is usually expressed as an *absolute magnitude* M in the wavelength pass-band of the observations

$$M = -2.5 \log L + M_{\odot}, \tag{1.2}$$

where L is the luminosity in solar units and $M_{\odot}$ is the absolute magnitude of the Sun in the observed range of wavelengths. For a 'red' ($\lambda \sim 7000\mathring{A}$) magnitude, $M_R = +4.3$. The most systematic method of measuring the luminosity of galaxies is to measure their flux (expressed as an apparent magnitude m) and their recessional velocity cz, and calculate a rest-frame absolute magnitude using one's favorite description of space-time. In a Robertson-Walker Universe,

$$M = m - 5 \log \left(\frac{q_0 z + (q_0 - 1)\left(\sqrt{1 + 2q_0 z} - 1\right)}{h q_0} \right) + 42.39 - K \tag{1.3}$$

where h is the Hubble constant in units of 100 km sec^{-1} Mpc^{-1}, q_0 is the deceleration parameter (specified by the cosmology, i.e. $q_0 = \Omega/2 - \Lambda$), and K is the "K-correction"

which accounts for the narrowing of the pass-band in the galaxy rest-frame and rest-shifting of the source spectrum with respect to the observed band; it is almost always a positive quantity.

Upon acquiring the absolute magnitudes of the desired number of galaxies in a survey over a given region of the sky, a LF, $\phi(M)$, is constructed by weighting each galaxy by the volume of space in which it could have been detected: If the ith galaxy in the absolute magnitude interval $M \rightarrow M + dM$ could have been detected to a redshift z_i over a solid angle $\Omega_i(z)$

$$\phi(M)dM = (3000Mpc)^{-3} \times h^3 \Sigma_i \left(\int_0^{z_i} dz \Omega_i(z) \frac{\left[q_0 z + (q_0 - 1)\left(\sqrt{1+2q_0 z} - 1\right)\right]^2}{q_0^4 (1+z)^3 \sqrt{1+2q_0 z}} \right)^{-1} \tag{1.4}$$

Many different methods are actually used to construct luminosity functions but this expression conveys the essential mathematics. This and similar operations can be performed on redshift surveys to find the local LF (Sandage *et al.* 1979; Efstathiou *et al.* 1988), or, if one is more ambitious, on deeper surveys to find the evolution of LF with redshift (Eales 1993).

Beyond the monumental task of acquiring magnitudes and redshifts of a sufficient number of galaxies to adequately sample the luminosity function, there are potential pitfalls in the standard technique of LF construction. These arise from a combination of the apparent magnitude limit of the surveys and their unrestricted depth. Two of the most important can be elucidated by a careful inspection of Eqn. 1.4. In magnitude-limited surveys the most luminous galaxies can be seen to much larger distances than the least. An interesting range of galaxy luminosities over which to construct $\phi(M)$ is ~ 5 magnitudes, a factor of 100, for which the corresponding ratio of Euclidean volumes is 10^3. The sampling of low-luminosity galaxies, which can be detected only in a much smaller regions of space, suffers from larger Poisson noise. Furthermore, the sampling becomes sensitive to variations in the galaxy density (large-scale structure). For example, if an observer inhabiting a region of low mean density were to construct a LF, this intrepid astronomer would mistakenly find

disproportionally fewer dwarf galaxies compared to giant galaxies, which are sampled from a larger, more "fair" volume.

Secondly, galaxies are seen against a noisy background due to the brightness of the night sky and the intrinsic noise of the detector. They are thus detected and selected not just on the basis of a total integrated flux, but according to surface brightness as well. Low surface brightness (LSB) galaxies are more difficult to detect and even more difficult to obtain accurate magnitudes and redshifts for. The effect is redshift-dependent due to cosmological dimming and K-corrections, and thus the same galaxy population may not be observed over the entire depth of a survey. Galaxies with anomalously low surface brightnesses but respectable luminosities have been discovered (McGaugh *et al.* 1995) but their space densities appear to be small relative to their brighter counterparts and their importance is debatable. Still, one can still argue that volume and surface brightness biases make for significant uncertainties in present field galaxy LFs (Driver & Phillips 1996).

There are other, as yet unquantified systematics as well. For example, positive luminosity evolution combined with the volume bias will cause the most luminous galaxies in a magnitude-limited survey to be too bright, effectively "stretching" the LF. Galaxies of different rest-frame spectra will suffer different K-corrections, which can induce significant errors if the spectra, especially the ultraviolet spectra which are red-shifted into the observed rest-frame, are not well known enough to make an accurate correction. All these systematics become more serious with increasing redshift.

A complentary scheme to construct the LF, pioneered by Abell, e.g., (Mottmann & Abell 1977), is to exploit the highly non-uniform distribution of galaxies in space and survey the densest concentrations of galaxies, called galaxy "clusters". These clusters are typically a factor of $\sim 10^3$ denser than the cosmological mean over a volume of a few Mpc^3. They create a significant projected surface density of galaxies on the sky despite intervening distances of hundreds of Mpc. The ratio of the size of clusters ($\sim$ 10 Mpc) to their distances ($\sim$ 500 Mpc) is small, meaning that errors in luminosity of at most a few percent occur by assuming the galaxies are all at the

same distance. The high projected surface density also permits efficient imaging and photometry of a large number of galaxies in a limited field of view. Moreover, the galaxies are all observed at the same rest-frame surface brightness limit modulus their different K-corrections. If the redshift of the cluster is known, galaxy luminosities can then be calculated using Eqn. 1.3 in a kind of "poor man's redshift survey".

Of course, without spectroscopy to confirm the redshifts of individual galaxies, it is impossible to be certain whether any particular galaxy is a member of the cluster or a field galaxy projected along the line of sight. However, it is possible to measure the *statistical* distribution of galaxies with some measured property (such as luminosity) by subtracting the mean contribution of background galaxies. The brightest galaxies associated with the nearer clusters are nearly all cluster members because of the relatively low numbers of field galaxies at the same apparent magnitude. However, the background contribution is significant and must be carefully estimated in the case of more distant clusters and their lower-luminosity members.

It is also important to point out that, without an independent measure of the total projected overdensity along the cluster line-of-sight, it is not possible to correctly compute the normalization of the cluster LF and compare it to the field; Only the shape of the LF can be accurately determined. Although a complete treatment of the LF problem must include issues of normalization, the observational part of this thesis is concerned with a construction of the cluster LF and I do not deal with this issue further.

Parametric descriptions of the galaxy LF attempt to capture the basic elements of the distribution using simple functions and are useful in comparing between individual surveys, and between surveys and models. Abell (1962) used a broken power law to describe the abundance of faint galaxies and the limits on bright ones. Schechter (1976), inspired by the description of the mass distribution derived in Press & Schechter (1974), introduced an analytical description of the LF now commonly called the Schechter function;

$$n(L)dL \sim e^{-L/L^*} \left(\frac{L}{L^*}\right)^{\alpha} dL \tag{1.5}$$

where L^* describes a characteristic cut-off luminosity (or absolute magnitude) and α the power-law distribution of low-luminosity galaxies faint galaxies.

The Field: Hubble (Hubble 1936) constructed the first galaxy luminosity function (a Gaussian) from a small, and very biased, sample of nearby galaxies. Much more recent surveys (Kirshner *et al.* 1979; Tully 1988) and their re-analysis (Efstathiou *et al.* 1988) have found Schechter-like LFs with flat faint-end slopes ($\alpha\sim -1$). Most notable are the recent very wide field surveys which have found similar results. Using the Mt. Stromlo-Automatic Plate Machine (APM) survey of field galaxies selected from blue photographic Schmidt plates, (Loveday *et al.* 1992) found a flat distribution with $\alpha = -0.97 \pm 0.10$ to $M_B < -19$. (Marzke *et al.* 1994) also obtained $\alpha = -1.0$ for Center for Astrophysics (CfA) redshift survey galaxies over the range $-20 < M_B < -18$ but found evidence for an upturn in the LF at $-16 + 5\log h$. The reality of the latter result is difficult to ascertain due to uncertainties in the systematics of the Zwicky magnitude system used. The combined samples in the AutoFib survey (Ellis *et al.* 1995) give a $z < 0.1$ LF with $\alpha = -1.09 \pm 0.10$. An evolution of α towards steeper values at higher redshift is also claimed. Analyses of the recently completed Las Campanas Redshift Survey (LCRS) include luminosity functions constructed from subsets of the 23690 galaxies in the survey at $z \sim 0.1$ (Lin *et al.* 1996). Due to a 'dip' in the LF, this survey finds a formal best-fit slope of $\alpha = -0.70 \pm 0.05$ to $M_r < -17.5$, but the data is better described over-all by $\alpha\sim -1.0$, and a possible upturn at $M_r > -17$.

Clusters: Schechter (1976), fitting his empirical form to the photographic data of (Oemler 1974), found $\alpha = -1.25$ (with an error greater than 0.2) and $M_B^* = -19.1 \pm 0.2$. The relatively small sample sizes of typical cluster samples and the covariance between M^* and α led subsequent photographic research on the cluster LF to adopt the Schechter value for α in order to obtain a well-defined value of M^* (Dressler 1978b; Lugger 1986; Oegerle & Hoessel 1989). Derivations of the LF from photographic data of the Virgo and Fornax (Ferguson & Sandage 1988) give a steeper slope; $\alpha\sim -1.3$ and $M_B^*\sim -21$. More recent work using CCD imaging (Driver *et al.* 1994; Driver *et al.* 1994; Kashikawa *et al.* 1995; De Propris *et al.* 1995)

has found a steep faint-end or an upturn in the slope with values of α approaching -1.4 to -2. On the other hand, deep CCD imaging in nearby clusters finds either an upturn at faint absolute magnitudes well below the limits of field surveys (Bernstein *et al.* 1995), or a simple flat LF (Chiboucas *et al.* 1995).

To summarize, there is agreement among all the low-redshift surveys of field galaxies that the LF is flat ($\alpha = -1$) to an absolute magnitude of about -17. Fainter than that there may be an upturn or excess of dwarfs. In contrast *some* work on clusters finds a steep LF at much brighter magnitudes (Driver & Phillips 1996). In Fig. 1 I plot various Schechter function parameter pairs obtained for surveys of the field and clusters. This plot is intended to sketch out the playing field, and is not intended to be complete nor unbiased. All absolute magnitudes are tranformed to Gunn r magnitudes using the assumptions $B - r = 1.1$ for field galaxies, $B - r = 1.5$ for cluster galaxies, $F - r = -0.58$ for cluster galaxies, and $R - r = -0.09$ for cluster galaxies. The dashed line approximately describes the covariance between M^* and α such that points on loci parallel to this line probably describe very similar distributions.

As mentioned earlier, redshift and photometric surveys suggest little or no luminosity evolution of normal galaxies in the field to $z \sim 1$. Studies have also focused on cluster galaxies where the case for or against luminosity evolution, particularly merging at the bright end of the LF and the brightest cluster galaxy, is not so clear. The results have typically been cast in the form of the difference between M_1, the absolute magnitude of the first-ranked galaxy or BCG, and some fainter magnitude such as M_2 or M^*. Merging would make more luminous galaxies grow at the expense of less luminous ones, widening the gap between them. The effect is expected to be most pronounced at the bright end since dynamical friction, the process driving merging, is proportional to the mass of the system. Some researchers found evidence for an effect (Dressler 1978a) while others (Gunn & Tinsley 1976; Schombert 1984; Lugger 1986; Oegerle & Hoessel 1989) could not confirm this. A significant correlation with the morphology of the cluster (Rood-Sastry and Bautz-Morgan type) such that clusters with more relaxed morphologies which are supposed to be dynamically 'older'have a

brighter M_1 and fainter M^*, is now claimed by Trevese (1996). A recent CCD survey of 119 BCGs in $z < 0.05$ Abell clusters (Postman & Lauer 1995) finds no correlation with Abell richness (however, their sample only included $R < 3$ clusters).

1.3.2 MORPHOLOGIES

Although the morphologies of nearby galaxies have been differentiated in botanical detail, work on the the morphologies of large samples of more distant galaxies in both the field and clusters has lagged behind construction of luminosity functions. Until recently much of the structural classification was done by eye from photographic plates, (Dressler 1980; Schechter & Dressler 1987). Such studies made clear that elliptical and S0 galaxies (disks with old stellar populations) dominated the population of clusters. A tight correlation between local density and galaxy morphology was found (Dressler 1980), although the exact interpretation of this finding has been disputed (Whitmore *et al.* 1993). Information on more distant field and cluster samples has been restricted to colors, with blue galaxies being equated with disk galaxies and red galaxies with ellipticals. This data suggests interesting evolution in the galaxy population with redshift, including the excess of faint blue field galaxies discussed above. In galaxy clusters, the fraction of blue galaxies was found to rise dramatically above a redshift of ~ 0.2 (Butcher & Oemler 1984). Spectroscopic investigation (Dressler & Gunn 1983; Dressler *et al.* 1985) and later high-resolution imaging by HST (Dressler *et al.* 1994) suggest that a large fraction of these are disk galaxies undergoing an increased episode of star formation. It is not yet clear whether this process is somehow connected to the relative abundance of ellipticals in clusters at the present epoch.

Steps are being taken to rectify the situtation and develop schemes that can be applied to digital surface photometry, including bulge-disk deconvolution of nearby spiral galaxies (Schombert & Bothun 1987), neural-network classification (Odewahn 1995), and principal component analysis of the surface-brightness profiles (Watanabe *et al.* 1985; Han 1995). For more distant objects the schemes are split among using simple characteristics such as surface brightness and central concentration of the flux (Okamura *et al.* 1984; Doi *et al.* 1993; Abraham *et al.* 1994; Doi

et al. 1995) and, for higher-resolution data, fitting surface brightness profiles (Casertano *et al.* 1995). This field of distant galaxy classification is in its youth and has only begun to explore the possibilities opened up by Hubble Space Telescope data and large digital surveys, as well as the combination of spectral and structural information.

1.4 Motivation for this Thesis

It seems clear that there is much work to be done before a significantly better understanding of galaxy formation and evolution is in hand. An interesting contribution can be made by a more systematic survey of cluster galaxies using the wide-field CCDs now available to image tens of thousands of galaxies to high photometric precision, a primary goal being to construct a high signal-to-noise LF and measure the slope of the faint end.

Furthermore, if one can somehow "age date" these clusters using, for example, an estimate of their over-all morphology independent of the properties of the individual galaxies, a number of interesting evolutionary tests can be made, including changes in the faint-end slope, the absolute magnitude of the cut-of M^*, the relative numbers of disk galaxies, and the luminosity of BCGs. This, in true Don Quixote style, is what I have set out to do in this Thesis.

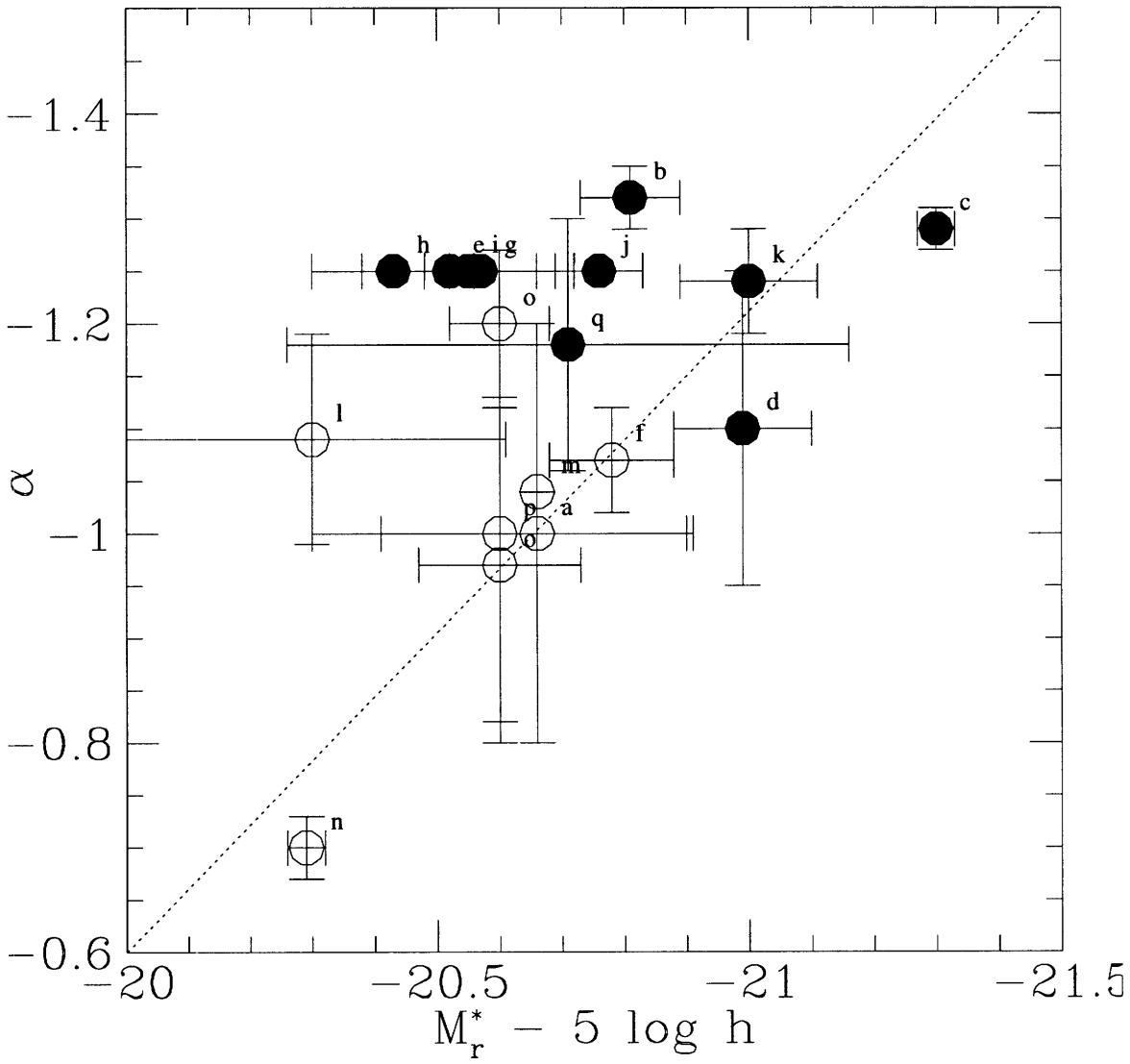

Fig. 1.— Field and Cluster LF – Schechter parameters
Schechter function parameters for field (open points) and cluster (solid points) surveys. The dashed line indicates the direction of covariance. (a) HI spirals (Tully 1988); (b-c) Fornax & Virgo (Ferguson & Sandage 1988); (d) KOS (Kirshner *et al.* 1979); (e) 3C295 (Mathieu & Spinrad 1981); (f) combined surveys (Efstathiou *et al.* 1988); (g) Abell Cl (Trevese *et al.* 1996); (h) Abell Cls (Dressler 1978a); Abell Cls (Lugger 1986); (i) Abell Cls (Oegerle & Hoessel 1989); (j) Abell Cls (Schechter 1976); (k) Autofib (Ellis *et al.* 1995); (l) APM/Stromlo (Loveday *et al.* 1992); (m); DARS (Peterson *et al.* 1986) (n) LCRS (Lin *et al.* 1996); (o) SSRS2 (Da Costa *et al.* 1994); (p) CfA (Marzke *et al.* 1994); (q) A576 (Mohr *et al.* 1996);

Chapter 2

A Wide-Field Optical Survey of Cluster Galaxies

An optical imaging survey of rich clusters of galaxies was conducted to efficiently study the distribution of a large number of member galaxies with luminosity and morphology and establish any correlation between these properties and that of the host clusters. The large number of clusters (67) in the survey and the relatively wide field surveyed in each cluster makes this a unique resource with which to undertake this research: I estimate that there are of order 10^5 cluster galaxies in the survey. In §2.1 I describe the survey and the construction of the galaxy photometry catalog. The measurement of the background field galaxy counts, crucial to a statistical determination of the galaxy luminosity function, is presented in §2.2. The global properties of the galaxy clusters, i.e., density and morphology, are discussed in §2.3. The galaxy LF for these clusters is derived and its variation with redshift and cluster properties explored in §2.4; The brightest cluster galaxies analyzed separately in §2.5. In §2.6 I introduce a new technique to characterize the surface-brightness morphologies of distant galaxies and analyze the relative distribution of disk and spheroidal systems in the clusters.

2.1 Description of the Survey and Galaxy Catalog

2.1.1 Cluster selection

The clusters were selected from the ACO catalog (Abell *et al.* 1989) containing 4076 such objects in the Northern and Southern hemispheres and essentially an extension of the original Abell catalog (Abell 1958). The Abell catalog was constructed from visually selected enhancements in the projected galaxy distribution on Palomar Observatory Sky Survey (POSS) plates of the Northern Hemisphere obtained at the Caltech 1.2 meter Schmidt telescope, and Southern Sky Survey plates taken at a similar telescope in Australia. By definition, each cluster contains at least 30 galaxies with apparent magnitudes in the range m_3 and $m_3 + 2$ (where m_3 is the magnitude of the third-ranked galaxy) in an aperture of radius 1.5 h^{-1} Mpc of the cluster center. A more complete sub-catalog of "rich" clusters with at least 50 members was also defined. Altogether, Abell defined six richness classes (0-5) in order of increasing membership. Only a small fraction of the ACO cluster have published redshifts (Struble & Rood 1991). Nearly all Abell clusters with measured redshifts lie at $z < 0.3$.

As is the case with any sample of astronomical objects selected by the human eye, the statistics and limitations of the catalog are not well understood. Without distance information, there is no one-to-one correspondence between the galaxy distribution in space and the observable; the projected surface density on the sky. Such a catalog could be contaminated by spurious sources caused by the large-scale structure of the galaxy distribution. A gravitationally bound mass of galaxies does not necessarily have to appear as a region of high surface density on the sky, and vice versa. For example, a number of less massive but more common enhancements in the space density could be (un)fortuitously aligned along a line of sight, mimicing the existence of a much more massive object. By the same token, an underdense region along the line of a genuine galaxy cluster could suppress the cluster signal and pre-

vent its detection. Most Abell clusters have no spectroscopic confirmation of being a significant overdensity in the space distribution of galaxies, nor even a measured redshift.

However, studies of the distribution of ACO clusters with richness find a sudden decrease in the their number below a galaxy count of 50, i.e., "poor" $R - 0$ clusters (Ebeling 1993). This suggests that the catalog is seriously incomplete for these objects. Clusters can also be identified by the X-ray emission from a hot intracluster medium in hydrostatic equilibrium with the gravitational potential (see Ch. III). Extensive studies of the Abell clusters detected in the All Sky Survey of the *Rosat* X-ray observatory satellite find that nearly all of the richer ($R > 0$) Abell clusters are physical objects and not the result of projection effects (Ebeling *et al.* 1993; Ebeling 1993) (see Ch III). Thus, with a few exceptions, I have included only $R > 0$ clusters with measured redshifts in my sample.

Clusters were selected with redshift to optimize the efficiency of galaxy photometry to a fixed rest-frame surface brightness. As discussed in §1.3, surface-brightness selection effects may be an important culprit in biasing number counts and redshift surveys. All other things (such as richness) being equal, distant clusters will subtend a smaller angle on the sky and thus more of their galaxies will be included in the fixed field of view of an imaging camera. However these same galaxies will have a lower observed surface brightness due to cosmological dimming and the red-shifting of the rest-frame spectra (K-correction).

I gauge the efficiency of observing cluster galaxies at a certain redshift by estimating the specific integration time required per galaxy to achieve a fixed rest-frame surface brightness limit. I assume that the density of galaxies around the cluster center decreases as the radius squared, such that their projected surface density at angle θ from the cluster center falls as θ^{-1} (Beers & Tonry 1986). In arc-second seeing, cluster galaxies will be resolved to $z \sim 0.3$, the limit of the Abell catalog and thus observing to a fixed surface brightness is sufficient to observe the same galaxy population, independent of redshift. For a fixed cluster richness, the total number of cluster galaxies will be proportional to the field of view. The cosmological surface

brightness dimming is a factor $(1+z)^{-4}$. I adopt a simple factor of $(1+z)^{-1}$ for the K-correction of elliptical galaixes (Postman & Lauer 1995),. The K-corrections of ellipticals are the largest in the chosen observing band-pass (R) and redshift range of the Abell catalog; Correcting for elliptical galaxies will result in generous over-corrections for all other galaxy types. Galaxy photometry is limited by the Poisson noise of the night sky background and the signal-to-noise of a measurement increases with the square-root of the integration time. The specific integration time per galaxy is then

$$t_{int} \sim (1+z)^{10} z^{-2}, \tag{2.1}$$

whose inverse is plotted in Fig. 1. There is a maximum at $z = 0.25$ and a broad range of suitable redshifts from $z > 0.1$. I tended to select clusters close to $z = 0.1$ to maximize the amount of spatial information availabel for the classification of galaxies (§2.6).

The sample was limited to clusters with Galactic latitudes $|b| > 30°$. No other selection criteria such as morphology were used. The selection is essentially unbiased in that I did not intentionally select clusters that have already been extensively observed. The drawback is that there is the possiblity of non-existent clusters, erroneous positions or incorrect redshifts in my sample. I obtained Charge-Coupled Device (CCD) imaging through red (5500-8000 Å) filters. This wavelength range was chosen because galaxies, particularly the elliptical galaxies that dominate the cores of clusters, emit most of their light at redder wavelengths, and the effects of redshift on galaxy spectra are small. Exposure times were generally selected to achieve a constant surface brightness limit although this is not always the case. Most of the imaging covered a 8.4 arc-minute field of view which, at $z = 0.13$, corresponds to 1 h^{-1} Mpc. Some clusters were imaged in a mosaic pattern to obtain a 16 arc-minute field of view.

2.1.2 Observations

The observations were made at the Michigan-Dartmouth-MIT Observatory using the 2.4 meter Hiltner telescope with a f/7.5 secondary. The four observing runs took place in May, 1994; September, 1994; May, 1995; and October, 1995. The first five days of the first run used a camera with a Loral 1024^2 CCD that is thinned and back-side illuminated in conjunction with a special R_s filter which has a redder and wider band-pass than a standard KPNO R interference filter. The plate scale was 0.275 arc-seconds per pixel giving a field of view of 4.6 arc-minutes. All subsequent observations used a camera with a STIS (Space Telescope Imaging Spectrograph) thick, front-side illuminated CCD with a 2048^2 format, 0.24 arc-second pixel scale, and a 8.2 arc-minute field of view. Due to the unavailabity of a larger R_s filter, an AURA R filter (similar to KPNO R) was used. Plots of the R and R_s bandpasses are shown in Fig. 1.

The weather during 6 of the 8 nights of the May 94 run was judged to be photometric based on repeatability of the measurements of standard stars and visual inspection of the sky for clouds. Twenty-two clusters were imaged under photometric conditions and they serve as the primary data for this thesis. No photometric nights occured for subsequent runs and no usable data was obtained at all during the last run (October 1995). Usable data were obtained for 67 Abell clusters. Table 1 lists the Abell clusters surveyed, giving the telescope and instrument, total field of view, and exposure time. It is also indicated whether the imaging was obtained under photometric conditions.

2.1.3 Image Processing

Raw CCD images require extensive processing to remove systematic effects and artifacts to obtain a "clean" image suitable for galaxy photometry analysis. I used the standard routines in the Image Reduction and Analysis Facility (IRAF) for this purpose.

The signal from a CCD camera is biased by an arbitrary amount sufficient to

ensure that the negative-going fluctuations from noise are not truncated. This bias level is recovered by reading each CCD column beyond the imaging area and creating an "overscan" strip. The bias level along the overscan is fit by a polynomial and subtracted from the image; the overscan region is then trimmed off.

Flat-fielding removes variations in the photometric zero-point across a CCD image. These variations arise from vignetting, obscurations by objects and dust particles in the optical path, and CCD pixel-to-pixel response variations. Images of blank fields such as screens on the inside of a telescope dome or of the twilight sky are sometimes used as flat fields to correct CCD images. However, these do not always faithfully reproduce response differences because of the effects of lighting, contaminating clouds or stars, and poor reproduction of the color of the night sky. More accurate flat fields were constructed by averaging over 20-40 images of different fields, excluding the highest few pixel values in the averaging process at each pixel. This technique relies on most of the fields being occupied by dark sky such that elimination of the few highest pixel values eliminates any contaminating objects.

Charged particles from cosmic ray and the decay of trace radioactive materials in the instrument produce spots in the CCD images with a characteristic highly peaked signal and a small footprint. In thinned CCDs the CPEs are typically elongated trails while in thick CCD's they are circular points. The CPEs accumulate on the image at a constant rate while an exposure is being made and ultimately limiting practical exposure times. CPEs coinciding with galaxy images can cause substantial photometry errors. If they are sufficiently numerous they may also make automatic determination of the image point-spread function difficult. CPE elimination is a critical step for facilitating the automatic analysis of the survey images. CPEs can be eliminated from very deep images by breaking the exposure into many multiple, shorter exposures. The events are uncorrelated from image to image and can be removed by median filtering. the exposure times used for this survey (15-40 minutes) and the time required to read out the CCD make this option impractical. Here, CPEs are removed using the COSMICRAYS routine in the NOAO package installed on IRAF. The galaxy detection and classification routines (discussed below)

are also able to descriminate against CPE events.

The COSMICRAYS routine examines each pixel which exceeds a certain threshhold above the background and compares its value to the average pixel value in a 7 $\times$ 7 box centered on the pixel in question. If the former exceeds the latter by a certain factor then the pixel is identified as a cosmic ray and its value replaced by the mean of four neighboring pixels (excluding the second highest pixel). The process can be repeated to iteratively clean all CPE-effected pixels. A smaller box reduces the effect of gradients in the image, while a larger box is required for CPEs with multiple pixels. Less stringent criteria (a smaller factor) will be more efficient at removing CPEs but may also introduce errors in the photometry, i.e., central pixels in objects may be altered. Areas of the image with steep pixel value gradients are susceptible to this effect. These will occur for point-like objects; extended objects like galaxies will always have broader profiles. The broader the point spread function with respect to the COSMICRAYS box, the lower the threshhold may be.

The minimum gradient threshhold for an image can be estimated by constructing a model PSF and evaluating the ratios of pixel value to averaged neighbor value. I modeled the PSF as a Moffatt function;

$$I(r) = \left[1 + \left(\frac{2r}{FWHM}\right)^2\right]^{\beta/2} 2^{\beta/2-1} \tag{2.2}$$

where FWHM is the full width half maximum of the PSF and β is a parameter which governs the power-law behavior of the 'wings' of the PSF. Typically, $\beta \sim 2.5$. A plot of the minimum flux ratio factor for CPEs versus the FWHM in pixels is shown in Fig. 2. A typical FWHM at the plate scale of the survey is 4 pixels. Based on these results I set the detection threshhold to 5σ and the flux ratio to 10%. Sixteen iterations were used to ensure that all pixels contaminated by CPEs were corrected.

"Bad" columns due to faulty CCD registers are removed by linear interpolation across the columns. The final step is to align and sum any multiple images of a field using the GEOMAP and GEOTRAN routines in IRAF.

2.1.4 PHOTOMETRY

Most of the observations were performed under non-photometric conditions, e.g., haze, thin cirrus or scattered clouds. In fact, reliably photometric conditions occured only for 6 of the 8 nights on the first run and never on any of the three successive runs. Nevertheless, this limited photometric data is critical for obtaining absolute magnitudes for M^*, M_1 and comparing between individual clusters and between clusters and the field galaxy photometry of other surveys.

Photometric images were calibrated using observations of standard stars (Christian *et al.* 1985). These stars are in (or in the line of sight of) globular or open clusters, which afford a sufficient number of stars for the relatively small field of view of CCD cameras. Photometric observations with each of the filter/CCD combinations were analyzed independently.

Stars are detected in the images using the DAOFIND algorithm in the the DAOPHOT package of stellar photometry tools in IRAF. This routine convolves the image with a Gaussian with 1 arc-second FWHM and finds peaks above a set threshhold. Photometry is performed on each star by counting the total counts within a 3 arc-second radius circular aperture and subtracting a fixed sky value determined by using the ITERSTAT routine (described below). The use of a global sky value for each image avoids contamination problems from adjacent stars. The 3 arc-second radius was found by trial-and-error to provide a balance between including as much of the scattered light as possible while minimizing the probability of contamination by neighboring stars.

A convenient expression of the calibration is the magnitude m_1 of a star that generates 1 DN/sec in the detector placed above the atmosphere. For the Loral CCD + R_s filter on the 2.4 meter telescope I found $m_1 = 28.95 \pm 0.05$ for a star with $B - R = 1.0$ color. There is a small but measurable color term such that m_1 increases as $0.1(B - R)$. The dissappointingly large error in the calibration possibly arises from a signficant systematic scatter in the calibration point, to which the problem of performing simple aperture photometry in the relatively crowded fields near star clusters is probably a major contributor. I observed no measurable drift in

the calibration over 5 days of of photometric observations. The calibration for the AURA R/STIS combination was found to be $m_1 = 23.00 \pm 0.05$ with no apparent color term. Note that the ~ 1 magnitude difference in response between the thinned and thick CCDs was compensated for by roughly doubling the exposure times for the latter.

The zero-point magnitude for each individual image is found using the equation:

$$m_0 = m_1 + C(B - R) - a_R z - g_R \tag{2.3}$$

where the last two terms are the atmospheric extinction through an airmass of z and the galactic extinction. Since no color information is available, I adopt a value of $B - R = 1.5$, typical of cluster ellipticals.

An extinction coefficient of 0.10 was used, intermediate between the standard KPNO R values($\sim$ 0.12) and that for the redder Thuan-Gunn r filter of 0.08 (Kent 1985). Uncertainties of up to 50% in this value are relatively unimportant since all of the photometric images were obtained through airmasses less than 1.3. While errors in a_R may produce small offsets in the absolute photometry, the errors in the relative photometry between cluster images will be less than 0.01 magnitudes. Galactic extinction is calculated using the B-band extinction values given in the NASA Extragalactic Database (NED) and multiplying these by 65% to account for the inverse dependence of extinction on optical wavelength (Lang 1980). If the value was not available from NED I adopted a value based on inspection of reddening maps (Burstein & Heiles 1982; Burstein & Heiles 1984).

Galaxy photometry is characterized by the existence of nearly as many photometry systems as there are surveys. To compare with surveys in these other systems it is necessary to find transformations between them. At red wavelengths, the Kron-Cousins R and Thuan-Gunn r pass bands are used with CCD imaging and the corresponding plate system is F magnitudes, usually converted to equivalent r_F magnitudes. The magnitudes here are in the Kron-Cousins R system and to compare with other work corrections for the different band-passes used must be made. Fortunately,

the corrections are not large; of order 10%.

Faint field galaxy counts are dominated by spirals at $z \sim 0.2 - 0.5$ while the Abell clusters are more elliptical rich and lie at about half the distance. This combination of different intrinsic spectra and different redshifts means that separate corrections should be made for the field and cluster samples (I do not attempt to tailor the corrections to the individual galaxy types within the clusters).

For field galaxies, I adopt $R_s - R = 0.14$ (Steidel & Hamilton 1993) and $R - r_F = 0.13$ (Metcalfe *et al.* 1991). The zero point of $R - r$ is estimated to be less than 0.1 magnitudes with a color term of less than 0.2 magnitudes per $B - R$ color for LCRS field galaxies (Lin *et al.* 1996). On the other hand, CCD stellar photometry (Jorgensen 1994) gives the transformation $R = r - 0.11(g-r) - 0.32 \pm 0.02$, which for a typical spiral galaxy with $g - r \sim 0.3$, gives $R - r \sim -0.35$. I assume a zero point similar to that of Lin *et. al.* (1996), but adopt the color term of (Jorgensen 1994) to correct for the redder cluster galaxies, to get $R - r = -0.09$.

Absolute magnitudes are calculated from apparent magnitudes assuming $q_0 = 0.1$ and a K-correction of the form $2.5 \log_{10}(1+z)$. The latter is used both by Lin *et. al.* (1996) for field galaxies in the LCRS survey and by Postman & Lauer (1995) for brightest cluster (elliptical) galaxies at $z < 0.5$.

2.1.5 Image Reduction

Catalogs of galaxies and basic measurements of their distribution of surface brightness were constructed from the images using the FOCAS routines developed by Valdez (NOAO, 1984). These routines consist of the detection and construction of objects, splitting objects with merged isophotes, separating stars and galaxies, and computing magnitudes and surface brightness properties. The brightest cluster galaxy (BCG), or galaxies if there were two giant ellipticals of roughly equal luminosity, were removed by isophote fitting and model subtraction. These galaxies typically have extended, low surface-brightness halos which are difficult for FOCAS to measure and which can cause it to produce spurious multiple objects. Treatment of the BCG's is discussed in §2.5.

The FOCAS DETECT routine convolves an image with a detection filter to find locations on the image where there is a significant signal level, i.e., the weighted sum of the pixel values above background exceeds the noise by a statistically significant amount. This level, set by the user but limited by the noise, is the detection isophote level. The choice of detection filter has a significant impact on the signal threshold at which different objects can be detected. A typical choice is a Gaussian with a width approximating that of the image point-spread function. The detection filter-convolved image is scanned line by line. Along each line, object "run length codes" are created by finding contiguous sections where all pixels have values above the detection threshhold. Objects are then assembled from overlapping run length codes, where diagonally adjacent pixels are considered to be overlapping. The detection threshhold, scaled to the RMS noise of the sky background, is thus a compromise between avoiding finding too many spurious objects and including more signal from each object at lower signal levels. The FOCAS routines do not, unfortunately, include special techniques to extend galaxy photometry to fainter isophote levels.

An optimal detection scheme is efficient at detecting the extended images of galaxies, is not prone to finding spurious objects from the noise background, and does not suffer from biases with image scale. Detection of spatially resolved galaxies is substantially different than detection of point-like objects (stars). There are three points in the FOCAS image reduction package where tuning to achieve optimal galaxy detection can be accomplished. The first point is the design of the spatial filter used to detect objects. This consists of a set of pixel weighting values w_i which are convolved with the pixel values at the location in the image of a prospective object in the field. If the values of a collection of pixels are s_i and the uniform background noise has RMS σ, the total signal-to-noise will be

$$S/N = \frac{\Sigma_i w_i s_i}{\sigma\sqrt{\Sigma_i w_i}}. \tag{2.4}$$

Differentiation leads to a condition on the filter weights w_i which extremizes (maxi-

mizes) signal-to-noise;

$$s_k \Sigma_i w_i^2 - w_k \Sigma_i w_i s_i = 0, \tag{2.5}$$

which is always satisfied if $w_i = s_i$. In other words, the optimal filter to detect a galaxy has the same profile as that galaxy. The drawback from using extended detection filters is increased computational overhead and increased susceptibility to systematic errors in the background (e.g., due to problems with flattening). And, of course, one does not know *a priori* the surface brightness profiles of the cluster galaxies.

Galaxies exhibit a wide range of surface-brightness profiles which have been described as exponentials, power-laws, or more complicated functions (Mihalas & Binney 1981). For the sake of simplicity, a reasonable choice is an exponential filter with a scale length similar to those of disk-like galaxies. This will significantly improve the detection characteristics over a Gaussian filter with the PSF FWHM and help ensure that the survey is not biased against these galaxies with their lower central surface brightness. A canonical disk scale length is 4 kpc; assuming $H_0 = 67$ km $\mathrm{sec}^{-1}\mathrm{pc}^{-1}$ this is an angular scale length of 1.44 arc-seconds (roughly 5.5 pixels) at $z = 0.13$. The angular width of the detection filter is adjusted according to the known redshift of each cluster to avoid distance biases. Beyond a redshift of $z = 0.25$ the FWHM of the filter is less than 1", i.e. smaller than the typical seeing disk, and there is no advantage to decreasing the width. For higher redshift clusters the total width of the detection filter template is set equal to the the "half-light" diameter of the exponential profile, 3.5 scale-lengths.

The second optimization point is setting the minimum number of pixels above the threshhold required to define an object. In theory, one can maintain rejection of spurious objects at lower detection threshholds by increasing the minimum number of pixels required. The trade-off is that it becomes increasingly likely that sources near the detection limit will fail the minimum pixels test and be rejected. Real objects with the smallest footprints will be point-like and thus I scale the required number of pixels with the size of the seeing disk. I set the minimum number of pixels equal to

the area within the half-light radius of the PSF. For a Gaussian PSF, this translates to

$$A_{min} \sim 1.1 W^2, \tag{2.6}$$

where W is the FWHM of the PSF in pixels. A_{min} is typically $\sim$ 20 pixels for the image scale and seeing conditions of the survey.

Finally, one can adjust the pixel value detection threshhold in terms of the RMS noise in the image. As one lowers this threshhold one achieves detection of lower surface brightness objects and more accurate isophotal magnitudes, but at the cost of a higher rate of spurious detections. Extensive tests of the DETECT routine with Monte Carlo simulations of noise images using different detection threshhold levels and minimum areas show that the spurious detection rate per pixel obeys the empirical relation;

$$N \sim 9 \times 10^{-4} e^{-\sigma^2 (A/12)^{0.18}}, \tag{2.7}$$

where σ is the detection threshhold and A is the minimum area in pixels. Thus A must increase very rapidly with σ to maintain the same number of spurious detections. An acceptable rate (1% spurious/real) is attained using the suggested threshhold of 2.5σ. Note that these spurious objects will almost all lie at or near the limiting magnitude.

Although FOCAS provides a SKY routine to find the local background level around each detection limit, the cluster images are very well flattened and a single global value for the background is sufficient. This also avoid problems with object contamination of the background apertures in crowded fields. A background level for each image is calculated in IRAF using the ITERSTAT routine developed by M. Dickinson and kindly provided by C. Steidel. This algorithm calculates sky values by iteratively calculating mean and standard deviation and rejecting high-valued pixels associated with objects.

Deep images of clusters are crowded and galaxy isophotes may overlap. Overlapping galaxies will be detected as a single object by the DETECT algorithm. The SPLITS algorithm attempts to break these into their individual components by examining successively higher threshholds above the detection isophote. The threshhold

step is some fraction of the pixel-to-pixel standard deviation (default is 0.2). SPLITS works on a rectangle of pixels encompassing the detection isophote. Like DETECT, it searches for pixels above a given threshhold but it uses the raw image pixel values, not the filtered values. Again, a minimum number of pixels are necessary to define an object. New objects are identified as isolated groups of contiguous pixels above each threshhold. Ideally, the algorithm would split the merged isophotes of galaxies without producing spurious objects in the diffraction spikes of stars and extended halos of galaxies. Unhappily, this is usually not the case without great care. The only explicit control of the SPLITS routine is achieved by adjusting the zero-point and slope parameters that the algorithm uses to estimate the pixel-to-pixel noise from the pixel values. Increasing either of these will suppress splitting.

A point-spread function is automatically constructed for each image to distinguish between stellar-like and extended objects (i.e., galaxies). The PSF template is found using the AUTOPSF routine in FOCAS. This algorithm corrals a minimum of stars with a narrow dispersion in the radial moment of their light distribution and averages them to construct the template. Since the object catalogs are constructed from relatively deep images they are dominated by galaxies at the faint limit ($R \sim 23$), which may interfere with the construction of a true stellar template. I avoid this problem by including only objects brighter than $R < 21$. Very bright objects ($R < 16$) whose images may be influenced by the non-linear response regime of the CCD and are also excluded.

FOCAS separates objects into classes using a series of rules and a "resolution classifier scheme" which tests the surface brightness profiles of objects against templates constructed from the image point-spread function and broadened versions thereof. Objects which contain saturated pixels (saturation level set by the user) are automatically classified as stars. Objects with asymmetries or ellipticities greater than 0.9 are classified "long" (e.g. charged particle events). Objects which cannot be successfully modeled as a combination of normal stellar profile and a stellar profile broadened by less than a factor 9.5 are considered galaxies.

I use the standard classifier parameters to a magnitude of $R < 21$ to separate

stars and galaxies. Beyond this point in a typical image the classifier begins to fail and galaxies become mistaken for stars, as evidenced by an enormous rise in the differential "star" counts by $R \sim 21$. The galaxy counts become sensitive to atmospheric seeing and errors are introduced in the cluster/background differencing. Fortunately, the surface density of stars per unit magnitude at high galactic latitude begins to level out at $R \sim 19$ and is much less than the number counts of galaxies at levels two magnitudes fainter. In Fig. 6 I compare the differential number counts of stars with those of galaxies derived below. The counts are roughly equal by $R \sim 19$. To extrapolate the bright star counts to fainter levels I use the model of Bahcall & Soneira (1981), choosing to renormalize using the numbers of bright stars identified in the images. Galactic coordinates are taken to be $b = 30°$, $l = 0$, and the dominant population at these faint magnitudes is assumed to be low-mass red disk stars with $V - R \sim 1$. By $R \sim 21$ the galaxy counts are a factor of 6 higher than stars. The extrapolated model indicates that the contribution of stars at fainter magnitudes is small and thus I assume all objects at $R > 21$ classified as either stars or galaxies are actually galaxies.

FOCAS calculates a number of photometry parameters; only those used in the analysis are discussed here. The *isophotal area* is simply the number of pixels above detection threshhold associated with the object. An *isophotal magnitude* is calculated from these pixels using a zero-point supplied by the user. First and second moments of the x, y and radial coordinates are computed, both for the unweighted and intensity-weighted distribution of pixels in the detection area. A *total magnitude* is calculated by filling in concavities in the isophote shape and growing rings around the object until the area exceeds the isophotal area by a specified ratio. The total magnitude calculation is often unreliable, failing or having errors in crowded fields. The isophotal magnitude is used here instead.

Each catalog generated from each field was individually inspected for problems such as a very asymmetrical or noisy point-spread function template; spurious faint objects generated in artifacts such as the diffraction spikes of stars; or erroneous splitting of large, extended objects into smaller fainter ones. Very often, adjustments

were necessary to the point-spread function generation or splitting machinery to fix these difficulties.

2.1.6 Magnitude Errors

Errors in galaxy photometry are usually dominated by systematic effects such as poor isophote definition and the finite size of pixels rather than the Poisson noise of the total counts. I estimate magnitude errors by using cluster galaxies that were multiply imaged in the CCD image mosaic of Abell 1632. A plot of the errors vs. magnitude is shown in Fig. 2. The RMS error in the isophotal magnitude was found to scale with apparent magnitude as $10^{m/5}$, i.e., Poisson-like behavior. However the errors are much larger; of order 5% for the brightest galaxies. The zero-point of the magnitude-dependence is assumed to be the rest-frame surface brightness of the detection isophote plus a constant. I find,

$$\sigma(m) = \sigma_0 10^{-(\mu^0 - 5.0 - m)/5} \tag{2.8}$$

where $\sigma_0 = 0.10$ magnitudes.

2.1.7 Completeness

In the game of galaxy counting it is important to make corrections for, or at least estimate the *completeness* of a galaxy catalog at a given magnitude, i.e., the ratio of the number of galaxies that are detected to the actual number. In this project, completeness corrections become particularly crucial when estimating the relative numbers of low-luminosity galaxies in clusters. For the apparent magnitude range of interest $R \sim 21 - 23$, the background field galaxy counts are comparable to, or often greater than the expected cluster counts. Thus small changes in the completeness estimate can have a large effect on the result (a classic case of the peril of subtracting two large numbers to find a small one). Completeness also depends on characteristics other than the isophotal magnitude (e.g., surface brightness): To construct cluster LFs, galaxies are ordered only by apparent magnitude and the completeness at a

given magnitude is the integrated completeness over all other galaxy properties.

Most of the incompleteness in an imaging survey arises from three effects. First, galaxies with true apparent magnitudes near the magnitude or surface-brightness limits of the survey can fall below the detection limit due to the superposition of sky noise, errors in the CCD response, etc. Second, galaxies can be detected but misclassified as other objects. For example, compact dwarf elliptical (dE) galaxies in distant clusters might be mistaken for stars (Ferguson & Binggeli 1994). Third, faint galaxies may fall near bright stars or galaxies and not be discerned as separate objects by the detection algorithm. (In the reverse reaction, close pairs or multiples of stars may be mistaken for galaxies).

The last effect is a purely random phenomenon and can be robustly estimated through the use of Monte Carlo simulations of image. However, the first two effects depend both on random events (like a star being on the line of sight to a galaxy), and systematic dependences on the detailed properties of the galaxies. Without *a priori* knowledge of the full spectrum of galaxy luminosities and surface-brightness morphologies it is impossible to estimate the true incompleteness. For example, there may exist a host of extended, very low surface brightness galaxies in clusters which would never be detected in this survey.

One approach to this problem is to postulate a variety of galaxy morphologies to construct artificial galaxies images at a fixed magnitude which are then added randomly to the real images. The fraction of galaxies which are recovered is the completeness estimate. For a detailed description of this technique I refer the reader to Steidel & Hamilton (1993). The one disadvantage of this method is that without deeper, higher-resolution image one is never certain that the galaxy models correspond to reality. In the case of galaxy clusters this is particularly troublesome since the morphologies of the dwarf population in clusters are poorly characterized, and may even vary from cluster to cluster.

An alternative method is to assume that Nature is kind and that the galaxies that *are* detected at a given apparent magnitude span the full range of morphologies, although the distribution may not be representative due to the selection effects dis-

cussed above. A large number of faint objects can be combined to construct a high signal-to-noise galaxy template which is representative of galaxies at that magnitude. This template is then added repeatedly to the real images and the fraction which are recovered in the catalogs is found. Although the details of the individual galaxies are lost in the averaging process, the important gross properties, i.e., the radial distribution of surface brightness, are retained.

Of course, by using those galaxies which are already detected to make the template, one biases the completeness estimate towards a kind of upper limit. There may be additional objects, lurking in the noise, which are not detected and do not contribute to the template. A less biased template could be made by weighting the individual contributions by some *a priori* estimate of their detectability. With enough galaxies, in principle one could recover a very acccurate estimate of the completeness through interleaved iteration of the galaxy detection and template construction processes.

At a given isophotal magnitude, the 50 galaxies with the closest magnitude are selected and 10×10 arc-second sections centered on each of these galaxies are extracted from the image being considered. These are averaged, with exclusion of the three highest and the lowest pixel values at each pixel to eliminate neighboring objects or image defects. The template is then added to 100 random locations in the image and the fraction of recovered objects recorded. An object is considered recovered if an object of similar magnitude is found within 0.7" of where the artificial galaxy was placed. (The probablity of a spurious match is of order 2%).

2.2 Field Galaxy Counts

Accurate estimation of the contribution of field galaxies (mostly background galaxies) to the counts in cluster images are critical in determining the shape of the luminosity function, particularly its faint end, and in estimating the luminosity overdensity of the cluster within some aperture. Errors associated with statistical background galaxy subtraction are usually the limiting factor in detailed cluster galaxy measurements.

It is also important to estimate the *field-to-field variance* in the counts in order to calculate the errors in the cluster LF. My approach here is to fit a model to the counts and describe the fluctuations as the variance in the model parameters.

To obtain accurate estimates of field galaxy counts at faint magnitudes I used a series of nine very deep images obtained with a thinned 2048^2 Tektronix CCD with a R_s filter at the prime focus of the Kitt Peak Mayall 4-meter telescope and kindly provided by C. Steidel. The CCD was operated in 2×2 binning model with a final pixel scale of 0.48 arc-seconds and a field of view of 10 arc-minutes. These images were obtained as part of a program to find the galaxy counterparts to $z \sim 1$ absorption line systems detected in the spectra of $z \sim 2$ QSOs (Steidel & Hamilton 1993) and thus, for my purposes, are essentially random fields. Details regarding the images are in Table 4. The basic image processing and photometry were already performed by C. Steidel and collaborators. Some further image processing was done; Bright stars and charge-transfer tails were masked out and replaced with uniform sky value and in some cases large-scale variations in background removed using cubic spline fits to the surface with one or more segments and iterative 3σ pixel value rejection. All but one of the images were brought to a common 1σ surface brightness limit of 28.05 magnitudes arc-sec.$^{-2}$ or an effective detection limit of $\mu_{R_s} = 25.63$, about 1.5 magnitudes deeper than the cluster survey images. This is accomplished by simply adding random Gaussian noise to the images in appropriate amounts. The remaining shallower image has a μ_{R_s} limit of 25.23. The limiting magnitude is $R \sim 24.5$ although the incompleteness becomes appreciable two magnitudes brighter.

Galaxy catalogs were produced using the FOCAS analysis procedures described above. Apparent magnitudes were transformed to Kron-Cousins R assuming $R_s - R \sim 0.14$ (Steidel & Hamilton 1993). A Galactic extinction correction was applied using the A_B values in the NASA Extragalactic Database and assuming $A_R/A_B = 0.63$. Figure 3 plot the differential galaxy counts for the summed catalogs in the magnitude range $17 < R_s < 24$. The spatial detection filter optimized for clusters at $z = 0.175$ (an intermediate value in the survey) was usd. The data here is binned in 0.25 magnitude intervals; solid error bars are the errors in the weighted

mean of the fields; the dashed error bars represent the RMS field-to-field scatter. There is a break in the counts at $R \sim 21$ where the slope of the number counts flattens.

To accurately model the number counts, the intrinsic fluctuations in the background must be distinguished from systematic errors. Several systematic effects will cause errors in the field galaxy counts. Here I consider three such effects. Because the galaxy photometry is performed using limiting isophotes, Galactic extinction will not uniformly fade all objects, but attenuate those with the lowest surface brightness the most. In the extreme case of low surface objects near the detection limit, the fading can remove them from the catalog althogether. Atmopheric seeing will blur the images of stars and galaxies, making them more difficult to detect and separate. Finally, the choice of the angular size of the detection filter, optimized for the detection of closer cluster galaxies, may have a significant impact on the counts. These should be considered separately from the intrinsic fluctuations and random errors since their effects can in principle be measured and accounted for.

Two independent, non-parameteric tests for significant deviant behavior of the number counts in a field are the total counts within the magnitude range of interest and a Kolmogorov-Smirnov test of the apparent magnitude distribution. The latter is sensitive only to the distribution of values over some interval, not the total number of values. I examine compare the counts in the apparent magnitude range $17 < R < 24$ of each field to that of the summed fields. The bright limit is the brightest magnitude where there is still a significant number of galaxies; the faint end is where incompleteness of the catalogs becomes appreciable. I find that the K-S test is unable to distinguish between any of the individual fields and the average. The total galaxy surface density of each field is reported in Table 4.

The 0421+019 field counts are lower by a factor of 3.6 over the scatter of the remaining fields. This field has the highest Galactic extinction and a plot of surface density versus A_B shows the expected strong correlation (Fig. 4). With it are plotted the number counts in the 0421+019 field as a fraction of the average of five fields with $\langle A_B \rangle = 0.01$, after the magnitudes are corrected for extinction. The relative

counts deficiency in the former field grows with fainter magnnitude. After correcting the 0421+019 for an estimated 0.25 magnitudes extinction in the R_s band I find that the counts become deficient fainter than $R = 20$, falling to a relative completeness of 60% by $R = 24$. This means that in addition to fading all the galaxies, the surface brightness effect of extinction causes a fraction of the faint galaxies to drop out of the catalog. I adopt a crude empirical description of the combined fading and incompleteness: The surface densities are adjusted using the empirical relation

$$\log_N = \log_{N(0} - 0.63(\gamma + 0.47)A_B \tag{2.9}$$

After this correction I look for a correlation with seeing (here described as the intensity-weight radial moment of the PSF); None is seen (Fig. 5).

The width of the spatial detection filter in FOCAS is varied inversely with cluster redshift to maintain a constant linear scale at the distance of the cluster galaxies. A possible systematic effect on the counts of background galaxies (which have more or less a fixed redshift distribution) was investigated by analyzing the field images using detection filters of different widths. The number counts from one of the fields are shown in Fig. 5 for filters optimized at differrent redshifts. There is a significant suppression of the galaxy counts fainter than $R = 21$ for filters optimized to redshifts $z < 0.10$. The effect is dramatic; for $z = 0.1$ filters the counts are consistent within the errors with higher-redshift filter; at $z = 0.09$ the counts are lower by a factor of about 2 to $R < 24$. Thus in the analysis of the cluster surveys, the widest detection filters used are optimized for $z = 0.1$.

The catalogs from eight image are combined (the high extinction field is excluded as a conservative measure) to construct a model of the mean number counts. The magnitudes in each field are corrected by $0.63A_B$ magnitudes of extinction and the associated losses due to extinction are corrected by multiplying the field of view by the factor $10^{-0.30A_B}$. Completeness corrections (never exceeding 10% for $R < 24$) are made using the procedure described in §2.1.7. I fit a broken power-law normalized

at $R = 21.0$ to the number counts in the range $17 < R < 24$;

$$n(17.0 < R < 21) = n_{21} 10^{\gamma_1 (R-21)} \tag{2.10}$$

$$n(21 < R < 24) = n_{21} 10^{\gamma_2 (R-21)} \tag{2.11}$$

The slopes γ_1, γ_2 and associated 1σ errors are found by maximum likelihood analysis of the data and Monte Carlo simulations thereof. The normalization at $R_s = 21.5$ is set to match the total number of counts within the magnitude range. I find $\gamma_1 = 0.505 \pm 0.014$, $\gamma_2 = 0.304 \pm 0.006$ and $n_{21} = 4472 \pm 120$. The solution is plotted as a solid line in Fig. 3. The formal χ^2 for 0.5-magnitude bins (14 degrees of freedom) is 11.9 based on Poisson errors. This relatively high value of χ^2 is not surprising given that the fluctuations in galaxy counts are super-Poissonian (see below).

Several other results are plotted with the counts; two fields with the same R_s filter (Steidel & Hamilton 1993); deep R-band counts using the Keck 10-meter telescope (Smail *et al.* 1995); the CCD imaging of Metcalfe *et. al.* (1991) taking $R = r_F + 0.13$; and the r_F Digitized Palomar Sky Survey II photograph counts which are well described by $\log_{10} n(r_F) dm \sim 0.327 r_F - 3.20$ (Weir *et al.* 1995). There is some disagreement between the counts, but they bracket the results derived here. My counts are lower than one of the Steidel fields and the Keck fields but are in turn significantly higher than the counts of Metcalf *et. al.* at $R \sim 22$ and nearly identical with the $R < 20$ counts of Weir.

As mentioned previously, a proper analysis of cluster luminosity functions requires one to estimate the errors associated with the LF parameters. A major source of error arise in the process of statistically subtracting the background galaxies, which are determined from independent fields. Field-to-field fluctuations in the background galaxy counts will introduce uncertainties into the resulting LF. The errors can be estimated using Monte Carlo simulations of the data where the Gaussian-distrubted variation isintroduced into the background parameters. It is observationally well-established that, due to the clustering of galaxies on the sky, the field-to-field variance in the number counts exceeds the Poisson estimates by a significant factor,

typically 2-3 (Jones *et al.* 1991). The variance depends both on the angular field of view and, through the amplitude of the galaxy-galaxy correlation, on the magnitude, with fainter galaxies being less strongly clustered (Efstathiou *et al.* 1991). If the angular correlation function of galaxies to some magnitude limit obeys $w(\theta) \sim \theta^{-0.8}$ (Peebles 1993) then the field-to-field variance in the number counts will be,

$$\left\langle \left(N - \bar{N}\right)^2 \right\rangle = \bar{N} + C(m)\theta^{-1.8} \tag{2.12}$$

where θ is now the field of view and C describes the strength of the clustering and is a function of the magnitude range.

To measure the effect of this scatter on the description of the backgound counts used here, the broken power-law model is fit to the eight individual 10×10 arc-minute fields. The background fluctuations will manifest themselves as field-to-field variance in the model parameters. In addition, single 5×5 arc-minute subsections of each field are then extracted, and with a seventh small field, are analyzed in the same way to examine the dependence on the angular field of view.

As an important aside, I find a significant covariance between the faint-end slope and the $R = 21$ normalization in the sense that the variance in the faint galaxy counts is minimized (Fig. 6(b)). If the counts in the range $21 < R < 24$ were constant, then the variation in n_{21} and γ_2 (δn_{21} and $\delta\gamma_2$) are related by,

$$\frac{\delta n_{21}}{n_{21}} = \left(\frac{1}{\gamma_2} - \frac{3\gamma \ln(10) 10^{3\gamma_2}}{10^{3\gamma_2} - 1} \right) \delta\gamma_2. \tag{2.13}$$

For $\gamma_2 = 0.304$, $\delta \log n_{21} \sim 0.90 \delta\gamma_2$. This locus is plotted in Fig. 6(b). The close correspondence with the data motivates fixing γ_2 to maintain a constant number of galaxies while the normalization at $R = 21$ varies.

For the 100 square arc-minute fields the field-to-field RMS scatter in the bright slope γ_1 is 0.08 about a mean of 0.40. The variance in n_{21} is 19%, or 2.4 times the Poisson value. For the 25 square-arc minute fields the, $\sigma_{\gamma_1} = 0.14$ about a mean of 0.45, and $\sigma_{n_{21}} = 20\%$ (1.44 times the Poisson value). These are consistent with the results of Jones *et. al.* (1991)

2.3 Global Galaxy Cluster Properties

If either the formation or subsequent evolution of galaxies is significantly affected by the cluster environment, or by its humble beginnings as a fluctuation on a mass scale of $10^{15} M_{\odot}$, this phenonomen might manifest itself by systematic correlations of galaxy properties with the global properties of the cluster. The two traditional properties that have been investigated are the richness and the morphology of a cluster. The former refers to the projected density of galaxies in excess of a mean background, usually in a fixed metric aperture. The second describes the geometry or shape of the cluster galaxies or its graviational potential. Cluster classifications based on subjective inspection of photographic plates exist in the literature (Bautz & Morgan 1970; Rood & Sastry 1971) but lack any quantitiative or objective nature. Most of the clusters in my sample are also too distant for photographic plate material. Thus I attempt some kind of classification using the information in the limited field of view of the CCD imaging.

2.3.1 Cluster Richness

Abell (Abell 1958) counted the number of galaxies C_A in excess of the background level within an aperture of radius 1.5 h^{-1} Mpc and with magnitudes between m_3 and $m_3 + 2$, where m_3 is the magnitude of the third brightest galaxy in the cluster. He assigned richness classes, with R = 0 clusters having 30-49 galaxies, R = 1 with 50-79 galaxies, R = 2 with 80-129, R = 3 with 130-199 galaxies, R = 4 with 200-299 galaxies, and the single R = 5 cluster in the catalog, Abell 665, having at least 300 galaxies. The counts and assigned classes are generally found to be accurate to about one richness class, with a systematic error of underestimating the richness with increasing redshift. As an extreme example of error, the very rich (and most distant at $z = 0.370$) cluster Abell 370 was assigned a richness class of 0 in the catalog.

I make an independent measurement of the cluster richness with which to correlate galaxy properties. Rather than use galaxy counts, I estimate the luminosity overdensity (with respect to a estimated cosmological mean value) within an aperture

centered on the peak of the cluster surface brightness. Luminosity density may be a more robust measurement than counts for two reasons: It is not dominated by the faintest and most numerous galaxies and therefore not sensitive to the exact cut-off in absolute magnitude; Second, merging of galaxies or 'cannibalism' by the brightest cluster galaxy will preserve luminosity but not number.

I calculate the luminosity overdensity δ_L within a fixed projected linear distance from the cluster center. I identify the cluster center as the peak in the surface brightness distribution of the cluster, measured with some smaller aperture. The result may depend on the size of the smaller aperture used, and thus I do not wish to make an *ad hoc* choice. Instead, I define an aperture which is appropriate to the mass scale of a Brightest Cluster Galaxy. To do this, I use a standard BCG luminosity and calculate a mass using a M/L value typical of giant galaxies. I then assume that the density profile of the cluster is that of an isothermal sphere and that the Abell radius of the cluster corresponds to the virial radius where $\rho = 178\bar{\rho}$. This choice of profile and normalization give the radius containing the BCG mass scale. Taking $M_R^{BCG} = -23.60 + 5\log h$ (see 2.5) and $M_\odot = +4.3$ in the R-band to find $L_{BCG} = 1.45 \times 10^{11} h^{-2} L_\odot$, and assuming a mass-to-light ratio of $100h(M/L)_\odot$, this mass scale is $1.5 \times 10^{13} h^{-1} M_\odot$. Taking the virial radius of clusters at the present epoch to be the Abell radius $r_A = 1.5h^{-1}$ Mpc then the mass contained within r_A is roughly

$$M_A = \left(\frac{4}{3}\pi r_A^3\right)\left(178\Omega^{0.4}\rho_c\right), \tag{2.14}$$

or $3.8 \times 10^{14} h^{-1} M_\odot$ (assuming $\Omega = 0.2$). For an isothermal sphere, the mass contained within a given radius is proportional to that radius. Thus the radius containing an equivalent BCG mass is then 0.04 of the Abell radius or 55 h^{-1} kpc. This value is comparable to what is often taken to be the "core radius" of clusters. I define the corresponding angle for the BCG assuming a $q_0 = 0.1$ cosmology;

$$\theta_{BCG} = \frac{0.04\,(1+z)^2}{0.1z - 0.9\left(\sqrt{1+0.2z} - 1\right)} \tag{2.15}$$

in seconds of arc.

I use the LCRS estimate for the mean luminosity density of the Universe (Lin *et al.* 1996) and thus for consistency I calculate the total luminosity from all $M_R < -17.41$ galaxies within a radius of $0.5h^{-1}$ Mpc. The flux from all galaxies within the corresponding angular distance is summed and corrected for missing and excised areas outside the CCD field of view assuming a θ^{-1} projected surface density profile (Beers & Tonry 1986). The contribution from the background is subtracted and the remaining flux is converted to luminosity using the redshift of the cluster.

This luminosity is to be compared with the cosmological mean luminosity with a sphere of the same radius in order to calculate a luminosity over-density δ_L. To do this, a correction must be applied the cluster luminosity to remove the contribution from outer regions of the cluster projected along the line of sight. To estimate the magnitude of this effect, I consider a 'toy' model of a spherically cluster with a power-law luminosity density profile. The ratio of the luminosity within the sphere compared to the total projected luminosity along the line of sight of the sphere is,

$$F = \frac{2}{(3+n)\int_0^\infty \ln(1+z^{-2})\,dz}, \tag{2.16}$$

where n is the power-law index. Taking $n = -2$, I find $F = 2/\pi$. I use the luminosity density estimated from the Las Campanas Redshift Survey over the same absolute magnitude range; $\bar{\rho_L} = 1.9 \times 10^8 h L_\odot Mpc^{-3}$. The mean luminosity within a sphere of 0.5 h^{-1} Mpc is $1.0 \times 10^8 h^{-2} L_\odot$ for $M_R < -17.41 + 5\log h$. The random error in the overdensity is taken to be the Poisson fluctuations associated with the finite galaxy counts within the aperture. I ignore the error in the calculation of the mean luminosity density since this will only produce a systematic offsets in all cluster values. Note that δ_L does not depend on h or Ω.

I calculate δ_L for all clusters, both photometric and non-photometric, keeping in mind that non-photometric conditions will systematically decrease estimates of δ_L. Fig. 7 is a plot of δ_L versus redshift. There does not appear to be a significant trend with redshift.

A comparison between C_A and δ_L for the photometric clusters appears to be

simply a scatter plot (Fig. 7). The "sore thumb" is Abell 2218, the richest cluster in the survey. Even if the two quantities are uncorrelated, are they consistent? I compare the overdensity computed (or estimated) within the 0.5 h^{-1} Mpc diameter aperture with the Abell counts. To do this, I convert C_A into an equivalent δ_L. I assume that the $\rho_L \sim r^{-2}$ profile extends at least to the Abell radius of 1.5 h^{-1} Mpc, such that the overdensity within the Abell radius is $\delta_A = \delta_{0.5}/9$. I then remove the correction of $2/\pi$ made earlier to remove outer cluster galaxies projected onto the field of the inner cluster. To convert to galaxy counts, I assume a Schechter function with a flat faint-end slope α (the exact value is not important here since the counts do not extent much past M^*). I assume that the third-ranked galaxy is actually the second brightest galaxy that is drawn from the Schechter LF and use the following definition,

$$C_A = \phi_0 \int_{m_3}^{m_3+2} exp\left(-10^{-0.4(m-m^*)}\right) dm \tag{2.17}$$

$$1.5 = \phi_0 \int_{-\infty}^{m_3} exp\left(-10^{-0.4(m-m^*)}\right) dm \tag{2.18}$$

For each value of C_A the value of $m_3 - m^*$ is found by evaluating the ratio of the two equations, whereupon the normalization ϕ_0 is determined. The total luminosity within the Abell sphere to $M_R = -17.41$ (about $M^* + 2.8$) is then estimated and divided by the mean field value (0.58 L^* per Abell volume);

$$\delta_A \sim \frac{2}{\pi}\frac{1}{4.64}\phi_0 \int_{m_3}^{m_3+2} exp\left(10^{-0.4(m-m^*)}10^{0.4(m-m^*)}\right) dm \tag{2.19}$$

Interestingly, $C_A = 100$ gives an overdensity of $\delta_A = 170$ within the Abell volume, consistent with the Abell radius being the approximate virial radius of a rich cluster. Finally δ_A is divided by nine to give δ_L within the 0.5 h^{-1} Mpc radius. The result is plotted in Fig. 7. The good agreement is comforting, if not terribly impressive due to the large scatter in the data. I thus conclude that my overdensity estimates and Abell's richness classifications are consistent.

2.3.2 MORPHOLOGY

Abell established a limited morphology classification for his clusters; However, the two better-known morphological classifications for clusters of galaxies are the Bautz-Morgan and Rood-Sastry types. The classification of Bautz & Morgan (1970) is based upon the luminosity of the brightest cluster galaxy with respect to the other cluster members. Type I clusters contain a central cD galaxy; Type II contain a giant elliptical or ellipticals, and Type III contain no dominant galaxies. Standard examples given by Bautz and Morgan for the three types are Abell clusters 2199 and 2029 (I); Abell clusters 194, 1656 (Coma), and 2197 (II); and the Virgo and Corona Borealis (Abell 2065) clusters (III). The morphological classification of Rood & Sastry (1971) is based more upon the spatial distribution of the brightest galaxies and is arranged into a "tuning fork" with two branches. The base of the fork is occupied by cD clusters with a central supergiant galaxy. At the branching point are B (binary) clusters with two giant galaxies of roughly equal luminosity. One branch contains L (linear) and F (flattened) clusters with a high flattened distribution of bright galaxies, while the other contains C (core-halo) and I (irregular) clusters with a more circular or irregular distribution. Bautz & Morgan suggested that this morphological sequence might correspond to an evolutionary sequence from older to younger clusters.

The optical characterization of galaxy clusters since that time has concentrated on quantifying the amount of so-called "sub-structure" in the spatial and velocity distribution of galaxies. Older, dynamically relaxed clusters are expected to exhibit less; dynamically young, more. A complete review of the subject is beyond the scope of this thesis, particularly since most of the techniques are unsuitable for this data. The reader is referred to a review and comparison of different techniques in Pinkney *et. al.* (1996). Substructure tests have also been developed and applied to the surface brightness morphologies of the X-ray emission which originates from an intracluster medium in approximate hydrostatic equilibrium with the gravitational potential of the cluster (Mohr *et al.* 1995; West *et al.* 1995). In particular Buote & Tsai (1995; 1996) have pursued a fundamental approach, performing a multipole expansion of the graviational potential and constraining the relative "power" in each moment using

X-ray measurements. Rhee *et. al.* (1992) and Pinckney *et. al.* (1996) perform a somewhat similar, but less physically based analysis of optical data using a Fourier expansion of the galaxy distribution.

Although it is tempting to perform a multipole expansion here using galaxies in place of X-ray photons, there are several reasons why this is impractical with this data. First, the distribution of galaxies on ~ 1 Mpc scales is much less centrally concentrated than the X-ray surface brightness: The data indicates that the projected surface brightness profile of Abell clusters falls as θ^{-1}. The X-ray emissivity of the intracluster medium, on the other hand, is proportional to the square of the gas density and the X-ray surface brightness is observed to fall off with a much steeper index of -3 to -4 (Jones & Forman 1984). A flatter profile leads to much larger random errors in the moments. Secondly, the number of independent optical measurements (locations of bright galaxies) is of order $10^2 - 10^3$, an order of magnitude smaller than the number of X-ray photons from a cluster observed with a reasonable integration time, and also leading to larger random errors. Finally, the finite optical field of view and significant offsets between the true center of the cluster and the coordinates given in the Abell catalog (determined from the projected overdensity on a much larger scale of 3 h^{-1} Mpc) lead to spurious contributions to the moment calculations which cannot be removed without making dubious assumptions about the symmetry of the cluster geometry. Finally, bright stars in the cluster foreground can null sections of the effective field of view, producing erroneous moments.

Instead, I attempt to classify the morphologies using two parameters that describe (1) the concentration of galaxies towards the cluster center and (2) the relative prominence of the cluster center with respect to other peaks in the surface brightness.

For the first parameter, I return to a comparison between the Abell counts within 1.5 h^{-1} Mpc and overdensity computed within 0.5 h^{-1} Mpc. Some of the scatter is undoubtably due to Poisson and photometry errors (Abell's as well as mine). However, 1 magnitude of error moves the points only 0.4 dex and probability will not qualitatively change the general distribution of the points. An interesting

hypothesis to explore is that the Abell counts are accurate to the limit of the Poisson statistics and that the observed large scatter between the overdensity and C_A is due in part to variations in the radial profile or morphology of the cluster. Dynamically relaxed clusters with highly dense cores would have much larger values of δ than similarly rich but less concentrated clusters. If this could be shown to be the case the ratio of the two values would be a important quantity with which to classify galaxy clusters.

Fig. 8 is a somewhat complicated plot which encodes the the standard morphological classifications in the points (see §2.3.2). The points are larger with lower numbered Bautz-Morgan type, and become rounder with later Rood-Sastry types. If these classification correspond to dynamical ages, the larger, rounder points are older and thus might be exptected to show a greater concentration of galaxies in their cores, increasing δ_L with respect to C_A. The plot does suggest such a correlation. Motivated by this possibility, I define a concentration index

$$I_C = log_{10}\left(\frac{\delta_{0.5}}{9\delta_A}\right) \tag{2.20}$$

which takes on a zero value for an isothermal sphere. δ_A is calculated according to the procedure described above. Abell counts, $\delta_{0.5}$s, and I_Cs for all clusters are given in Table 3.

The second parameter, a "peak index" I_P, is defined as

$$I_P = -\log_{10}\left(\frac{f_2}{f_1}\right) \tag{2.21}$$

where f_1 and f_2 are the fluxes of the brightest and second-brightest peaks measured in the $0.055h^{-1}$ kpc aperture defined in §2.3.1. The second-ranked peak is found in the same way as the first-ranked, with the added requirements that the peak must be a true peak, i.e. all neighboring grid values must be smaller, and its center must be separated from the center of the first-ranked peak by at least 4 aperture radii ($220h^{-1}$ kpc).

A cluster characterized by a single very bright galaxy or concentration of

galaxies (Rood-Sastry types D and C) would have a large value of I_P, while a bimodal cluster or irregular cluster would have a value approaching zero. I expect a redshift bias in that the brighter second-ranked peaks of nearby clusters will be more likely to fall outside the field of view and P_I will tend to decrease with redshift. This trend is shown in Fig. 8.

Finally, I plot the clusters in $I_C - I_P$ space (Fig. 9) with the points coded with Bautz-Morgan and Rood-Sastry type as before. The arrow shows the qualitative direction in which clusters are expected to evolve as they dynamically relax to a more concentrated state with a central peak. There is a tendency for the earlier (more relaxed) Bautz-Morgan and Rood-Sastry types to fall in the region of higher I_P and I_C but there is considerable scatter.

2.4 Luminosity Functions

2.4.1 LF Construction

The galaxy catalogs constructed from imaging of galaxy clusters at known redshifts can be used to construct luminosity functions, subject to the intrinsic photometric errors and uncertainties in background galaxy subtraction. A composite cluster LF can be used to determine the mean faint-end slope and the relative abundance of dwarf galaxies in clusters. A comparison of luminosity functions from cluster to cluster, and between clusters and field, can be used to ascertain whether galaxies obey a "universal" luminosity function or if different environments have produced or evolved different galaxies.

The analytical form of the LF proposed by Schechter (1976) and motivated by the Press-Schechter formalism (Press & Schechter 1974) has been repeatedly shown to provide a fair description of both cluster and field galaxies, provided one allows the two free parameters M^* and α to vary. I thus use this convenient formulation to describe my data and compare it with previous work.

The absolute magnitude limit to which galaxies are included in fitting an LF

model must be chosen with some care. Evidence for a steep upturn in the LF at faint absolute magnitudes indicates that the results of a LF fit may depend sensitively on the elected cut-off. Indeed, some of the disagreement between different previous work may have arisen from differences in the chosen limits in M. To be consistent with the analysis of the Las Campanas Redshift Survey (Lin *et al.* 1996), I use only galaxies brighter than $M_r = -17.5 + 5\log h$ ($M_R = -17.41$) unless otherwise mentioned. I also exclude the first-ranked, and sometimes the second-ranked, galaxies since these do not appear to obey statistics commensurate with a Schechter function (see §2.5).

By far the most critical process in constructing a luminosity function is correct subtraction of the background field galaxy contribution. Modest errors in the background counts can produce substantial errors in the derived LF. I use two independent and complementary techniques to accomplish this. The first technique uses separate, random fields to establish the background counts (§2.2). While being a more objective method the results can suffer from random errors due to the fluctations in the background counts as well as serious sytematic errors including errors in photometry between the cluster and background fields, differences in seeing, and different completeness corrections. The second technique differences the high-density and low-density regions on the cluster image(s) to remove the background (as well as some of the cluster signal). This generates results that are free of the systematics described above, but assumes that the luminosity function of cluster galaxies is independent of the local density. Since the morphological breakdown of galaxies depends on the local density (Dressler 1980), there is no reason to suppose that the luminosity is invariant. Differencing high- and low-density regions may result in a LF which is skewed from the true LF in either region. However, performing both operations on the same data set and the results checked against each other is potentially a powerful technique to isolate such errors, and this is the approach I take here. Below I discuss some mechanical details relevant to each method.

Absolute background subtraction: A model consisting of the background model constructed in §2.2 and a Schechter function (modulus the redshift of the cluster) is convolved with an estimate of the completeness and fit to the distribution

of galaxies with apparent magnitude to find the two free parameters M^* and α. A typical cluster catalog generated from CCD imaging of clusters contains a few hundred bright galaxies, only a small fraction of which will be brighter than M^*. In this low-signal regime it is clearly hazardous to pursue the traditional route of sorting the galaxies into bins with magnitude and attempting a least-squares fit of a Schechter function to the count; the exact choice of bins may significantly effect the value of M^* obtained, and thus α. Instead, I use the method of maximum likelihood [e.g., (Efstathiou *et al.* 1988)] which treats the data in unbinned form. A galaxy count model is constructed from a Schechter function superposed on the power-law background count model described in §2.2. The two free parameters of the Schechter function are determined through the method of maximum likelihood (the LF normalization is fixed to match the total number of galaxies). A "black-box" extrema-finding algorithm, kindly provided by J. Tonry, was used.

Random errors in the Schechter function parameters are produced by (1) shot noise from the finite number of galaxies used to construct the luminosity function; (2) galaxy magnitude errors; (3) intrinsic fluctuations in the normalization and slope of the background counts; and (4) photometry errors from uncertainties in atmospheric and interstellar extinction. I estimate errors by Monte Carlo simulations of the data using the following prescriptions: The magnitudes of the simulated galaxies are randomly drawn with replacement from the real data set. The total number of galaxies is held fixed since this is an independently measured quantity. Gaussian-distributed errors in isophotal magnitude are introduced using the relation described in §. The normalization and slope of the background counts are varied by a Gaussian with the standard deviation given by Eqn. 2.8. Although the variations in these quantities are covariant, as a simple, conservative approach I vary them independently. Finally, I add a Gaussian-distributed error of 0.03 magnitudes in the offset between the background and cluster photometry to account for possible errors. This accounts for maximal errors of 0.02 magnitudes in atmospheric extinction and 0.02 magnitudes in interstellar extinction. I estimate the 1σ errors in the parameters using the 68% percentile limits of LF parameters from 100 Monte Carlo simulations. I then calculate

a goodness-of-fit by calculating the χ^2 per degree of freedom between the data binned in half-magnitude or magnitude intervals and the best-fit luminosity function.

Differential Background Subtraction: This is a procedurally much simpler technique. The center of the cluster is identified as the peak in the cluster surface brightness using a 0.055 h^{-1} kpc aperture, as described in §2.3.2. Galaxies are then separated into inner and outer regions, depending on their projected distance from the cluster center. Typically a separating radius of 0.5 h^{-1} Mpc is used. The separate catalogs are then binned in magnitude, and differenced, weighting the bins by the inverse of the accessible area on the sky. A completeness correction is then made. I require that the outside region have an area at least 1/3 of the inner region to have a sufficiently accurate estimate of the "background".

2.4.2 Composite Luminosity Function

A composite LF is constructed by compiling the galaxy catalogs from 22 clusters imaged with the Loral CCD/R_s filter combination under photometric conditions. There are 5489 galaxies in the range $-23.41 < M_R < -17.41$ (excluding the first- and second-ranked galaxies). The best-fit Schechter function using the absolute background correction has $M_R^* = -21.13 \pm 0.11 + 5\log h$ and $\alpha = 1.09 \pm 0.08$. This is plotted in Fig. 10 with the background-subtracted and completion corrected data binned into 0.5-magnitude bins (solid points). The catalog is essentially complete to an absolute magnitude of -17, but is only 50% complete at $M_R = -15.5$. The reduced χ^2 (14 degrees of freedom) is 14.2, indicating there is considerable structure that is not well described by the simple choice of LFs. The most noteworthy of these is a dip at $M_R \sim -19.7$. The distribution of parameters with 1000 Monte Carlo simulations of the data are plotted with the 1σ limits in Fig. 11. If I include the second-ranked galaxy the parameters changes in value to $M_R = -21.30$ and $\alpha = 1.13$, a difference that is not significant compared to the errors in the values.

Much previous work on cluster LFs with shallower photographic data has fixed the faint-end slope to $\alpha = 5/4$, as prescribed by Schechter (1976), to obtain a well-defined value of M_*. The two Schechter parameters are strongly covariant; thus to

compare with this work I also fix α to this canonical value, to find $M_R^* = -21.47 \pm 0.14$. The difference in predicted counts between the two fits is no more than 25% over the magnitude range of the fitting; The best-fit $\alpha = 1.25$ Schechter function slightly under-predicts the number of bright galaxies while over-predicting the number of faint ones.

The completeness-corrected LF, constructed using differential background subtraction and a 0.5 h^{-1} Mpc radius aperture to separate the "cluster" and "background" galaxies, is plotted as the open points. The differential background-subtracted LF is re-normalized to predict the same total number of $M_R < -17.41$ galaxies. The agreement, on the whole, is excellent. To determine if any variation of the LF with distance from the cluster center might be causing systematic errors in my results, I construct a third LF with a differential background subtraction using galaxies having a projected distance of at least 0.75 h^{-1} kpc from the cluster center. Of course, this biases the sample to galaxies in the more distant clusters where the linear field of view is larger, and as a result the completeness limit is brighter. The errors in this smaller sample are also correspondingly larger and I bin the data in 1-magnitude bins. This LF and the best-fit LF found from absolute background subtraction of the entire sample are compared in Fig. 11. As a final check between the two different methods, I fit a Schechter function plus absolute background model to these 969 outer galaxies brighter than $M_R = -17.41$. This yields yields $M_R^* = -21.03 \pm 0.29$ and $\alpha = -1.00 \pm 0.23$. The LF of the total catalog and the outer subset are statistically equivalent. Thus I conclude that, barring an extremely insidious conspiracy between a sytematic error in the background subtraction and radial variation in the LF, the two LF constructions arrive at approximately the same LF.

2.4.3 Variation of the Cluster Luminosity Function

I wish to determine whether there is any significant of variation of the luminosity function with redshift and the various cluster parameters described in §2.3.2, or if the cluster LF is indeed consistent with being "universal". The errors in the best-fit Schechter parameters become progresssively (and depressingly) larger as one sub-

divides the sample down to the level of individual clusters. For this reason, I first attempt to assess the reality of an effect by simply dividing the 22 clusters into two bins by the relevant parameter and determining whether there is a statistically significant difference in the best-fit Schechter values. I perform two fits for each sample; one with both Schechter parameters "free", and the second with α fixed to 5/4 to obtain a better-defined M^* with which to compare different samples. Errors are computed only for the latter. The results are tabulated in Table 5.

There appears to be a variation in $M^*(\alpha = 5/4)$ such that it is brighter in the higher redshift sample, brighter in the high density sample, and fainter in the clusters with Rood-Sastry cD types. A comparison between the 2-parameter fits of the low- and high-redshift samples and those for a fixed $\alpha = 5/4$ suggests that the latter is somewhat exaggerated from using too steep a value of α. Dwarf galaxies may be disappearing preferentially from the high-redshift sample due to surface-brightness selection effects, giving a lower observed value. Nevertheless the data supports luminosity evolution in M^* of at least $\sim$ 0.2 magnitudes, a value commensurate with the predictions of the passive evolution of early-type galaxies (Buzzoni 1995). This effect may also explain some of the variation with overdensity δ because of the bias towards richer clusters with higher redshift clusters in the Abell catalog. In addition, the values of δ and M^* are covariant in that fluctuations of the number of the few brightest galaxies in the cluster will affect δ and M^* in the same way. The values of M^* do not appear to vary with the morphological parameters of the cluster with the exception of the anomolously faint values of M^* for the Rood-Sastry cD clusters. Note, however that there are only three cD clusters in the sample.

Finally, maximum-likelihood fits of the Schechter LF-plus-background model were made to each of the 22 individual photometric cluster galaxy catalogs. Plots of the LFs are included in Appendix B. Inspection of these plots suggests that, with a few exceptions, this choice of LF performs an adequate task of describing the bright end of the cluster galaxy LF.

A plot of M_R^* vs. α (Fig. 12) reveals the strong covariance between the two parameters. Thus much of the deviation is consistent with an invariant, but noisy LF.

Again, to compare with previous work, I fix the slope $\alpha = 1.25$ and find the best-fit value of M_*. The distribution of values is shown as a histogram at the bottom of Fig. 12. I also plot these versus the redshift in Fig. 12. There is a strong clustering of values around $M_R = -21.7$, but also a number of fainter values. It seems clear that the Monte-Carlo simulations are somehow over-estimating the measurement errors by a factor of ~ 2.

The values of M^* are plotted versus Bautz-Morgan type, Rood-Sastry type, and the two indices derived in §2.3.2 in Fig. 13. The plots are arranged such that older, more dynamically relaxed clusters would be expected to fall to the left. The M_* values around -21.7 show a significant trend such that they become brighter to the left. The values are also correlated with the luminosity overdensity (Fig. 14), such that M^* becomes brighter with δ_L. This is as would be expected since I_C and δ_L are not independent.

2.4.4 Discussion

The agreement between the composite LFs constructed using the absolute and differential background techniques is an excellent indication that there are no serious systematic errors in the shape of the LF induced by the background modeling in the former, or a variation in the cluster LF in the latter. The LF in its general form is well described by the classic, nearly-flat Schechter function as has been found for the field. There appears to be a significant "dip" in the LF at $M_R \sim -19.5 + 5\log h$. This appears to be general feature of the cluster LF. For example, Biviano *et. al.* (1995)) find a similar dip in the Coma cluster at $M_b < -17.3 + 5\log h$. Otherwise, the LF is fairly flat at least to $M_R < -16.5$, in good agreement with field surveys and some work on the cores of clusters.

The LF derived here is inconsistent with claims of a bright upturn in in the LF at $M_R \sim -17.5$ reported in some clusters. At magnitudes much fainter than this the LF depends critically on the completeness correction which, as I have discussed, is difficult to quantify. I thus conclude that there is no strong evidence from this data for a steep faint end to the LF or a dwarf excess. From the fact that there are

22 randomly chosen clusters in the sample I also conclude that any excess seen in particular clusters is not a general phenomenon. Unfortunately, there is no overlap in my sample and those in which excesses have been seen, so that it cannot be determined if the disagreement arises from a difference in the image reduction and analysis.

Assuming a $R-r$ correction of 0.09 magnitudes, the M^* derived for this sample of cluster galaxies with $M_R < -17.41$ is 0.93 ± 0.20 magnitudes brighter than the value derived from the galaxies in the LCRS survey (Lin *et al.* 1996) (refer to Fig. 1). However, part of the difference may be due to the detailed fitting of the LCRS LF and the anomolously flat faint-end slope. The difference between this result and other field surveys is about ~ 0.5 magnitudes. That there exists a difference should not be terribly surprising, given that the morphological distribution of cluster galaxies are very different from the field. With α fixed to 1.25, the value $M_R^* = -21.47$ is signficantly brighter than nearly all previous values derived from clusters. This exact amount of discrepancy is not known since the F-R colors of these objects have not been independently measured. By dividing the clusters into bins with redshift and morphology, I have demonstrated that there is a tendency for M^* to brighten by 0.2-0.4 magnitudes with increasing redshift and denser clusters with a more relaxed morphology. With the small size of the photometric sample and the well-known bias towards rich systems at high redshift do not make it possible to distinguish between these two affects at this time. The evolution is, however, consistent with passive stellar evolution predictions (Buzzoni 1995).

2.5 Brightest Cluster Galaxies

The brightest galaxy or brightest two galaxies were identified in each cluster and were analyzed independently of the image analysis used to obtain galaxy photometry and described above. Identification of BCGs is a process fraught with peril. The number counts of foreground field galaxies (see §2.2) are such that on average one galaxy brighter than $R = 15.90$ should appear in a field of 75 square arc-minutes (typical of the survey). This is consistent with the apparent magnitude of the BCGs

in clusters at redshifts from 0.15 to 0.2. Fortunately, true BCGs are located in the denser centers of the clusters and are fairly homogeneous in their surface brightness morphology, i.e., are elliptical galaxies with extended profiles. Their inner isophotes are almost always very round but the outer isophotes may be considerable flatter, with ellipticities approaching 0.5. Foreground galaxies are usually spirals and will be located randomly in the field. I found that with a little experience, these two distinguishing characteristics can be used to discriminate against contaminants. There are also clusters that contain no obvious BCG in which case the brightest galaxy identified by FOCAS was used.

In a number of cases the BCG candidate fell very close to the edge of the field of view, several arc-minutes from the cluster center given in the Abell catalog. This may be due to errors in the coordinates (Huchra, private communication) as well as physical offsets between the location of the BCG and the projected overdensity of the cluster on the scale of the Abell radius. Whatever the reason, it implies that a certain fraction of the clusters in this sample may have BCGs that fall outside the CCD imaging field. Thus the object that is identified as the brightest galaxy likely to be a cluster member may not actually be the true BCG.

FOCAS does not lend itself to the analysis of very extended galaxies such as BCGs. Instead, I use a standard elliptical isophote fitting routine to measure the total counts to levels below the 1σ pixel-to-pixel deviations and estimate a total luminosity. I used the isophote fitting task ELLIPSE in the Space Telescope Science Data Analysis Softward (STSDAS) package. This routine is based on the isophote analysis technique developed by Jedrzejewski (1987) in which elliptical annuli of successively larger semi-major axes are fit to the surface brightness profile of a galaxy. The first through fourth harmonics of the surface brightness distribution within an annulus are calculated. The centroid, ellipticity, and position angle of the annulus are re-calculated using the first and second moments, while the third and fourth moments account for any "boxiness" of the isophotes. I then used the spline-fitting routine in BMODEL to construct a noise-free image of the galaxy using the isophote data created by ELLIPSE. Very often the isophote-fitting routine performs poorly in the central few kpc region of

the BCG, especially if there are multiple nuclei or very "boxy" isophotes. This inner region is usually uncontaminated by other objects and so the data image is used to replace the model image there. The resulting hybrid image is then subtracted from the original image to allow FOCAS to detect galaxies close to the BCG and prevent FOCAS from finding spurious objects in the extended halo of the BCG. The total counts from the galaxy image is measured and a magnitude calculated. This is different than the approach followed by Schneider *et. al.* (1983a) and Postman & Lauer (1995) and allows us to by-pass the correction factors that are used with a fixed metric aperture, at the cost of possibly larger random photometric errors and systematic errors from contaminating objects.

Fig. 15 plots the absolute magnitude M_1 of the brightest galaxies identified as BCG candidates (solid points) from the 22 clusters imaged with photometric conditions. Several features are immediately obvious from this plot: First, there is a significant locus of the most luminous objects at $M_R \sim -23.6$. The outlier with the extraordinary luminosity is the BCG in Abell 2244, which has a bright foreground star that is contaminating the isophote fitting and may be responsible for the offset. Second, the locus appears to have a significant trend with redshift such that more distant galaxies are more luminous. Third, there is the suggestion of a second locus at $R = -23$, albeit with a much larger scatter. Finally, there are a large number of objects consistent the brightest objects drawn from a Schechter LF.

It is possible that the second "locus" arises from some as yet-unascertained systematic error in the photometry. It is extremely unlikely that clouds could have produced such a homogeneous offset over several nights; the effect is too large for simple haze or variations in atmospheric extinction. The effect shows up in data obtained from both cameras and is therefore unlikely to have been the product of a amplifier gain error. I have checked several cases to eliminate the possibility that poor background subtraction is responsible for the difference. If the second-ranked galaxies are plotted as well (open points) they are found to have a range of absolute magnitudes up to the fainter "locus", suggesting that the brightest galaxies falling on the fainter locus are actually the second-ranked galaxies in the cluster. Either

the true BCGs lie outside the area of the cluster imaged in the survey (as was found several times to be the case), or somehow a true BCG was prevented from forming. What remains well defined is a gap of about 0.45 magnitudes between the BCG and the next-brightest galaxy.

Because of the small size of the photometric sample, and the fact that there appears to be only a secular trend of luminosity with redshift, I do not try to search for any correlation of M_1 with cluster properties. Instead, I examine the distribution of cluster properties for those with BCGs and those (apparently) without. In Fig. 16 I plot the distributions with Bautz-Morgan and Rood-Sastry types, and with the concentration and relative peak indices. Because of the small number of clusters in the photometric sample it is difficult to distinguish the two distributions, although the BCG sample does tend towards earlier (more evolved) types. There appears to be a tendency to find BCGs in lower-numbered Bautz-Morgan type clusters, per definition. This may either mean the appearence of a BCG in a cluster is unrelated to its morphology, or, less likely, that there are BCGs in most of these clusters, but that a large fraction of them are falling outside the field of view of the CCD imaging.

2.5.1 The $M_1 - M^*$ Differential

As discussed in Ch. I, the magnitude difference between the brightest cluster galaxy and the characteristic galaxy magnitude $M_1 - M^*$ is a photometry-independent, distance-independent (except for small differences in K-correction between the BCG and bright galaxies) quantity that is also of great significance to galaxy evolution models. As an interesting aside, in Fig. 17 I plot $M_1 - M_2$ vs. $M_1 - M^*$ (M^* determined with a fixed α) for all clusters. These quantities are independent since here the fitting for M^* excludes the brightest two galaxies. The clusters occupy a locus which is well-defined at the bright M_1 end, but poorly defined at the other. I estimate the values expected from a Schechter LF with the normalization varying over the range of reasonable cluster richness (10 and 1000 galaxies brighter than $M^* + 3$). The solid curve is the region that include 90% of the Monte Carlo points. The Schechter LF occupies a distinct and separate part of this space and the simulations demonstrate

that nearly all of the M_1, M_2 pairs here cannot be drawn from a Schechter LF, i.e. that the brightest galaxies in the cluster are not drawn from such a distribution.

Plots of $M_1 - M^*$ (Fig. 18) demonstrate a weak correlation between this parameter and the cluster morphology in that more relaxed clusters tend to have larger differences that asymptote to a value that I define as a BCG. This is clearly consistent with a picture of a BCG growing with time in a cluster, e.g., through cannibalism of other galaxies. The scatter is large; a larger photometric sample to suppress the cluster-to-cluster error in the estimation of M^* is obviously needed. Since M^* brightens at most only slightly that the value M^1 is responsible for most of the variation, as is demonstrated in Fig. 19.

2.5.2 Discussion

The first-ranked cluster galaxies, and possibly the second-ranked, are shown to be distinct from a population drawn from a Schechter distribution. It appears that many of the CCD fields exclude the BCG (due to offsets between the cluster centers in the Abell catalog and the BCG locations). The first-ranked galaxies are ~ 0.5 magnitudes brighter than all other galaxies and can more or less by identified by that characteristic. They exhibit a tight correlation between absolute luminosity and redshift, showing a brightening of about 0.6 magnitudes by $z = 0.35$. The extrapolated $z = 0$ value of M_1 is -23.25, consistent with estimates by Postman & Lauer (1995). The very small scatter in BCG magnitudes (if the secular luminosity evolution can be removed) reinforces their value as "standard candles" for distance measurement. The appearence of a BCG is correlated with the morphology of the cluster, suggesting that these objects have evolved (perhaps by cannibalism) over the age of a cluster but asympotote to some luminosity after some period of time and only passively evolve further.

I compare the evolution of the ACG absolute magnitude with the models of Buzzoni (1995). The predicted luminosity evolution is sensitive to the assumed shape of the Initial Mass Function (IMF) and insensitive to the metalliticty thus a sample of passively evolving limit objects (such as these might be) can be used to constrain

the IMF in elliptical galaxies. Buzzoni's models assume a single starburst at $z = \infty$ with a power-law IMF of slope $-s$. The absolute magnitude evolution with elapsed time is given by the empirical relation,

$$\frac{dM}{dt} = C - 0.27(s-1), \tag{2.22}$$

[also (Tinsley & Gunn 1976)]. The elapsed time in an $\Omega < 1$ and $\Lambda = 0$ universe is

$$t = H_0^{-1} \frac{\Omega_0}{2(\Omega_0 - 1)^{3/2}} \left[-\cosh^{-1}\left(\frac{\Omega_0 z - \Omega_0 + 1}{\Omega_0 z + \Omega_0}\right) + \frac{2\sqrt{(1-\Omega_0)(\Omega_0 z + 1)}}{\Omega_0 (1+z)} \right] \tag{2.23}$$

I plot the Buzzoni predictions for three different values of s (1.35, 2.35, 3.35) as the dashed lines in Fig. 15. The data would appear to be more consistent with steep evolution in the model with a very flat IMF, i.e., dominated by massive stars. It is difficult to draw any strong conclusions from this since there are relative few BCGs in the sample, the range of redshifts is small, and no complementary color information is available. Note that choosing a larger value of q_0 makes objects appear closer, decreasing their luminosity, but also makes the elapsed time less, lowering the predicted luminosity of the models. An alternative would be a younger age for the BCG stellar populations, perhaps produced during the merger and cannibalism of other bright galaxies.

Finally, I fit a simple form of evolution to obtain a best-fit and remove the redshift dependence. Assuming exponential decay of luminosity in an Einstein-de Sitter universe, and excluding A2244, I find the best fit of the remaining 10 BCGs to be

$$M_1(z) \sim -23.25 - 5.0\left[1 - (1+z)^{-2/3}\right] \tag{2.24}$$

the residual scatter is 0.06 magnitudes about a mean of -23.31, or $1.1 \times 10^{11} L_\odot$. This is indistinguishable from the expected random error due to errors in surface brightness profile fitting (0.04 magnitudes), galactic extinction (0.02 magnitudes), and atmospheric extinction (0.01 magnitudes). Using the same luminosity evolution, I find the absolute magnitude of the second-ranked galaxies to be 0.47 magnitudes

fainter.

2.6 Morphology of Cluster Galaxies

2.6.1 The Technique

My objective is to characterize cluster galaxy populations as a whole, rather than attempt to accurately classify individual galaxies. If accurate, quantitative measurements of the former can be obtained, a comparison with indicators of cluster age or dynamical state would be a test of the hypothesis that galaxies evolve in clusters over time, going from a disk-dominated population to a spheroidal population. I build on previous work (Okamura *et al.* 1984; Doi *et al.* 1993; Abraham *et al.* 1994) and exploit the fact that the surface-brightness profiles of disk-like galaxies are more extended and flattened (when not seen exactly face-on) compared to spheroidal systems. I calculate a photometry- and scale-independent quantity that is the difference of the principle moments of inertia normalized by the isophotal area. In terms of the moments of inertia M of the surface brightness in image coordinates;

$$Q = \frac{\sqrt{(M_{xx} - M_{yy})^2 + 4M_{xy}^2}}{A}, \tag{2.25}$$

where A is the isophotal area. A low value of this parameter indicates the object is concentrated and/or round, i.e., an early type galaxy, while a large value indicates a disk galaxy. Since this quantity only measures the surface brightness morphology and not other qualities such as color, S0-like galaxies will be classified as disk systems.

Fig. 20 is a "Hubble Atlas" of bright galaxies in Abell 2266 at $z = 0.1671$. Two-thirds of the clusters in our survey are closer than this object, although the "seeing" while these images were obtained was better than average ($\sim$ 0.85 arcseconds). The galaxies are arranged in order of decreasing Q from top left to bottom right. The top eight objects have the largest Q values in the image, and the bottom eight have the smallest. Disks systems, especially those seen edge are, and systems with spiral arms are clearly distinguished from spheroidal systems. The two objects

which appear to be "out of sequence" are (second row, left) a galaxy whose isophotes are contaminated by a larger galaxy, and (bottom row, second from left) a barred spiral which is nearly face on and has a high central surface brightness, possible indicating nuclear activity.

The two most significant systematic errors are the finite "seeing" or telescope resolution when the images are acquired, and the surface brightness of the detection isophotes. The redshift of the cluster will enter into both effects; the linear resolution becomes poorer with increasing redshift and the rest-frame threshhold surface brightness becomes brighter. The net effect of variation in resolution is not intuitively obvious. Poorer seeing will reduce the quadrapole moments of flattened disk systems by making them appear rounder. On the other hand, the centrally concentrated profiles of spheroidal systems will become more diffuse and their quadrapole moments may increase as long as they are slightly flattened. When estimating the preponderance of disk versus spheroid systems in individual clusters, it is clearly desirable to use a statistic that is robust to modest variations in these seeing and surface-brightness limits.

To simulate the effects of seeing I convolved the Abell 2266 images obtained in 0.7-1" seeing with a $\sigma = 1''$ Gaussian filter to bring the effective resolution to 1.4". It was necessary to add noise to the images to restore the background noise to the original level. Galaxy catalogs are generated from the degraded images and matched with the original catalogs. Fig. 21 shows a subsection of an image near the cluster core demonstrating the effects of the poorer resolution. The quadrapole moments from the original and degraded galaxy catalogs are compared in Fig. 22. The results are encouraging; even with significant degradation the Q-values for most objects with $log_{10}Q$ greater than -1.5, i.e., the most extended and flattened objects, are remarkably preserved. To simulate the effects of a brighter rest-frame surface brightness threshhold I simply add sufficient noise to the original images to raise the detection threshhold by a complete magnitude. A comparison of the brightest objects shows that there appears to be a small effect in the direction of increasing Q, but that it only a few percent. Finally, I add insult to injury by reducing the surface

brightness sensitivity in the smoothed image by a magnitude as well.

The highest Q objects will be the disk systems observed at oblique angles or nearly edge-on. These are the "tip of the iceberg" since there will be other disk galaxies inclined at less favorable angles which reduce their quadrapole moment. I consider a simple model consisting of randomly oriented disks with identical exponential profiles . There are several competing effects as the inclination of a disk is varied; the disk becomes flatter, increasing Q, but the surface brightness increases, moving the limiting isophote outwards and decreasing Q. For a disk inclined at an angle θ (where $\theta = 0$ is face-on),

$$Q = \frac{\sin^2\theta\,[6 - \exp(-X)\,(6 + X + 3X^2 + X^3)]}{X^2\,[1 - \exp(-X)\,(1 + X)]} \tag{2.26}$$

where X, the scaled radius of the limiting isophote obeys,

$$X = -X_0 \ln\cos\theta \tag{2.27}$$

and X_0 is the limiting isophote in the face-on case. The distribution with Q is plotted in Fig. 21 and is sharply peaked at $Q{\sim}0.25$. High values of Q (order unity and greater) would not be observed due to the effects of seeing and the disks having finite thickness.

The paucity of model disk systems with $Q < 0.03$ and the apparent robustness of measured Q values above this threshhold suggest that this would be a useful criterion for estimating the relative number of disk galaxies versus spheroids in clusters. I define the quantity F_Q as the fraction of galaxies more luminous than $M_R = -17.41$ and with $\log Q > -1.5$ and calculate this using the catalogs from each cluster. Note that F_Q is not truely the relative fraction of disk galaxies since there will be systematic scatter of disk systems out of the cutoff but it is encouring that the numbers derived are representative of previous estimates of the spiral/S0 population in clusters (Whitmore *et al.* 1993).

2.6.2 Application to the Data

Five clusters (A1661, A1990, A2142, A2213, and A2235) were observed twice and the data reduced independently. A value of F_Q was obtained from each catalog and the RMS variation between measurements of the same cluster was found to be 0.029. The median number of bright galaxies per cluster is 110, and F_Q is typically ~ 0.3, and thus the Poisson noise from the finite number of disk-like galaxies is typically 0.05 and the random error dominates any systematic error. (Some of the systematic variation is probably due to different sizes of the field of view.)

In Fig. 23 F_Q is plotted with redshift. A χ^2 test of all clusters gives a mean of $\bar{F_Q} = 0.280 \pm 0.005$ and a reduced χ^2 of 2.39. The scatter is thus marginally consistent with the estimated errors. To test for any secular variation with redshift I divide the objects into two bins of equal number (at $z = 0.138$) and apply the Kolmogorov-Smirnoff test. I find that there is 6.9% probability that the two subsamples are drawn from the same population so that the results are inconclusive. As a final test, I bin the clusters into four redshift bins of 21, 18, 15, and 13 clusters (to partially compensate for the larger errors at low redshift) and compute the average F_Q in each bin. These are plotted as the solid, connected points along with the data (the redshift of the bin was chosen to be the median value of the constituent clusters). A systematic trend with redshift appears, such that the higher redshift clusters tend to be more disk rich. Without additional information (such as colors) it is not possible to rule out a systematic error or selection effect. For example, the Abell catalog is very biased towards richer clusters with increasing redshift and if there was a correlation with richness and galaxy type (I show below there is no evidence for this) this would manifest as such a trend.

It is tempting, however, to associate the trend with the well-known Butcher-Oemler effect, where cluster populations become bluer at redshifts $z > 0.2$. The difference between the lowest- and highest-redshift bins is 0.25 ± 0.07 of the average. In an Einstein-de Sitter cosmology, the elapsed time between the median redshifts of the bins is 0.88 h^{-1} Gyr. If the observed trend were due to disk galaxies being destroyed or transformed into early-type galaxies, a half-life of $2.1 \pm 0.8 h^{-1}$ Gyr is

implied.

Figs. 24 and 25 are plots of F_Q versus the various morphological parameters described in §2.3.2. There appears to be no correlations with an of these cluster indicators.

In summary, the use of the difference of the principle moments Q of the surface is a potentially powerful technique to distinguish between disk and bulge systems to moderate redshift (~ 0.2) and it is robust to mild changes in seeing or noise level. A simple model of randomly oriented disks suggests a cut-off value to separate the two classes of systems. Although this technique has not yet been calibrated with images of galaxies of known morphological types, an application to the data here finds that the average fraction of disk-like systems is 30%, close to typical values reported in the literature (Whitmore *et al.* 1993). A search for a variation in the fraction with redshift finds a marginal detection of an increase in disk systems at $z > 0.2$, consistent with the expected Butcher-Oemler effect (Butcher & Oemler 1984). The utility of the technique could be greatly enhanced by combing it with color information to distinguish between S0 disk systems and late-type spirals.

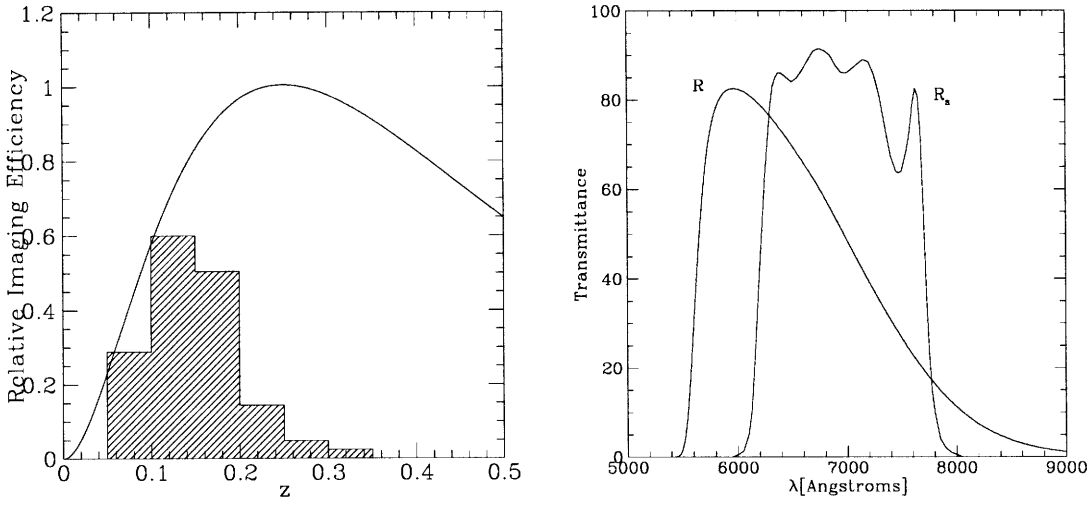

Fig. 1.— Survey redshifts and filters
Left: Relative imaging efficiency (galaxies observed to a fixed rest-frame surface brightnes limit per unit time) versus redshift for elliptical galaxies in clusters with θ^{-1} projected profiles. The distibution of survey clusters with redshift is shown; **Right:** transmittance plots of the two filters used in the survey.

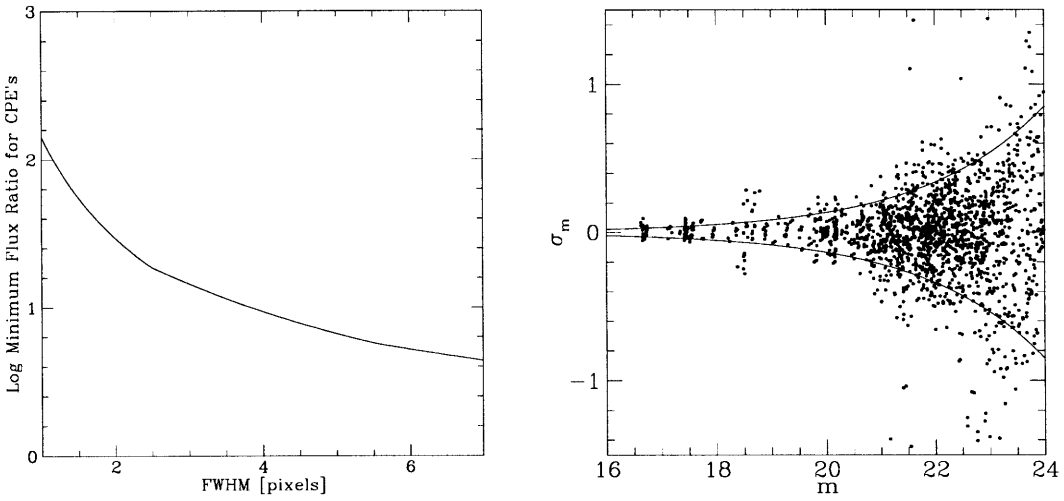

Fig. 2.— CPE rejection criteria and magnitude errors
Left: Minimum allowable charged particle event flux ratio rejection threshhold versus FWHM of the image point-spread function before object photometry is compromised. **Right:** Galaxy photometry errors from 322 galaxies that were multiply imaged and analyzed in the field of Abell 1632. The curves are the adopted 1σ errors.

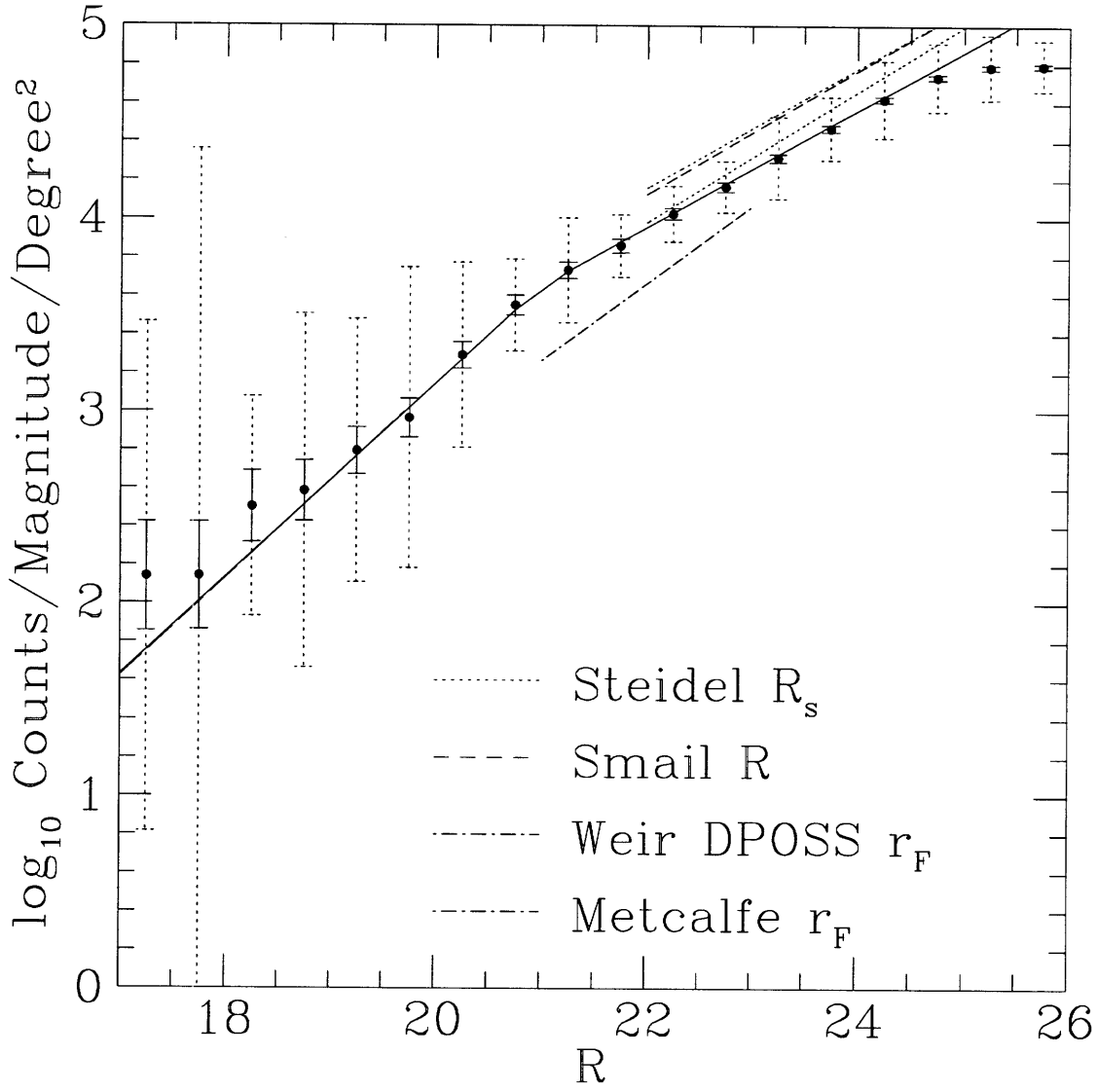

Fig. 3.— Field galaxy counts

R_s-band galaxy counts from six 100-square arc-minute fields. The solid error bars are the Poisson errors in the mean; the dashed error bars are the RMS field-to-field scatter. The solid line is the maximum-likelihood fit over the range $R_s < 19 < 24$. Number counts obtained by other researchers are shown for comparison. The line for the bright Weir counts is very difficult to see because of the good agreement!

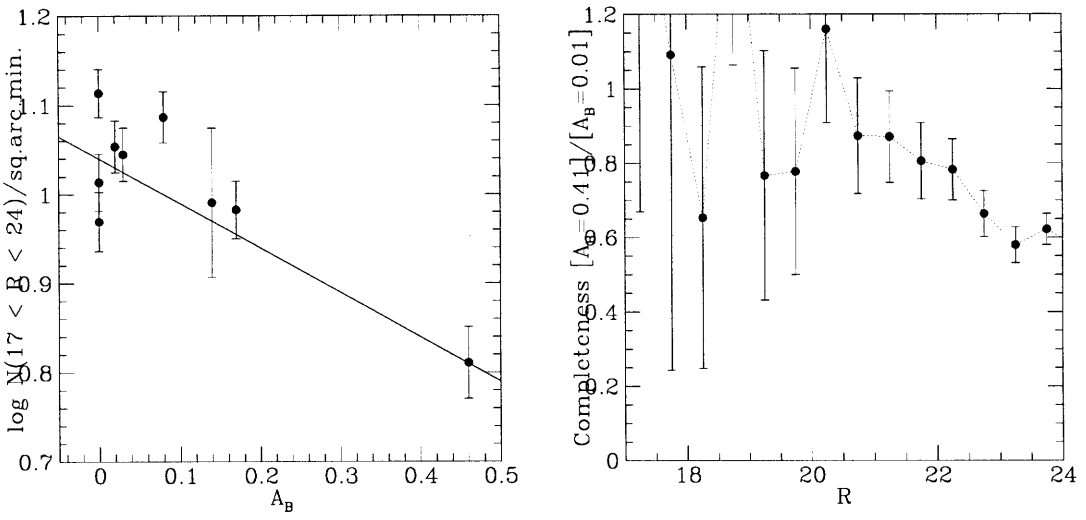

Fig. 4.— Effects of Galactic extinction
Left: Total $17 < R < 24$ counts versus Galactic extinction A_B before any corrections are made. The line is the best-fit value $\log N = C - 0.47 A_B$. **Right:** Relative completeness of $A_B = 0.41$ field with respect to an average of 5 fields with $< A_B >= 0.01$, after the magnitudes have been corrected for extinction.

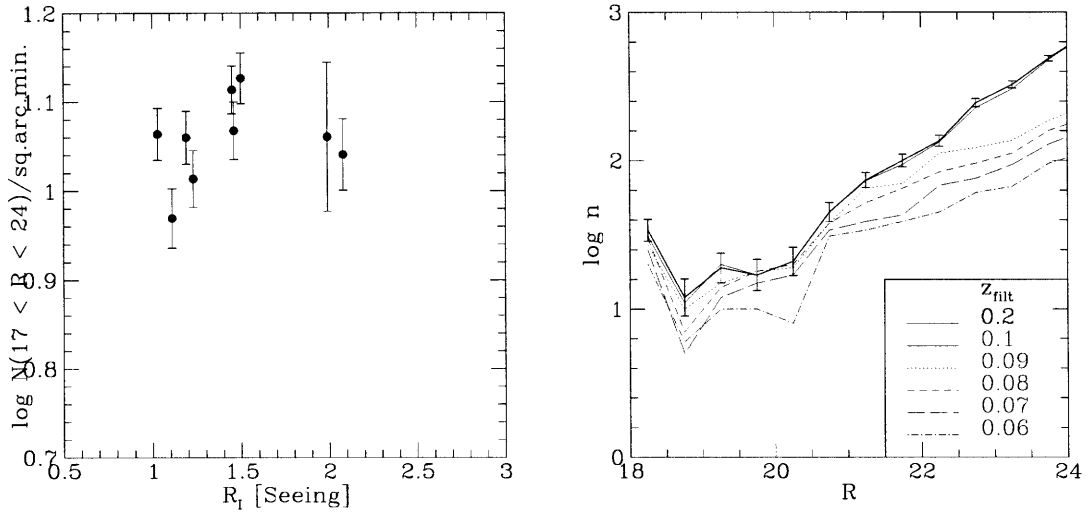

Fig. 5.— Effect of seeing and detection filter width
Left: The effect of seeing (as measured by the radial moment I_r of the point-spread function) on the normalization. **Right:** The effect of varying the width of the detection filter (inversely with the redshift given here) on the number counts of detected galaxies;

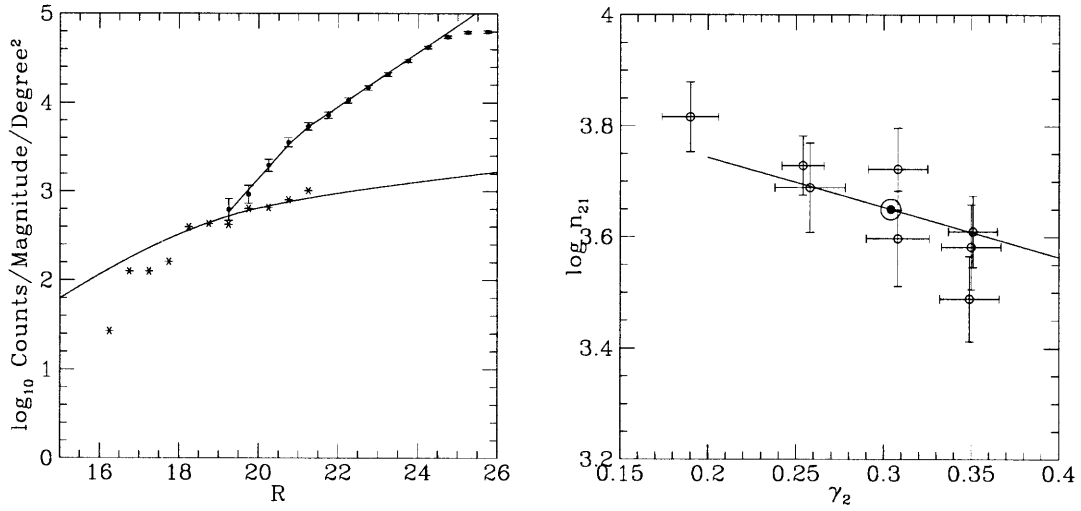

Fig. 6.— Average star counts and background model parameter covariance **Left:** Comparison of galaxy number counts with predicted [model of Bahcall & Soneira (Bahcall & Soneira 1981)], and actual star counts (stars), show that at $R > 21$ the star counts are much smaller than the galaxy counts. **Right:** Normalization of the field galaxy count model at $R = 21$ versus the maximum likelihood faint-end slope γ_2 over the range $21 < R < 24$ for the eight 100 square-arc minute background fields. The error bars are the 68% confidence limits from Monte Carlo simulations of the data. The solid point is the maximum-likelihood parameter pair obtained from the cumulative data, and the locus is the predicted variation in the case of constant $21 < R < 24$ counts.

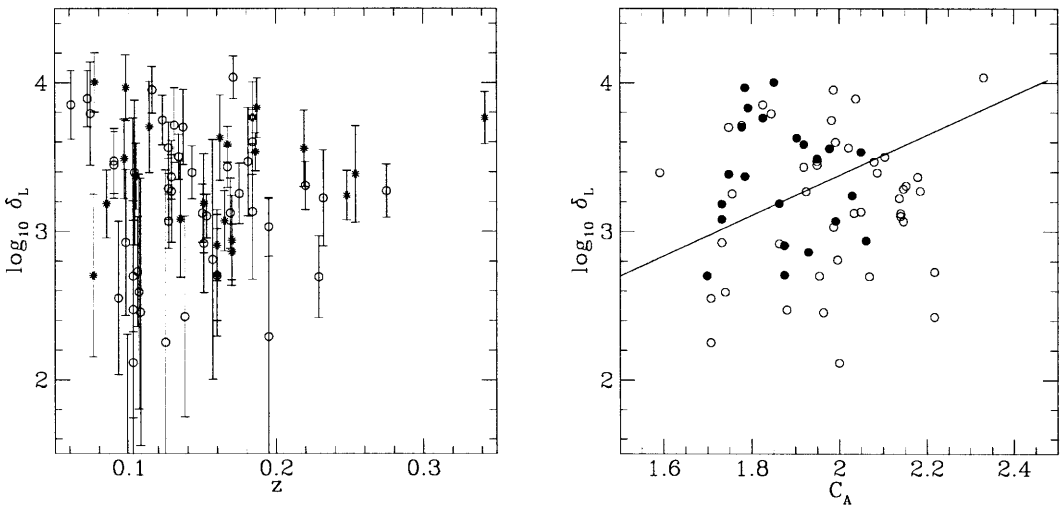

Fig. 7.— Cluster luminosity overdensity
Left: Luminosity overdensity δ_L within 0.5 h^{-1} Mpc of the cluster center versus redshift. Solid points are photometric data. **Right:** Comparison of δ_L with Abell galaxy counts C_A within 1.5 h^{-1} Mpc. The line is the predicted relation if the clusters have r^{-2} profiles and Schechter LFs. Error bars have been omitted for clarity.

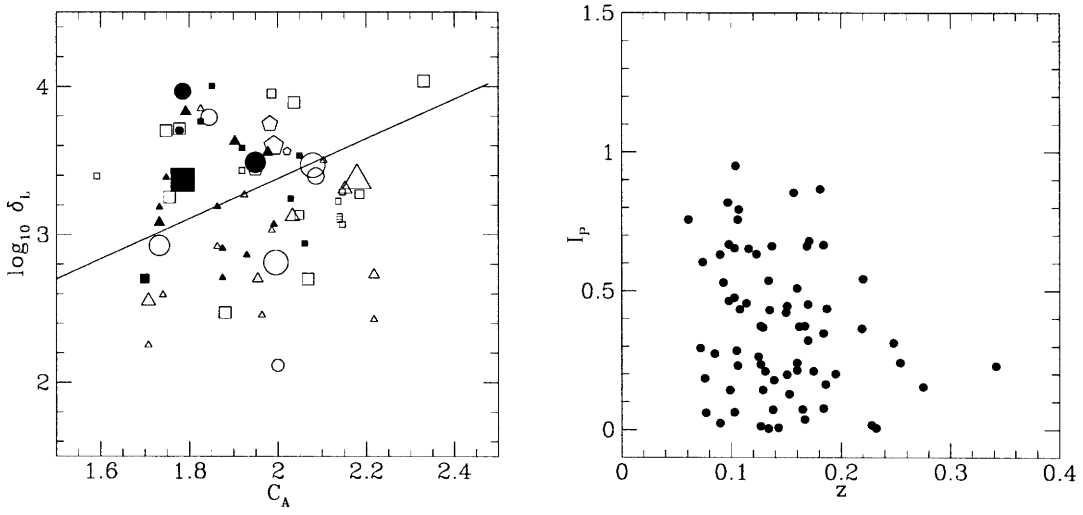

Fig. 8.— Cluster luminosity overdensity and peak index
Left: Luminosity overdensity δ_L within 0.5 h^{-1} Mpc of the cluster center versus logarithm of the Abell counts. Points are encoded as follows; solid points are photometric data; decreasing in size are Bautz-Morgan types I to III; triangles, squares, pentagons, and circles are Rood-Sastry typese I/F, C/L, B, and cD, respectively. The line is the predicted relation if the clusters have r^{-2} profiles and Schechter LFs. **Right:** Peak index I_P showing the expected bias with redshift.

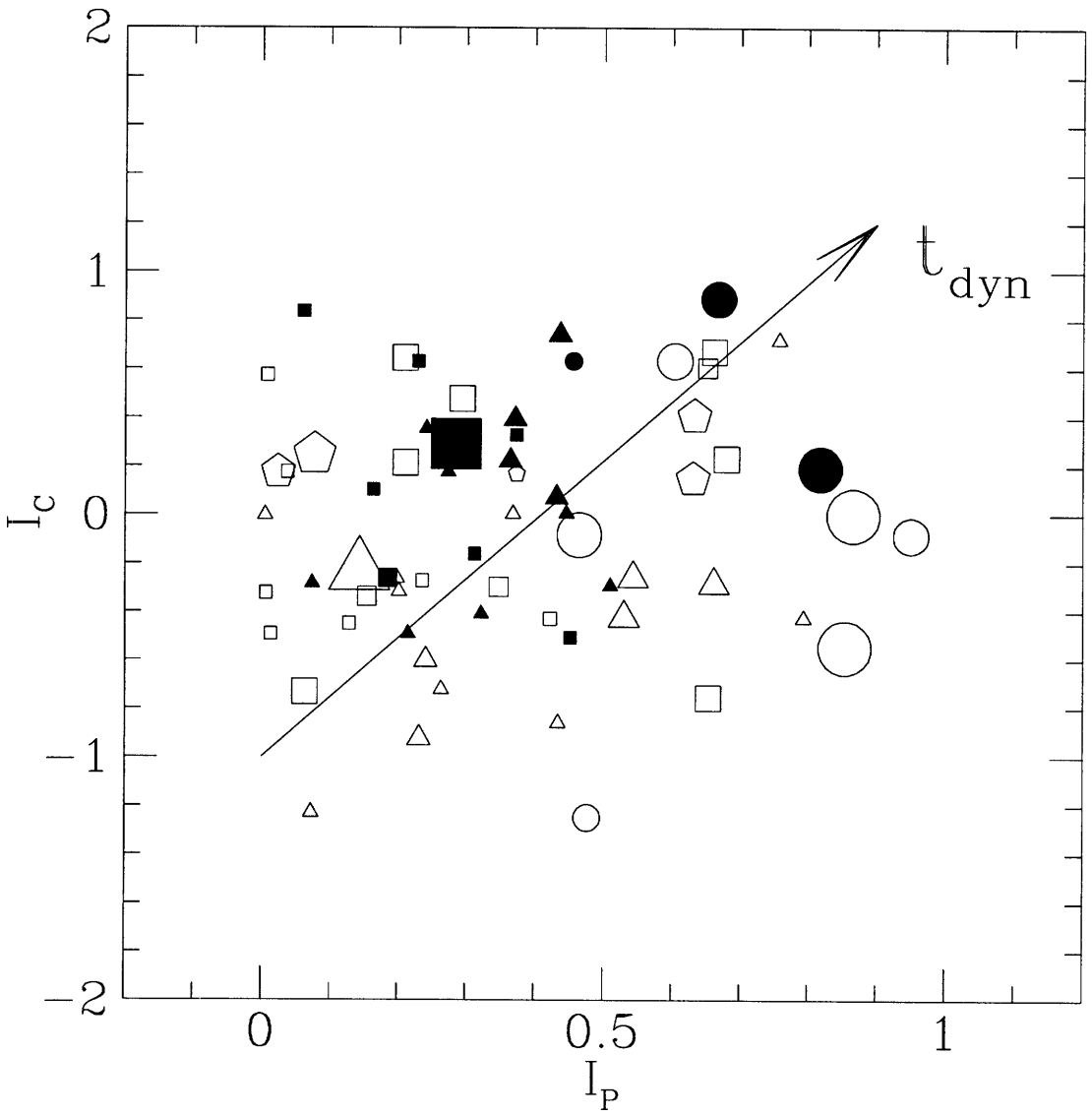

Fig. 9.— Concentration index vs. peak index
Concentration index I_C versus peak index P_I defined in §2.3.2. Points are encoded as follows; solid points are photometric data; decreasing in size are Bautz-Morgan types I to III; triangles, squares, pentagons, and circles are Rood-Sastry typese I/F, C/L, B, and cD, respectively. The arrow indicates the expected evolutionary track of clusters towards a more concentrated, smooth morphology.

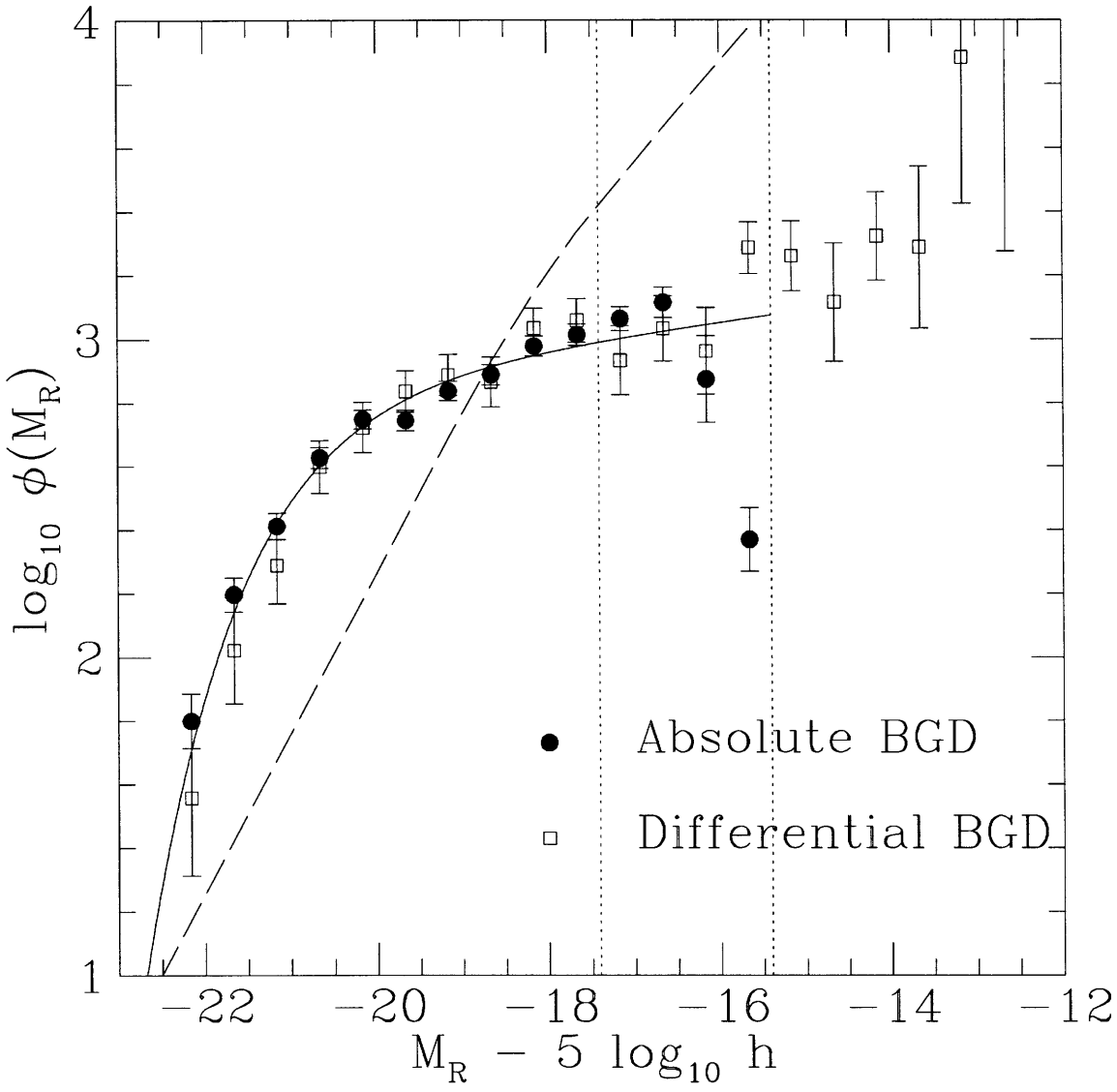

Fig. 10.— Composite luminosity function
Absolute background-corrected LF (solid point) and differential background-corrected LF (open points) from photometric galaxy catalogs of 22 Abell clusters. The best-fit Schechter function ($M_R^* = -21.13$, $\alpha = 1.09$) is plotted. The dashed line is the background contribution on the same scale.

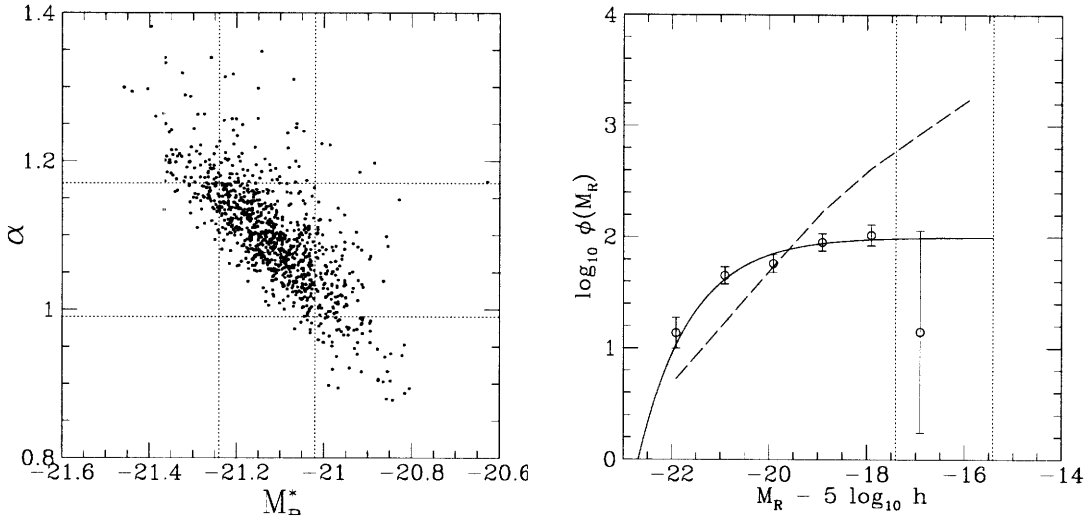

Fig. 11.— Error covariance and LF from outer galaxies
Left: Schechter function parameters from 1000 Monte Carlo simulations of the cumulative photometric data. The circled point is the actual derived value and the dotted lines are the 1σ error-bars. **Right:** Comparison between best-fit Schechter function using the entire data (solid line) with the LF constructed by differencing the galaxies inside and outside 0.75 h^{-1} Mpc from the cluster center. The dashed line is the background level.

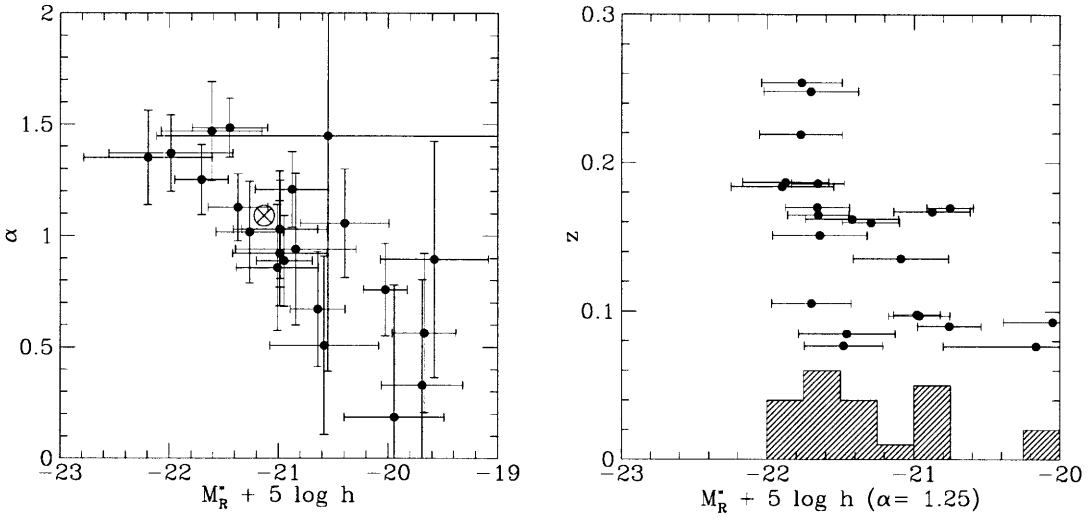

Fig. 12.— Schechter LF parameter for clusters
Left: Best-fit Schechter parameters for 22 Abell clusters with photometric data. The circled X is the point from the cumulative LF. **Right:** Value of M_R^* versus redshift for a fixed $\alpha = 1.25$. A histogram of M^* value is also shown.

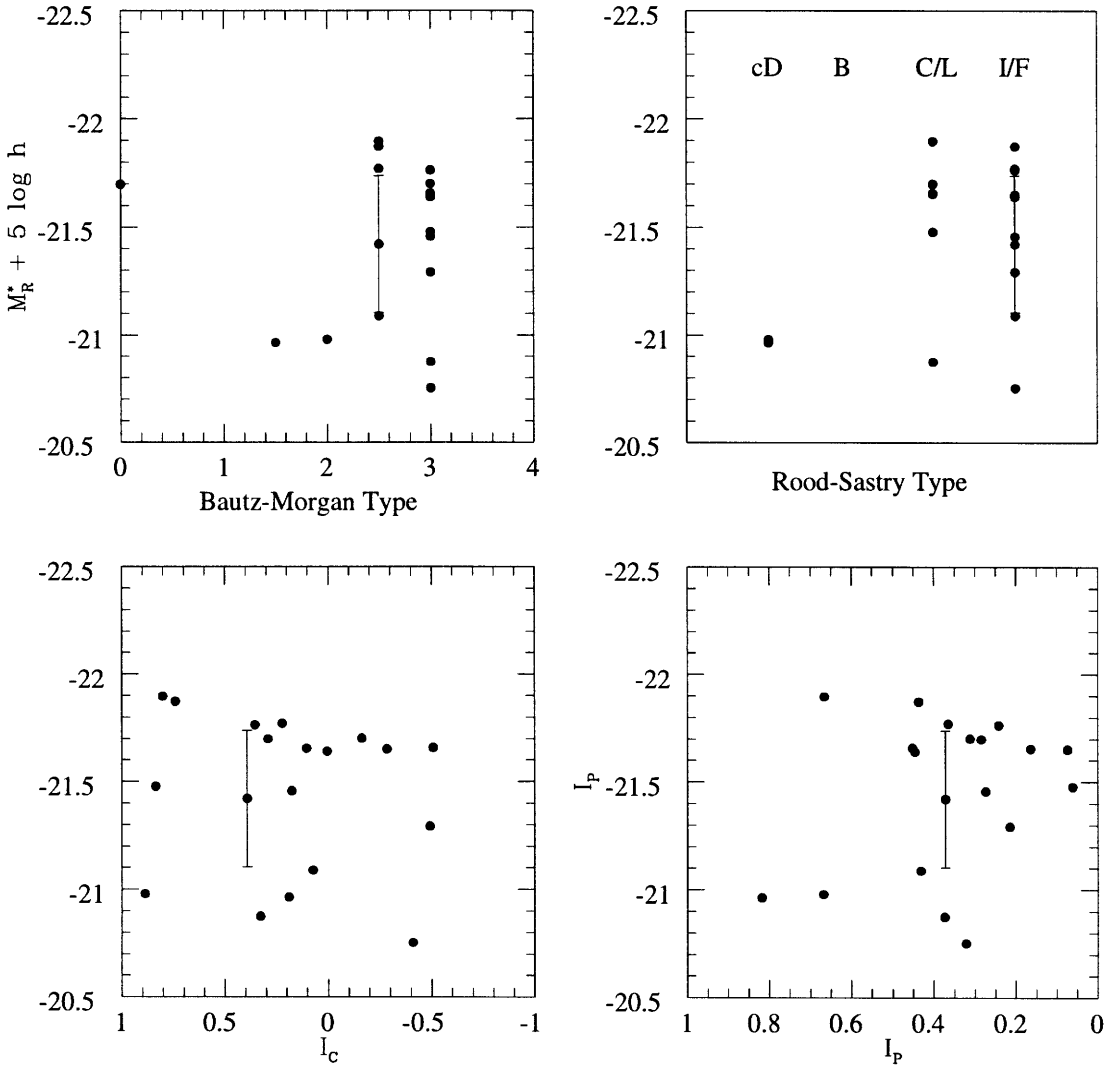

Fig. 13.— M^* dependence on cluster morphology
Characteristic absolute magnitude M_R^* versus Bautz-Morgan type, Rood-Sastry type, and the concentration and relative peak indices derived in the thesis. The plots are arranged such that old more dynamically relaxed clusters would tend to fall towards the left. Only a single, randomly chosen error bar is shown for clarity.

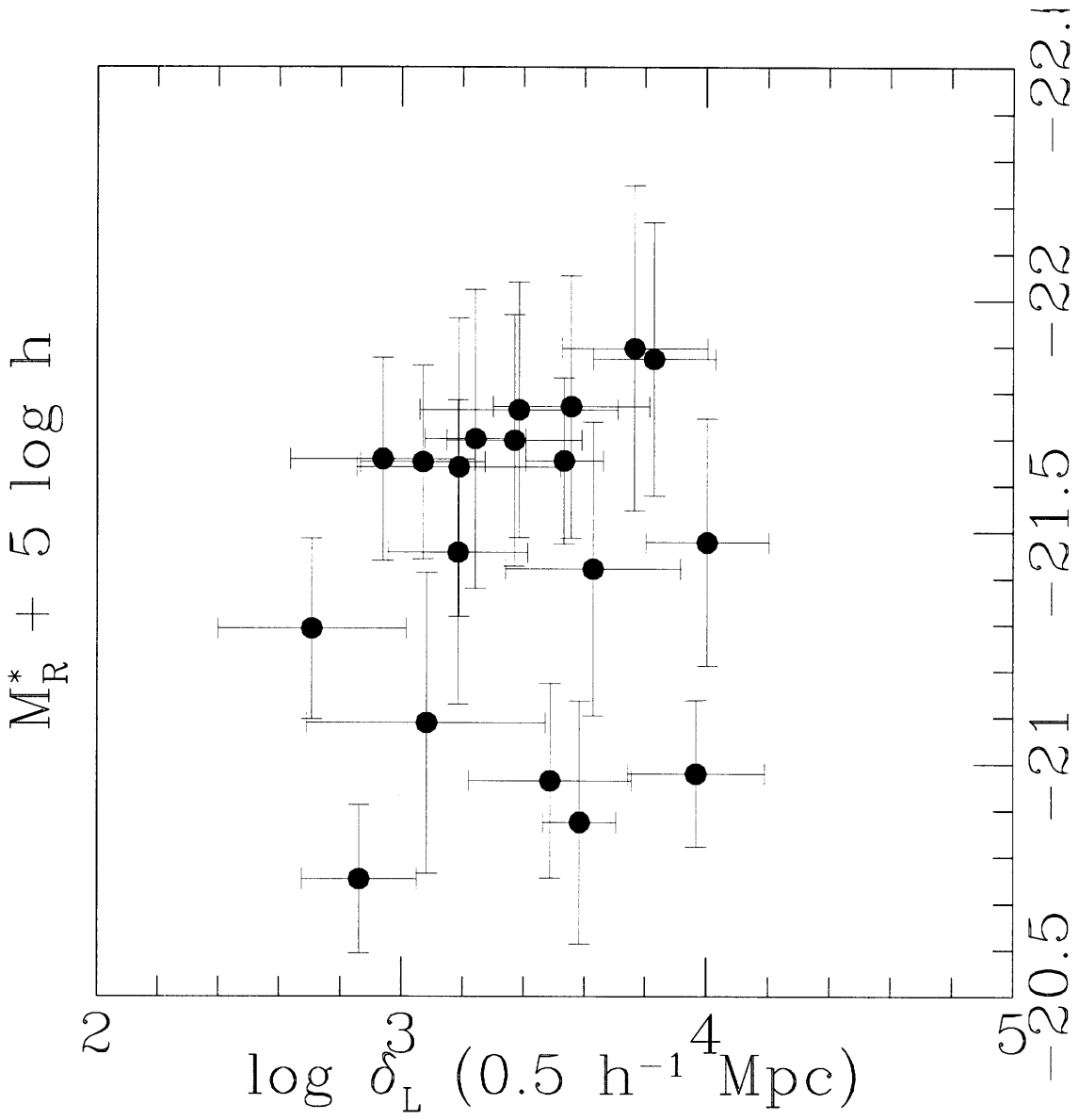

Fig. 14.— M^* dependence on cluster overdensity
Characteristic absolute magnitude M^*_R versus luminosity overdensity with the central 0.5 h^{-1} of the cluster.

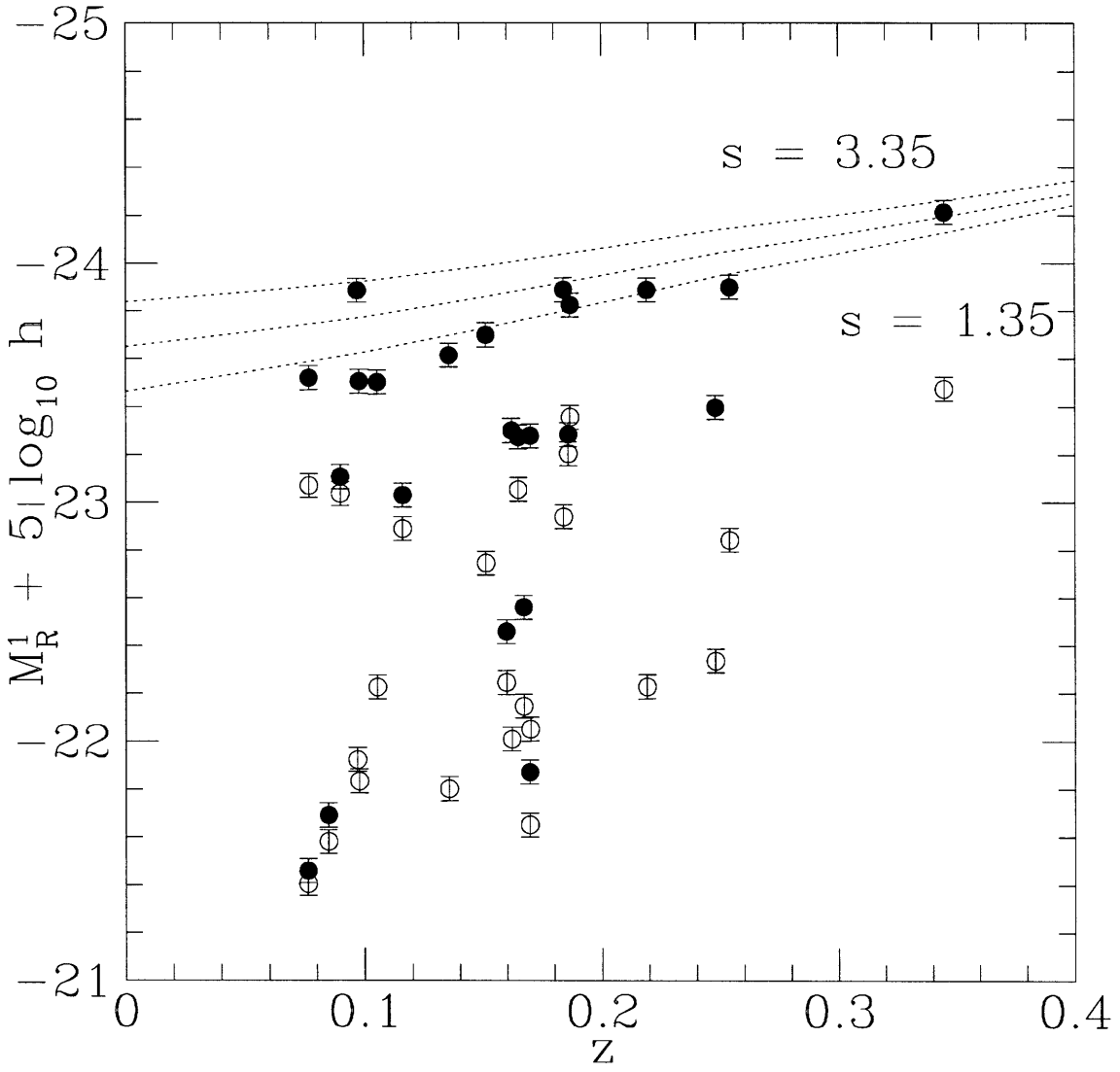

Fig. 15.— BCG magnitudes
Total absolute magnitudes of BCG candidates from 24 Abell cluster galaxies from 24 Abell clusters with photometry plotted against redshift. Filled points are the brightest galaxies in the field of view that do not have disk-like morphologies. Open points are the second brightest. The estimated error of 0.05 magnitudes is shown. The dashed lines are evolutionary models (Buzzoni 1995) with different IMF slopes.

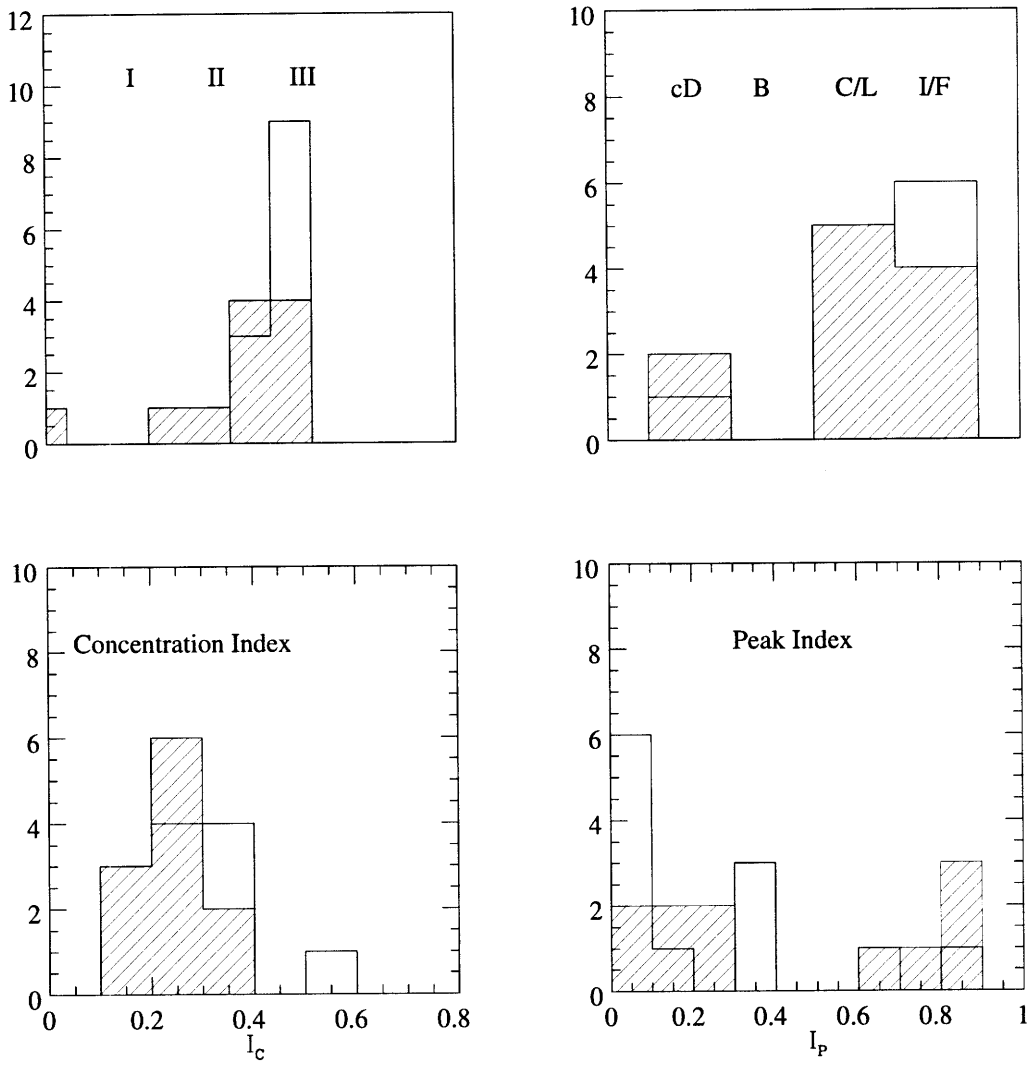

Fig. 16.— Distibution of BCG and non-BCG clusters
Distribution of Abell clusters with (shaded) and without (unshaded) photometrically identified BCGs with Bautz-Morgan type, Rood-Sastry type, concentration index (increasing towards right) and relative peak index (decreasing towards the right, see §2.3.2 for definition).

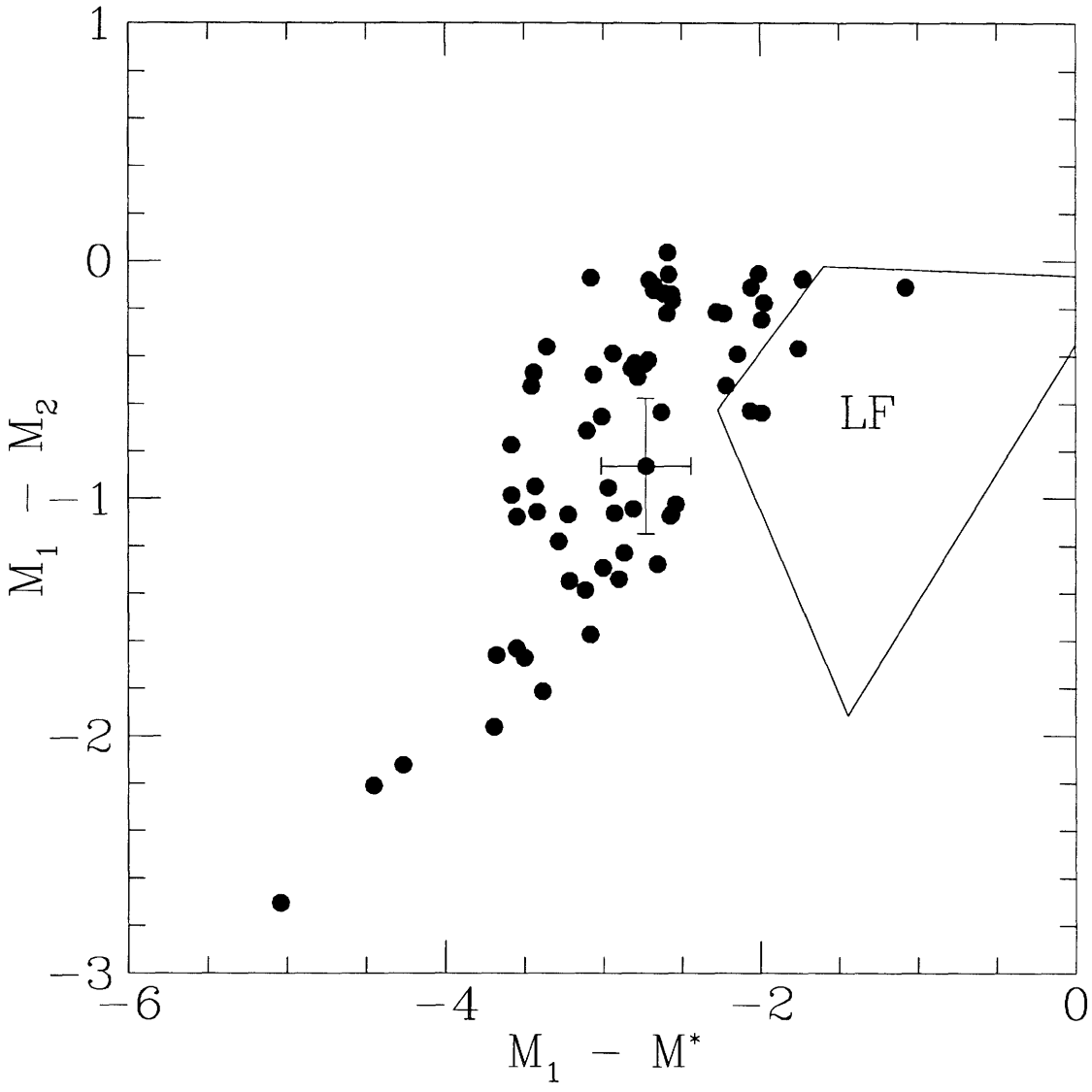

Fig. 17.— $M_1 - M^*$ vs. $M_1 - M_2$
Plot of relative magnitudes of first- and second-ranked galaxies and the characteristic magnitude M^*. The region marked LF is the 90% confidence limits on simulated Schechter-function clusters with a reasonable range of richness.

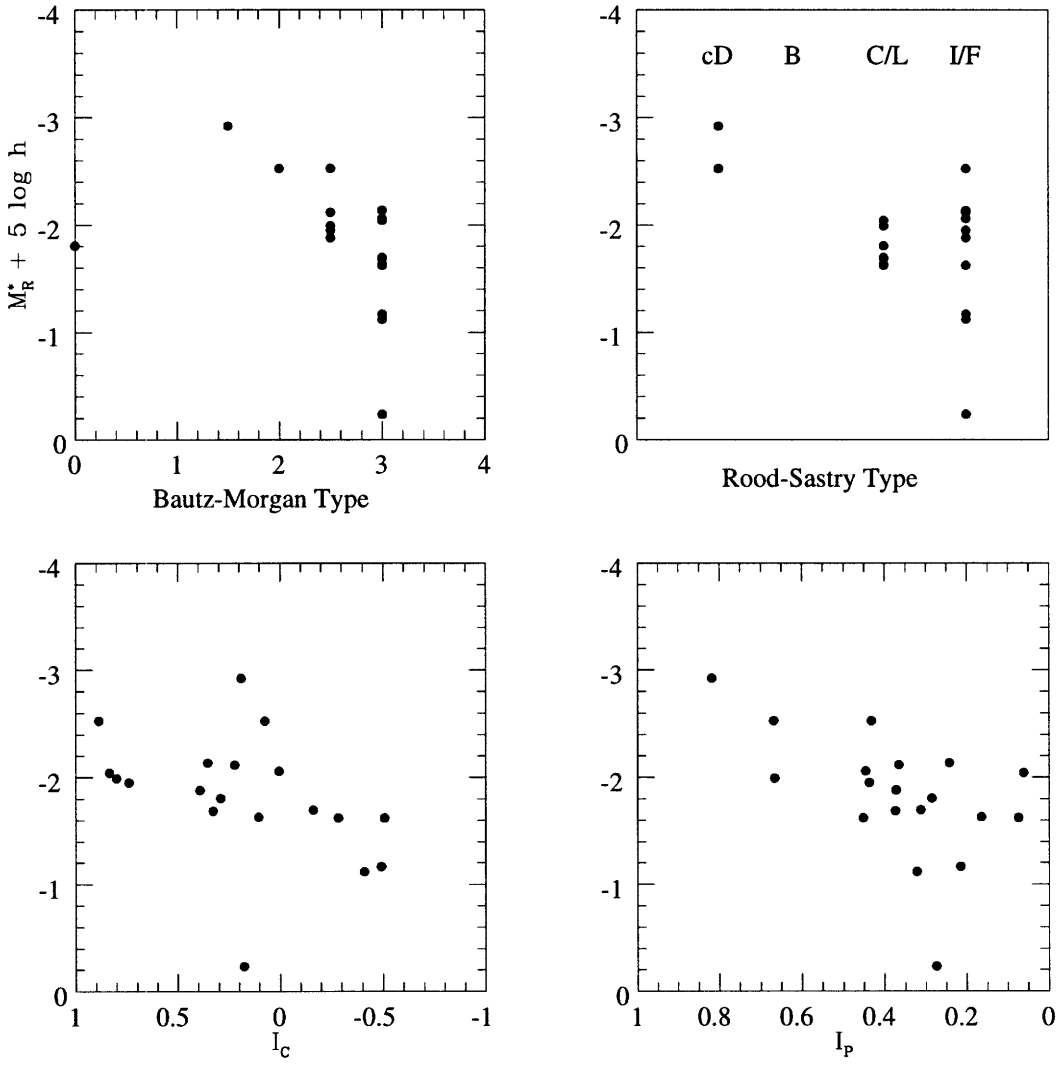

Fig. 18.— $M_1 - M^*$ vs. cluster morphology indices
Correlation of $M_1 - M^*$ with parameters describing the morphology of the cluster (see §2.3.2). The plots are arranged so that more dynamically relaxed cluster would appear on the left.

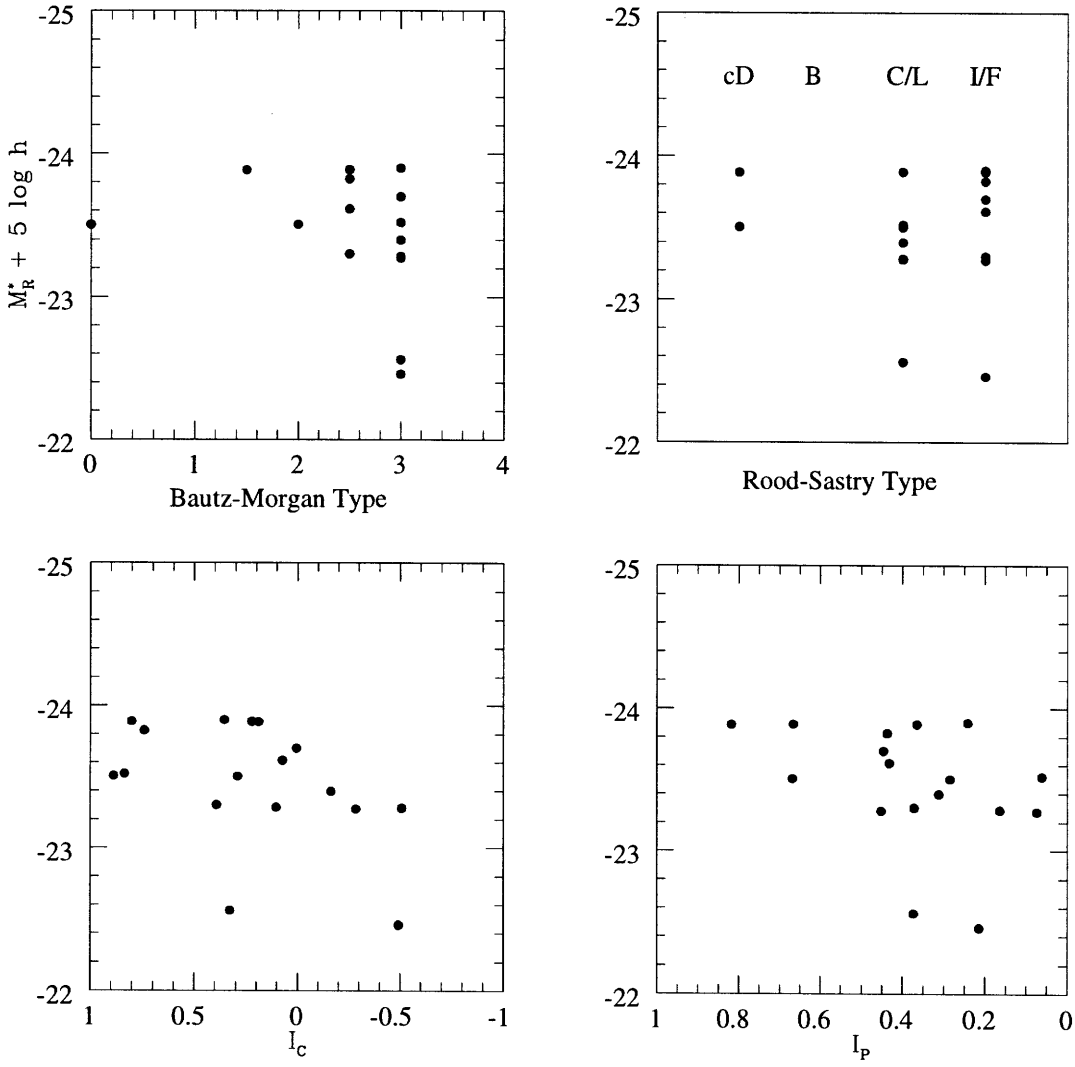

Fig. 19.— M_1 vs. cluster morphologies
Correlation of M_1 with parameters describing the morphology of the cluster (see §2.3.2). The plots are arranged so that more dynamically relaxed cluster would appear on the left.

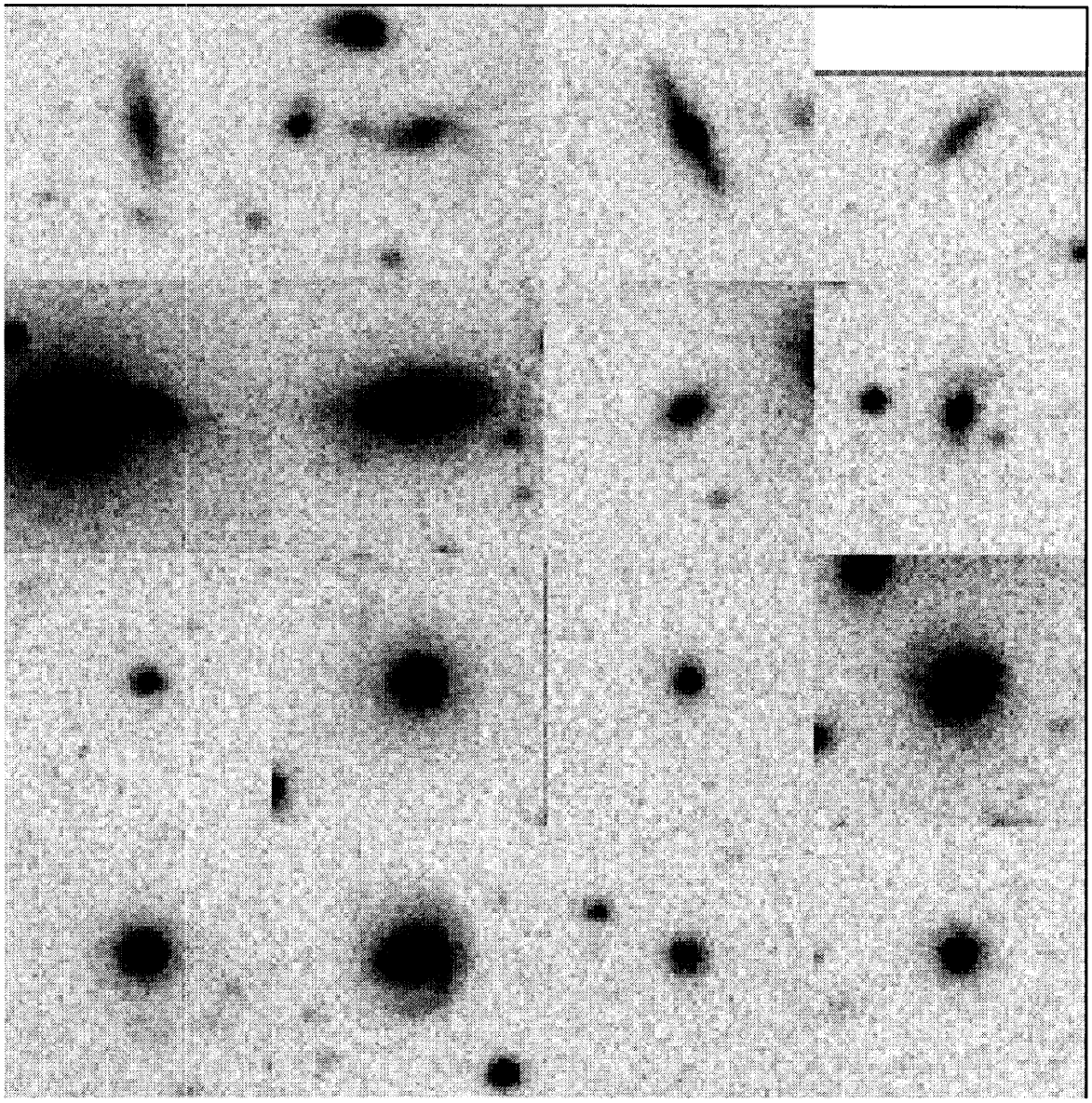

Fig. 20.— Hubble Atlas of galaxy morphologies by Q parameter
"Hubble Atlas" of 16 $M_R < -17.41$ galaxies in Abell 2266 ($z = 0.1671$) observed in 0.8" seeing. The galaxies are ordered with decreasing Q, moving from the 8 most disk-like in the upper left-hand corner to the 8 most star-like in the lower right-hand corner. Each image is 16.8" on a side. Some of the most compact objects may, in fact, be stars.

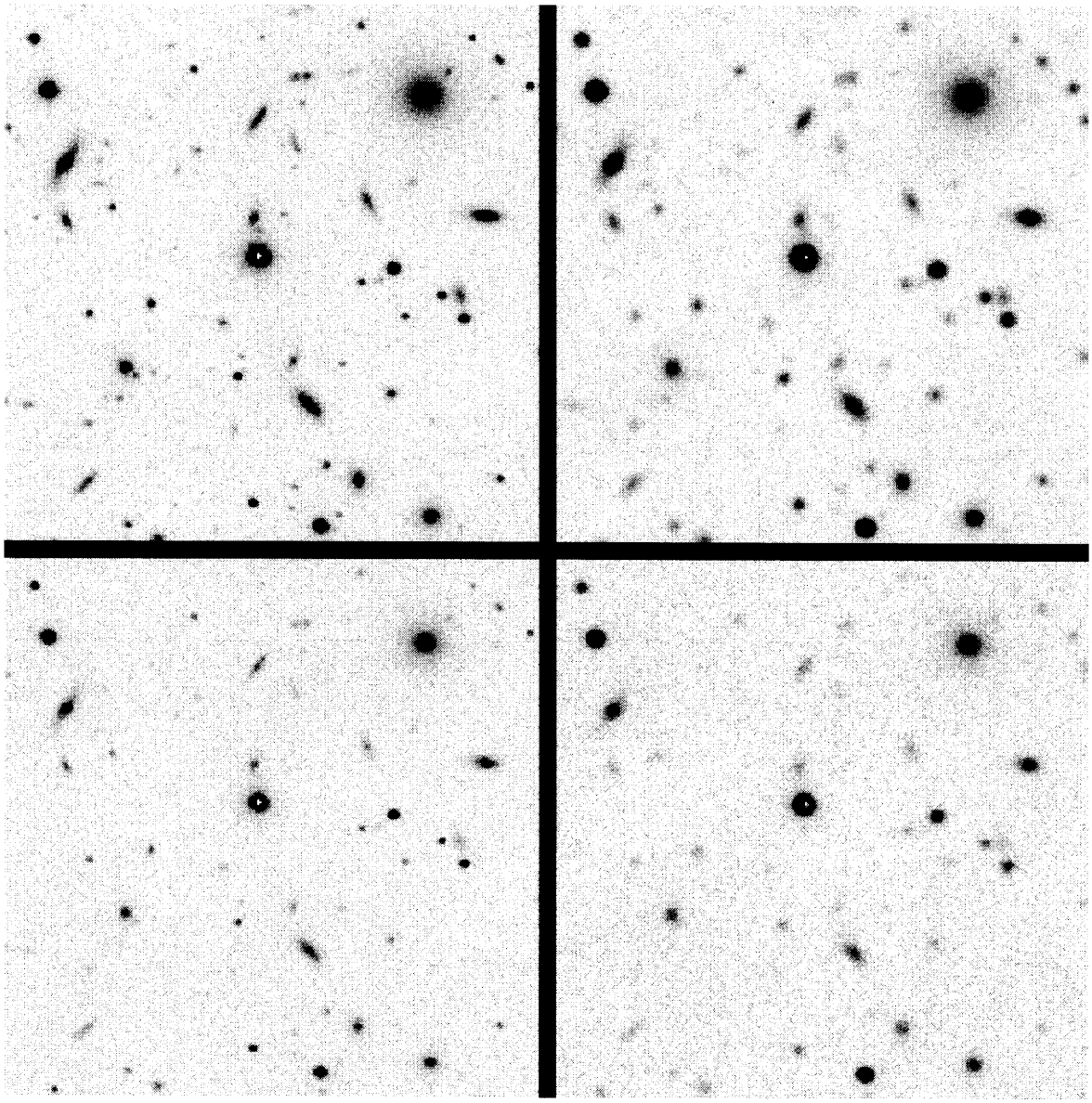

Fig. 21.— Image degradation for test of Q parameter
A 96 × 96 arc-second section of an image of the core of Abell 2266 at $z = 0.1671$. Clockwise from upper left; original image obtained in 0.8" seeing; degrade to an effective seeing of 1.4'; poor seeing and a 1 magnitude brighter surface brightness limit; brighter suface brightness limit only.

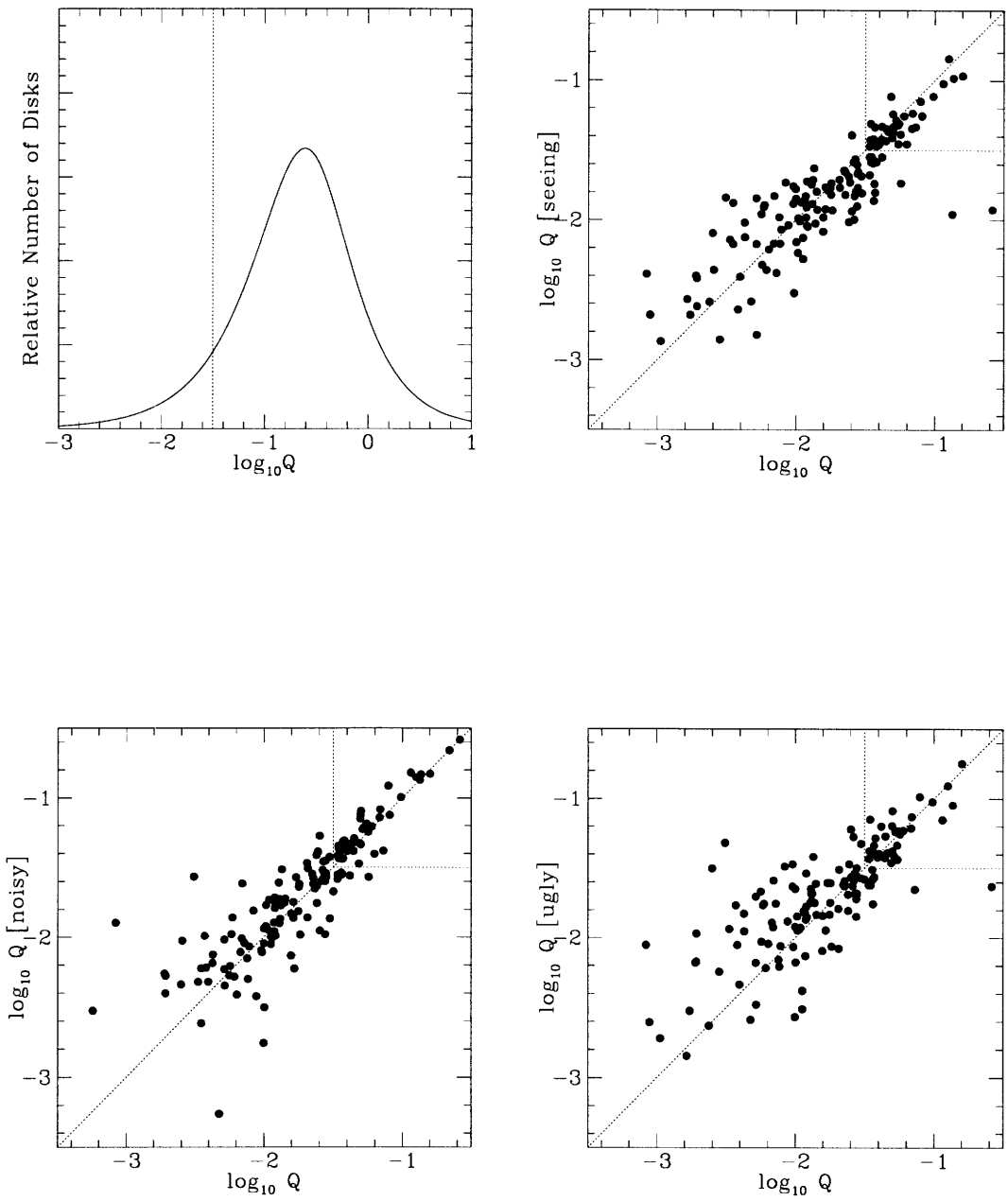

Fig. 22.— Test of Q parameter with image degradation
The three lower right panels compare the values of Q from the corresponding degrade images of A2266 shown in Fig. 21 with the values obtained in the original image. Only galaxies brighter than $M_R = -17.85 + 5 \log h$ are included. The upper left pannel is a plot of the distribution of "toy" disk galaxies with Q. The dashed lines are the adopted cutoff at $\log Q = -1.5$.

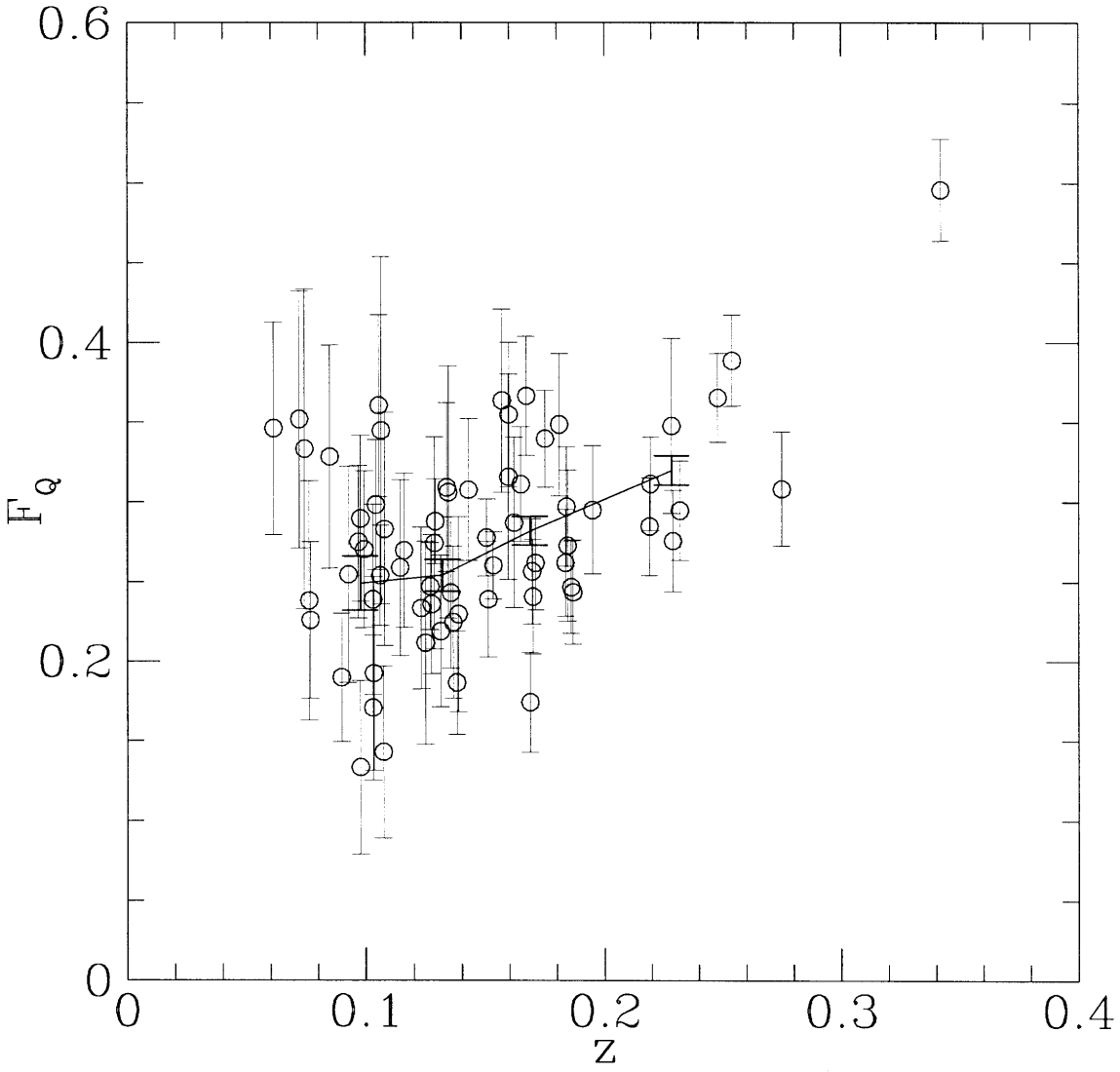

Fig. 23.— Fraction of disk galaxies vs. redshift
Fraction of galaxies with $\log_{10} Q > -1.5$ (disk-like morphologies) in 67 Abell clusters versus redshift. Errors bars are from Poisson statistics. The clusters are averaged into four bins with redshift (heavy error bars connect by the solid line).

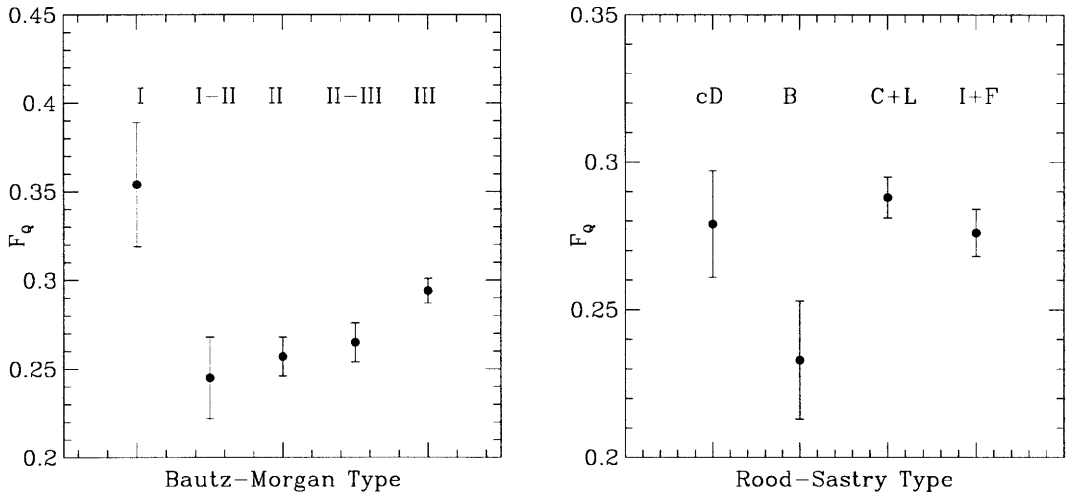

Fig. 24.— Fraction of disk galaxies vs. cluster morphology
Fraction of high Q (disk-like) galaxies versus Bautz-Morgan and Rood-Sastry cluster classifications. The values are the weighted averages of the individual clusters. The trend is from dynamically relaxed, older clusters on the left to unrelaxed, young clusters on the right.

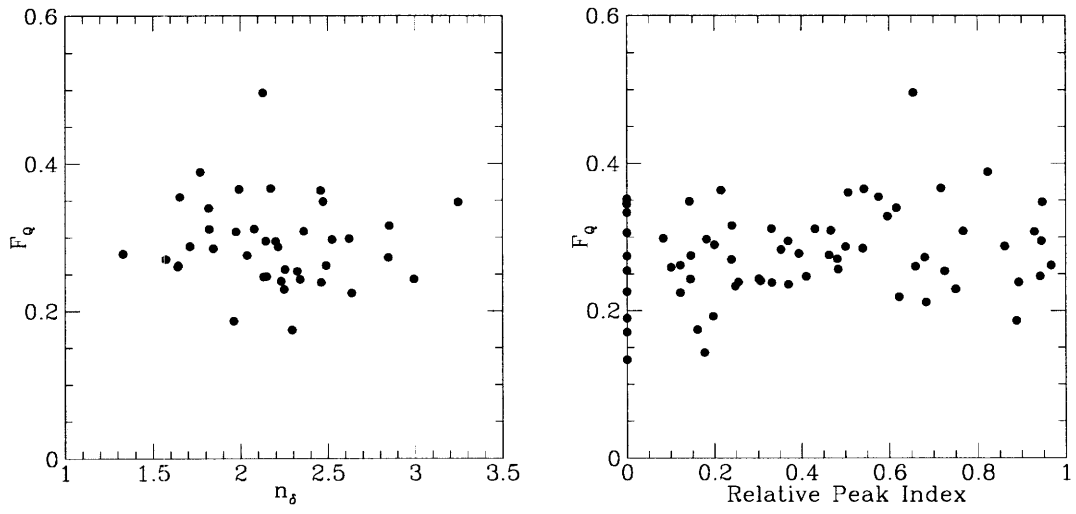

Fig. 25.— Fraction of disk galaxies vs. morphology indices
Fraction of high Q (disk-like) galaxies versus concentration and relative peak indices. Individual error bars have been omitted for clarity; Median errors are shown.

Table 1: Abell Cluster Galaxy Survey

Abell[a]	z	camera	filter	Ω^b	t_{int}	$\mu_R^{0\,c}$	Abell[a]	z	camera	filter	Ω^b	t_{int}	$\mu_R^{0\,c}$
1	0.1249	STIS	R_A	67.1	1800	25.2	1984	0.1231	STIS	R_A	67.1	1200	24.8
7	0.1073	STIS	R_A	67.1	1800	25.5	1990	0.1269	STIS	R_A	268.4	1270	24.8
24	0.1338	STIS	R_A	67.1	1800	25.9	2001	0.1750	STIS	R_A	268.4	1050	24.2
31	0.1596	STIS	R_A	67.1	1800	25.1	2005	0.1275	STIS	R_A	67.1	1200	24.9
41	0.2750	STIS	R_A	67.1	1800	24.9	2021	0.0994	STIS	R_A	268.4	900	24.5
84	0.1939	STIS	R_A	67.1	1800	25.7	*2056	0.0763	Loral	R_s	88.1	600	25.0
96	0.1344	STIS	R_A	67.1	1800	25.4	*2061	0.0768	Loral	R_s	88.1	600	24.7
136	0.1569	STIS	R_A	67.1	1800	25.3	2065	0.0721	STIS	R_A	67.1	1200	24.8
175	0.1569	STIS	R_A	67.1	1800	25.4	2069	0.1160	STIS	R_A	67.1	1200	24.5
403	0.1033	STIS	R_A	67.1	900	24.7	*2083	0.1143	STIS	R_A	67.1	1200	24.6
439	0.1063	STIS	R_A	67.1	1800	24.1	*2084	0.3420	STIS	R_A	67.1	1200	23.0
1235	0.1042	STIS	R_A	268.4	960	24.3	2089	0.0743	STIS	R_A	67.1	1200	24.5
1278	0.1290	STIS	R_A	268.4	900	24.7	2100	0.1533	STIS	R_A	268.4	900	25.1
1495	0.1429	Loral	R_s	88.1	600	24.5	2110	0.0978	STIS	R_A	67.1	1200	25.1
1504	0.1836	Loral	R_s	88.1	600	24.3	2111	0.2290	STIS	R_A	67.1	1200	24.6
1632	0.1620	Loral	R_s	88.1	600	24.4	2142	0.0899	S/L	R_A/R_s	67.1	1800	25.3
1661	0.1950	STIS	R_A	67.1	2100	25.1	2172	0.1387	STIS	R_A	67.1	1200	24.8
1667	0.1648	Loral	R_s	88.1	600	24.4	*2175	0.0978	Loral	R_s	88.1	600	25.1
1674	0.1060	STIS	R_A	268.4	960	24.4	2178	0.1429	Loral	R_s	88.1	600	25.0
1675	0.1840	Loral	R_s	88.1	600	24.4	2183	0.1365	STIS	R_A	67.1	1200	24.8
1679	0.1699	Loral	R_s	88.1	600	24.2	*2192	0.1868	Loral	R_s	88.1	600	24.4
1793	0.0849	Loral	R_s	88.1	600	24.9	*2198	0.1696	Loral	R_s	88.1	600	24.6
1831	0.0613	Loral	R_s	88.1	600	25.0	*2211	0.1355	Loral	R_s	88.1	600	24.7
1878	0.2540	Loral	R_s	88.1	600	24.0	*2213	0.1597	S/L	R_A/R_s	67.1	1500	25.0
1889	0.1860	Loral	R_s	88.1	600	24.4	2218	0.1950	STIS	R_A	67.1	900	24.0
1929	0.2191	Loral	R_s	88.1	600	24.3	2224	0.1504	STIS	R_A	268.4	900	25.0
1930	0.1313	STIS	R_A	67.1	1200	24.6	*2235	0.1511	S/L	R_A/R_s	67.1	1500	24.8
1934	0.2195	STIS	R_A	67.1	1200	24.2	2240	0.1380	STIS	R_A	268.4	900	24.9
1952	0.2480	Loral	R_s	88.1	600	24.1	*2244	0.0970	Loral	R_s	88.1	600	24.8
1954	0.1810	STIS	R_A	67.1	1200	24.3	*2257	0.1054	Loral	R_s	88.1	600	24.8
1958	0.2284	STIS	R_A	67.1	1200	24.2	*2266	0.1671	S/L	R_A/R_s	67.1	1500	25.1
1961	0.2320	STIS	R_A	67.1	1200	24.7	2443	0.1030	STIS	R_A	67.1	1800	25.7
1979	0.1687	STIS	R_A	67.1	1200	24.4	2471	0.1078	STIS	R_A	67.1	1800	25.6
1984	0.1231	STIS	R_A	67.1	1200	24.8							

Note. — (a)*indicates observed under photometric conditions; (b) solid angle imaged in arc-minutes^2; (c) rest-frame surface brightness of 2.5σ detection isophote in magnitudes per arc-second^2.

Table 2: Cluster Morphology Indices

Abell	z	C_A	B.M.	R.S.	δ_L	σ_δ	I_C	I_P	R_P
0001	0.12	51	III	I	2.253	1.160	-0.723	0.264	0.338
0007	0.11	55	II-III	I	2.593	0.790	-0.427	0.793	0.346
0024	0.13	127	III	I	3.501	0.152	-0.002	0.005	0.325
0031	0.16	90	II-III	F	2.702	0.410	-0.602	0.241	0.308
0041	0.28	153	II-III	L	3.272	0.179	-0.339	0.154	0.328
0084	0.10	76	II	L	2.474	0.731	-0.732	0.063	0.318
0096	0.13	61	I-II	I	0.000	-0.608	-3.079	0.538	0.674
0136	0.16	99	I	cD	2.811	0.806	-0.548	0.854	0.305
0175	0.13	84	III	I	3.268	0.343	0.004	0.369	0.243
0403	0.10	100	II-III	cD	2.116	1.646	-1.249	0.476	0.289
0439	0.11	35	N.A.	L	0.000	-0.417	-2.759	0.757	0.259
1235	0.10	122	II	cD	3.395	0.486	-0.085	0.951	0.620
1278	0.13	151	N.A.	F	3.366	0.149	-0.237	0.143	0.639
1495	0.14	39	III	C	3.395	0.178	0.574	0.008	0.347
1504	0.18	98	I-II	B	3.600	0.218	0.247	0.077	0.431
1632	0.16	80	II-III	I	3.629	0.288	0.393	0.372	0.770
1661	0.19	97	III	F	2.291	0.930	-1.056	0.095	0.929
1661	0.19	97	III	F	3.030	0.198	-0.317	0.201	0.559
1667	0.16	98	III	F	3.070	0.203	-0.283	0.074	0.548
1674	0.11	165	II-III	F	2.729	0.370	-0.925	0.231	0.279
1675	0.18	50	II-III	L	3.766	0.238	0.801	0.666	0.206
1677	0.18	112	II-III	C	3.132	0.455	-0.298	0.348	0.726
1679	0.17	115	III	C	2.939	0.302	-0.507	0.452	0.204
1793	0.08	54	III	I	3.185	0.229	0.176	0.274	0.355
1831	0.06	67	III	F	3.851	0.231	0.717	0.757	0.279
1878	0.25	56	III	F	3.385	0.325	0.355	0.242	0.776
1889	0.19	112	III	L	3.534	0.128	0.104	0.164	0.473
1929	0.22	95	II-III	I	3.557	0.257	0.222	0.365	0.546
1930	0.13	60	II	C	3.714	0.251	0.644	0.210	0.488
1934	0.22	142	II	F	3.307	0.161	-0.261	0.544	0.276
1952	0.25	107	III	C	3.242	0.166	-0.162	0.312	0.308
1954	0.18	120	I	cD	3.468	0.365	-0.002	0.866	0.582
1958	0.23	88	III	I	0.000	-0.203	-3.291	0.017	0.600
1961	0.23	137	III	C	3.224	0.323	-0.323	0.006	0.614
1979	0.17	108	II	F	3.123	0.235	-0.286	0.662	0.390
1984	0.12	96	II	B	3.748	0.167	0.407	0.633	0.495

Note. — (a)*indicates observed under photometric conditions; (b) solid angle imaged in arc-minutes^2; (c) rest-frame surface brightness of 2.5σ detection isophote in magnitudes per arc-second^2. isophote.

Table 3: Cluster Morphology Indices (cont.)

Abell	z	C_A	B.M.	R.S.	δ_L	σ_δ	I_C	I_P	R_P
1990	0.13	140	III	L	3.068	0.183	-0.491	0.013	0.252
1990	0.13	140	III	L	3.286	0.205	-0.273	0.236	0.487
2001	0.17	57	II	L	3.253	0.204	0.213	0.211	0.756
2005	0.13	105	III	B	3.562	0.172	0.169	0.374	0.526
2021	0.10	52	III	I	0.000	-2.307	-2.987	0.143	0.426
*2056	0.08	50	II-III	C	2.703	0.548	-0.262	0.185	0.360
*2061	0.08	71	III	L	4.003	0.200	0.836	0.061	0.297
2065	0.07	109	II	C	3.892	0.190	0.477	0.294	0.234
2069	0.12	97	II-III	C	3.952	0.157	0.605	0.652	0.452
*2083	0.11	60	III	cD	3.702	0.307	0.632	0.456	0.251
*2084	0.34	67	III	C	3.764	0.176	0.630	0.230	0.268
2089	0.07	70	II	cD	3.792	0.349	0.633	0.604	0.233
2100	0.15	138	III	C	3.102	0.147	-0.449	0.128	0.519
2110	0.10	54	I-II	cD	2.926	0.491	-0.083	0.465	0.362
2111	0.23	148	II-III	C	2.694	0.274	-0.897	0.266	0.511
2142	0.09	89	II	B	3.446	0.224	0.148	0.631	0.242
2142	0.09	89	II	B	3.472	0.219	0.174	0.024	0.403
2172	0.14	69	II-III	L	0.000	-0.261	-3.151	0.178	0.427
*2175	0.10	61	II	cD	3.967	0.223	0.888	0.668	0.387
2178	0.09	51	II	I	2.551	0.516	-0.425	0.530	0.273
2183	0.14	56	II	C	3.701	0.254	0.671	0.662	0.793
*2192	0.19	62	II-III	F	3.830	0.201	0.741	0.437	0.282
*2198	0.17	85	III	F	2.862	0.187	-0.409	0.322	0.515
*2211	0.14	54	II-III	I	3.082	0.390	0.073	0.432	0.210
*2213	0.16	75	III	I	2.708	0.308	-0.491	0.215	0.423
*2213	0.16	75	III	I	2.906	0.238	-0.293	0.510	0.374
2218	0.17	214	II	C	4.036	0.144	0.232	0.680	0.254
2224	0.15	138	III	C	3.122	0.196	-0.429	0.423	0.716
2235	0.15	73	III	F	2.919	0.330	-0.264	0.199	0.583
*2235	0.15	73	III	F	3.188	0.333	0.005	0.446	0.225
2240	0.14	165	III	I	2.426	0.677	-1.228	0.073	0.572
*2244	0.10	89	I-II	cD	3.488	0.268	0.190	0.818	0.423
*2257	0.11	61	N.A.	C	3.370	0.222	0.291	0.285	0.204
2266	0.17	83	III	C	3.433	0.139	0.176	0.038	0.350
*2266	0.17	83	III	C	3.585	0.120	0.328	0.374	0.344
2443	0.10	117	II	C	2.699	0.374	-0.757	0.654	0.381
2471	0.11	92	III	I	2.456	0.902	-0.861	0.434	0.296

Note. — (a)*indicates observed under photometric conditions; (b) solid angle imaged in arc-minutes^2; (c) rest-frame surface brightness of 2.5σ detection isophote in magnitudes per arc-second^2. isophote.

Table 4: Background Fields

Field	Ω arc-min.^{2a}	Seeing^b	A_B [mag]^c	m_0^d	$\Sigma(17-24)^e$
0421+019	94.05	2.08	0.46	33.60	6.47 ± 0.26
0747+611	92.38	1.46	0.17	32.63	9.61 ± 0.31
0953+549	98.87	1.11	0.00	32.89	9.32 ± 0.31
0957+557	92.38	1.23	0.00	32.82	10.32 ± 0.33
1213-002	102.00	1.19	0.03	32.90	11.09 ± 0.33
1245+345	101.74	1.03	0.02	32.91	11.32 ± 0.33
1329+412	105.27	1.45	0.00	32.95	12.99 ± 0.35
1623+268	98.51	1.50	0.08	32.58	12.21 ± 0.35
0747+710	14.61	1.99	0.14	32.84	9.79 ± 0.82

Note. — (a) the solid angle of the field in square arc-minutes after areas around bright stars and image defects are excised; (b) intensity-weighted radial moment of the image point-spread function; (c) source: NASA Extragalactic Database; (d) photometric magnitude of 1 DN above atmosphere; (e) total surface density of galaxies with $17 < R < 24$.

Table 5: Variation of LF with Redshift & Cluster Properties

Type	$M^* - 5\log h$	α	$M^*(\alpha = 5/4)$
All	-21.13	1.09	-21.47 ± 0.14
$z < 0.163$	-20.85	1.06	-21.24 ± 0.10
$z > 0.163$	-21.20	0.91	-21.94 ± 0.14
$\delta <$	-20.71	1.01	-21.16 ± 0.10
$\delta >$	-21.25	0.90	-22.04 ± 0.16
I/F	-21.04	1.00	-21.55 ± 0.09
C/L	-21.31	0.92	-22.09 ± 0.16
cD	-20.14	0.64	-21.11 ± 0.21
I-II	-21.08	1.05	-21.50 ± 0.11
III	-21.17	1.10	-21.49 ± 0.10
$I_C <$	-21.10	1.10	-21.47 ± 0.09
$I_C >$	-21.16	1.09	-21.51 ± 0.10
$I_P <$	-21.16	0.88	-21.98 ± 0.13
$I_P >$	-21.04	1.07	-21.41 ± 0.12

Chapter 3

Galaxy Clustering: The Cosmic Rosetta Stone?

3.1 Background

Although galaxies are the stuff of the Universe that is directly observable with our telescopes, the past fifty-years has seen a steady accumulation of *indirect* but practically irrefutable evidence that much or most of the mass is in a 'dark' form that neither emits or absorbs much light, and may be non-baryonic altogether. Dark matter exists over a range of mass scales; reviews of the subject include Trimble (1987). The earliest evidence was dynamical in nature: Dark matter on the scale of galaxy clusters was first pointed out by Zwicky (1933) and much later on the scale of galaxies (Freeman 1970; Ostriker *et al.* 1974; Rubin *et al.* 1978) based on the dynamics (velocity dispersions) and kinematics (rotation curves) of galaxies. Evidence for dark matter on very large scales comes from the analysis of the deviation of galaxy motions from a uniform Hubble flow ("peculiar velocities") (Dekel *et al.* 1993). The amount of dark matter is often estimated in terms of the required mass density to close the universe. The dark matter in our Galaxy and other galaxies amounts to $\Omega \sim 0.03$, in clusters is ~ 0.2 and the large-scale peculiar velocity studies indicate $\Omega \sim 0.5$. Theoretical prejudices motivate $\Omega = 1$ to be consistent with a flat universe with no cosmological constant (Guth & Pi 1982). By contrast, the total amount of luminous matter (assuming the mass-to-light ratio of normal stellar populations) contributes $\Omega_L = 0.0035h^{-1}$ (Lin *et al.* 1996) and nucleosynthesis theory combined with standard cosmological models

limits the total baryonic matter to 0.01-0.05 h^{-2} (Trimble 1987).

Galaxies are thus the visible, but perhaps biased, tracers of the underlying and otherwise invisible mass distribution of the Cosmos. One of the goals of modern extragalactic astronomy is to measure the statistics of that distribution and its evolution with redshift. Models of cosmological structure formation make predictions of the evolution of this distribution from a postulated field of random mass density perturbations in an otherwise extremely homogeneous early universe. These models typically consist of three elements: The world-model parameters Ω_0 and Λ_0 (the cosmological constant) at the present epoch; the power spectrum of the initial density perturbations, usually described as a power-law with index n (which is almost always negative); and a thermodynamic description of the dark matter, e.g. dissipationless and "hot" or "cold" depending on the temperature at the epoch when the dark matter particles decoupled from the radiation field.

A detailed review of large-scale structure and its application in testing cosmological models is beyond the scope of this Chapter. However, a fundamental prediction of all models in which structure formation is hierarchical, i.e., more massive objects form later than less massive ones, is that the evolution with redshift is quite sensitive to the value of Ω_0. In "open" models where Ω_0 is significantly less than unity structure formation is terminated at $z \sim \Omega_0^{-1} - 1$ while for $\Omega = 1$ (flat Einstein-de-Sitter model) structure formation continues to the present epoch. The disparity in the predicted evolution is most pronounced for the most massive gravitationally bound objects seen at the present epoch. These correspond to clusters of galaxies with dynamical masses of order $10^{15} M_\odot$.

The different evolutionary histories will manifest themselves in at least two ways: The co-moving number density of clusters (defined in some systematic fashion) will remain relatively constant with redshift in an $\Omega_0 < 1$ universe until $z = \Omega^{-1} - 1$ after which it will exhibit marked negative evolution. In an $\Omega_0 \sim 1$ model the evolution occurs at the present epoch. Second, the relative dynamical ages of clusters will be markedly different in the two cases; the $\Omega_0 < 1$ clusters will be older than clusters in a flat universe, which are essentially still forming. In principle, the morphologies of galaxy clusters could be used to statistically estimate their ages and constrain the value of Ω_0 (Richstone *et al.* 1992). This possibility has been a powerful motivation for much of modern research and survey work on cluster galaxies.

3.2 Galaxy Cluster Surveys

Abell (Abell 1958) developed the first systematic large-area galaxy cluster catalog that, with its Southern hemisphere and supplements (Abell *et al.* 1989), contains 4076 objects identified by eye as areas of high galaxy surface density on photographic plates. The corresponding data in the third dimension (redshift) is sparse; most of the published redshifts of Abell/ACO clusters are in Struble & Rood (1991). Despite this, the catalog has been the workhorse of galaxy cluster research ever since. The morphologies of clusters in the original Abell catalog were characterized by Rood & Sastry (1971), while Bautz & Morgan measured the relative prominence of the brightest galaxies in these objects (Bautz & Morgan 1970).

Zwicky also constructed a cluster catalog from the same photographic data, but in a much less systematic fashion (Zwicky 1958). Several other cluster catalogs, selected by silicon rather than by eye, have subsequently appeared (Shectman 1985; Lumsden *et al.* 1992; Dalton *et al.* 1994), all based on relatively shallow photographic plate data. The catalogs are typically useful in identifying clusters at a statistically meaningful rate to $z{\sim}0.1 - 0.2$. Deep photographic imaging has been to use to construct small and incomplete samples of clusters to $z < 1$ (Gunn *et al.* 1986; Hoessel & Schneider 1985). These deeper catalogs suggest that the comoving number density of galaxy clusters evolves very little to $z \sim 0.5$.

Spectroscopic and CCD imaging surveys of galaxies provide a far superior quality of information, but have been limited to much smaller areas of the sky. However, as the size of these samples have steadily increased there have been reports of significant clustering at redshifts of 1-3 (Le Fevre *et al.* 1994; Giavalisco *et al.* 1994). To develop an intermediate catalog of reasonble depth and size, Postman *et. al.* (1996) completed a CCD survey of 5 square degrees in two optical pass-bands. Although their catalog contains only 107 cluster candidates without redshift information, they find that their data is consistent with a constant co-moving number density of clusters to $z \sim 0.6$ that is ~ 5 times *higher* than the density of rich Abell clusters at the current epoch.

The identification of a cluster as a gravitational bound object can be secured by spectroscopic measurement of the recessional velocities of candidate member galaxies. In the absence of such detailed (and costly) information, the reliablity of a galaxy cluster catalog, and any conclusions drawn from it concerning numbers of clusters and their evolution, depends on the statistical quality of the catalog, and the degree to which the objects iden-

tified in the catalog correspond to physical clusters. These problems can be distilled down to three basic issues:

The **contamination** of the catalog by objects which are spurious enhancements of the projected surface density of galaxies caused by the chance superposition of many smaller overdensities, or the projection of single large but gravitationally unbound overdensities along the line of sight, e.g., the sheets seen in large redshift surveys (De Lapparent *et al.* 1991).

The **completeness** of the catalog, i.e., the ratio of the number of clusters detected to the actually number at a given detection limit. There are any number of mechanisms through which incompleteness could arise: Juxtaposition of clusters with bright stars may prevent an accurate count of the galaxies or their accurate photometry and eliminate such objects from the catalog. A superposition of a cluster with a significant underdense region ("void") along the line of sight will suppress the galaxy counts and may cause the cluster to drop out of the catalog altogether. If the shapes of galaxy clusters depart significantly from spherical symmetry (Plionis *et al.* 1991), projection effects become important. For example, if clusters are actually filametary in form, they will be detected most easily end-on when the projected surface density of galaxies is highest.

The **correspondence** between the projected clustering of galaxies in space and the underlying mass distribution; i.e., do gravitationally bound objects on mass scales of $10^{14} - 10^{15} M_{\odot}$ always have corresponding and proportional enhancements in the galaxy density? The concept of galaxy 'bias' was introduced (Bardeen *et al.* 1986) to explain why galaxies appear to cluster much more strongly on scales of about 8 h^{-1} Mpc than the underlying mass distribution does, as inferred from the galaxy velocity dispersion. If galaxies preferentially form in the densest areas the discrepancy is nicely resolved. In the case of cluster selection, one is not concerned with the relatively small amounts of bias postulated to explain the large-scale observations. If, for some unknown reason, there was a significant amount of *negative* bias for some clusters, e.g. galaxies failed to form or were destroyed in them, then there might be clusters with very high mass-to-light ratios that would fail to appear in optically-selected catalogs. These mythical creatures, so-called "dark clusters", are an intriguing but unsubstantiated idea. A dark cluster might reveal itself through the gravitational lensing of background objects. Dark lenses have been implicated as the culprit of the wide-separation QSO lense candidate 2345+007 (Steidel & Sargent 1990). A more

secure identification of a dark lense might occur through the detection of X-ray emission from a hot intracluster medium in hydrostatic equilibrium with a gravitational potential that contains few or no galaxies (see the next section). Perhaps the best candidate yet found is the "dim" cluster HCG94, identified as a compact group by Hickson *et. al.* (1989), but found by Ebeling *et. al.* (1995) to possess an X-ray luminosity commensurate with a full-fledged cluster of galaxies.

3.3 X-RAY CLUSTERS

3.3.1 X-RAY EMISSION FROM CLUSTERS

X-ray emission from the Coma galaxy cluster ($z = 0.023$) was first confirmed by a sounding rocket flight in 1969 and reported in 1971 (Meekins *et al.* 1971). *Uhuru*, the first X-ray observatory satellite, subsequently detected X-rays from several other clusters and obtained spectra that showed the X-ray spectra to be consistent with free-free (brehmstrahllung) emission from optically thin intracluster medium at temperatures of a few keV (Kellogg 1973). Successive satellite missions have enormously expanded both the number of X-ray clusters and the amount of detailed information about their emission. The increased sensitivity of X-ray instrumentation has enabled the detection of clusters to cosmological distances: Currently, the most distant X-ray cluster lies at $z = 0.81$ (Gioia & Luppino 1994). The Coma cluster has an X-ray luminosity in the 0.5-4.0 keV range of $2.0 \times 10^{44} h^{-2}$ ergs s^{-1}, where h is the Hubble Constant in units of 100 km s^{-1}Mpc^{-1}. The detection limits of the latest imaging satellites like *Einstein* and *Rosat* with modest exposure times is 1×10^{-13} ergs s^{-1} cm^{-2}, and thus for an open ($q_0 = 0$) Robertson-Walker cosmology, a Coma-like cluster could be in principle be detected to a redshift of 2.3.

Observations and some simple physics indicates that; (1) the X-ray emitting gas is in approximate hydrostatic equilibrium with the gravitational well of the cluster; (2) the emission is long-lived and not a transient phenomenon.

Pressure-supported gas in hydrostatic equilibrium with the gravitational potential of a cluster will have a temperature approximated by the virial relation;

$$T \sim \frac{2 m_p \sigma^2}{3 k_B} = 6.6 keV \left(\frac{\sigma}{1000 km/sec} \right), \tag{3.1}$$

where σ is the galaxy velocity dispersion in the potential well of the cluster. The close correspondance between the observed gas temperature and galaxy velocity dispersion supports the hypothesis that the X-ray-emitting gas in most clusters is equilibrated. This phenomenon has been explored to to place significant constraints on models of the depth and shape of the gravitational potential and the mass (much of which is unseen) responsible for it, e.g. (Buote & Canizares 1994; Buote & Tsai 1996).

The X-ray volume emissivity of gas with primordial composition (76% H and 24% He) at temperature $T > 1$ keV is $\epsilon_X = 4.87 \times 10^{-24} n_e n_i T^{1/2}$ ergs sec^{-1}cm^{-3} K$^{-1/2}$ (Lang 1980). The total luminosity of a cluster with gas-mass M_g and electron temperature T_e obeys the scaling,

$$L_X \sim M_g \rho_g T_e^{1/2} \tag{3.2}$$

The density-squared dependence of the emissivity has profound consequences: First, it means that the inner regions of the cluster with the highest gas density will be greatly accentuated, making X-ray clusters appear as distinctive, clearly-defined objects on the sky. Supposing that the space density of gas has the radial profile r^{-2}, the corresponding X-ray surface brightness will fall off as θ^{-3}, much faster than the projected galaxy distribution (θ^{-1}). The corollary of this effect is the small volume filling factor of the X-ray emission ($\sim 10^{-6}$). The probability of chance superpositions becomes vanishingly small and thus samples of X-ray selected clusters do not suffer from the projection effects which hinder optical surveys. On the other hand, the sensitivity to the gas density makes the X-ray emission very dependent on the thermal state of the gas, as I show later.

The approximate cooling time of the X-ray emitting gas is simply the mean thermal energy divided by the luminosity:

$$\tau_c \sim \frac{3kTM}{2L_x m_p} = 8.3\Omega^{-1} \left(\frac{M}{10^{15} M_\odot}\right) \left(\frac{L_x}{L_{Coma}}\right)^{-1} \left(\frac{\Omega_g}{0.03}\right) Gyr \tag{3.3}$$

i.e., of order the Hubble time and much longer than the crossing time ($\sim 10^9$ years). Only in the innermost regions of some clusters is the estimated cooling time shorter than the dynamical time, producing "cooling flow" instabilities (Fabian *et al.* 1991).

Since the emission from X-ray clusters is long-lived, can be detected to high redshift, and is not subject to line-of-sight projection effects, the statistics of these objects are a potentially powerful tool to test models of cosmology and structure formation (Eke

et al. 1996). One is also relying on a phenomenon that is different than the process of galaxy formation and thus may be a means of detecting dark clusters missed by optical observations, i.e., the X-ray emission of a cluster is not directly dependent on the cluster mass-to-light ratio.

The X-ray picture is not all that rosy, however. The very effect which makes X-ray clusters easy to find, i.e., the sensitivity of the luminosity to the gas density, also hinders an interpretation of the observations. Since clusters are detected and selected based on X-ray flux, and thus, at a given redshift, their intrinsic X-ray luminosity, the thermodynamic state of the gas will significantly bias a catalog (I discuss the effects of X-ray surface brightness in the next section). This state may depend on the thermal history of the gas, which is very uncertain. Radiative cooling can be very important in the centers of some clusters at the present epoch where the density and brehmstrahllung emissivity are high (Fabian *et al.* 1991) and this process may have been more important at earlier, times when collapsed objects would have been denser. High rates of star formation and subsequent supernovae during the formation of galactic bulge populations may have injected energy into the intracluster medium at an earlier epoch. Finally, it is not known to what degree the gas is shocked by the merging of dark-matter halos in the hierarchical picture of structure formation. This may depend on the power spectrum of density fluctuations, since the merging of large masses would be expected to produce more shocking of the gas, while the steady of accretion of small masses might produce a more adiabatic evolution.

I illustrate this by presenting a paradox: The simplest model of X-ray cluster evolution includes the hierarchical formation of structure produced by an initial field of Gaussian fluctuations with spectral index n evolving in a universe with critical mass density ($\Omega = 1$). Clumping proceeds to larger and larger mass scales with time, and the gas is continually heated by shocks to achieve hydrostatic equilibrium. The typical mass of a bound object at redshift z scales as;

$$M \sim (1+z)^{-6/(n+3)}. \tag{3.4}$$

The collapse density is proportional to the mean cosmological density at that epoch;

$$\rho \sim (1+z)^3 \tag{3.5}$$

Combining these with the virial equation gives the temperature of the gas;

$$T \sim (1+z)^{(n-1)/(n+3)}. \tag{3.6}$$

Thus the X-ray luminosity of a characteristic bound object is,

$$L_x \sim M\rho T^{1/2} \sim (1+z)^{(7n+5)/(2n+6)}. \tag{3.7}$$

These scalings are supported by the results of high-resolution numerical simulations (Navarro *et al.* 1996). For the Cold Dark Matter model, the spectral index over the relevant range of mass scales is $n = -1$ and therefore $L_x \sim (1+z)^{-1/2}$, decreasing with redshift. However the co-moving number density of such objects would increase rapidly as $M^{-3} \sim (1+z)^3$. Thus the co-moving X-ray emissivity of the universe would *increase* with redshift. In an open universe $\Omega < 1$ the rapid positive evolution would still occur, but not until a redshift $z \sim \Omega^{-1} - 1$.

As has been pointed out by Evrard & Henry (1991) and Kaiser (1991), among others, this is firmly ruled out by the observations, which if anything, suggest *negative* evolution at $z < 0.5$. One explanation is that the spectral index is steeper, e.g., $n = -2$, such that $L_x \sim (1+z)^{-9/2}$. However this does not explain the lack of evolution seen at at optical wavelengths (§3.2). An alternative suggestion (Kaiser 1991) postulates an injection of energy into the intracluster medium at some early time, raising the entropy of the gas to a much higher value. This might have occured during the epoch of galaxy formation at $z > 3$ (Steidel *et al.* 1996). Thereafter, the gas evolved adiabatically. Taking the ratio of specific heats γ to be 5/3, the X-ray luminosity is found to evolve as $L_x \sim (1+z)^{-5}$. There is an unfortunate degeneracy in a *high* sensitivity to both the power spectrum and adiabaticity. Furthermore, the effects of negative evolution in the X-ray gas can be partially offset by the suppression of structure formation in an open universe.

A different approach is to select clusters based on the temperature of the X-ray gas (usually done by fitting models to X-ray spectra). The temperature of the X-ray emission is a direct indication of the depth of the potential well and thus the mass of the cluster. (But this does not eliminate the luminosity and surface-brightness selection effects in the sample.) Also, since the X-ray-emitting gas traces the shape of the cluster potential, the surface brightness morphology, which is independent of the X-ray luminosity, remains an

independent test of cosmology. Several techniques have been applied to measuring the shapes of nearby clusters (Mohr *et al.* 1995; Buote & Tsai 1996). Presumably, clusters at higher redshifts would be younger on average and thus appear more distended or irregular on the sky.

Exploitation of the detailed properties of high-redshift clusters for the purposes of constraining cosmological models must await the next generation of X-ray telescope satellites which combine high sensitivity, spatial resolution and energy resolution, particularly the Advanced X-ray Astronomical Facility (AXAF) (Canizares 1990). In the meantime, it remains to be clearly discerned what the results of current and previous surveys, however imperfect, are telling us.

3.3.2 X-RAY CLUSTER SURVEYS

Once it was confirmed that the X-ray emission from most galaxy clusters is the thermal free-free emission from an optically-thin intracluster medium, the number of detected clusters and our increased understanding of their statistics and evolution with redshift has been limited only by the steady improvements in sensitivity and resolution brought about by advancements in X-ray telescope and detector technology. This has also brought an increased understanding of the inherent systematics of the catalogs which are produced (§3.4).

The large numbers of galaxy clusters detected by the X-ray telescope and the Imaging Proportonal Counter (IPC) on the *Einstein* Observatory satellite made possible the first serious investigations of their statistical properties (Henry *et al.* 1982; Soltan & Henry 1983) (see descripton of *Einstein* and the IPC in §4.1.1). These found that the X-ray luminosity function (XLF) of nearby Abell clusters could be described by a power law over the range $10^{43} - 10^{45}$ ergs sec^{-1}, with more luminous clusters having a lower co-moving number density. The value of the power-law index is close to -2, depending on the details of the fitting process. Soltan & Henry (1983) found that L_x correlated with increasing Abell "richness", a measure of the galaxy density, evidence that the X-ray luminosity was an indication of the global state of a cluster, and not an independent statistical process. Henry *et. al.* (1982) concluded that there was no evidence that the slope of the XLF evolved strongly with redshift to $z \sim 0.5$, although the small size of their sample and incompleteness still allowed for considerable evolution.

Edge *et. al.* (1990), using a larger and more complete X-ray cluster sample con-

structed by Lahav (Lahav *et al.* 1989), found that a Schechter function with characteristic luminosity $L_x^* = 2.0 \pm 1h^{-2} \times 10^{44}$ ergs sec^{-1} ($\sim 1L_{Coma}$) provided a slightly improved fit to the XLF and a slightly flatter slope of $\alpha = -1.65 \pm 0.26$. They also measured the X-ray temperature function (XTF) using measurements from the EXOSAT observatory and obtained a best-fit power-law index of $\alpha = 4.93 \pm 0.37$. Finally, the sample was found to be significantly depleted of $L_x > L_x^*$ clusters at $0.1 < z < 0.2$ compared to the space density of such objects at $z < 0.1$, suggesting a steepening of the XLF with redshift. No attempt was made to constrain any redshift evolution of the XTF.

A significant advancement in the size and quality of X-ray surveys occured with the advent of the Extended Medium Sensitivity Survey (EMSS), which was constructed from sources serendipitously detected in Einstein Imaging Proportional Counter images of high Galactic latitude targets (Gioia *et al.* 1990; Stocke *et al.* 1991). Of the $\sim$ 800 objects, 104 were eventually identified as galaxy clusters (Gioia & Luppino 1994). The most distant cluster in the sample lies at $z = 0.81$. A complete subset of these above a flux limit 1.5×10^{-13} ergs s^{-1} cm^{-2} and a declination $\delta > -40°$ were anlyzed (Henry *et al.* 1992): The clusters were divided into three approximately equally-populated bins with redshift ($0.14 < z < 0.2$, $0.2 < z < 0.3$, and $0.3 < z < 0.6$). The slope of the XLF was found to monotonically steepen with redshift. A power-law fit to each XLF returned indices of -2.09 ± 0.20, 2.63 ± 0.22 and 3.09 ± 0.27 in successively higher redshift bins. This provided strong evidence for negative redshift evolution in the luminosity or number of clusters with $L_x > 0.7 \times 10^{44}$ ergs at $z > 0.2$.

In 1990 the Roentgen Observatory Satellite *Rosat*, was launched. The satellite, still in limited operation at this writing, carries an X-ray telescope with three detectors; two Position Sensitive Proportional Counters (PSPC) and a High Resolution Imager (HRI). The reader is refered to Ebeling (1993) and references therein for a detailed description of the satellite and instruments. The X-ray telescope/PSPC combination offered an effective area 3 times larger than the *Einstein* telescope and IPC, with an on-axis angular resolution of 25", a factor of 3.6 improvement. The circular field of view of the PSPC was 2 degrees in diameter, although the imaging performance of the X-ray telescope deteriorated rapidly further than 20 arc-minutes from the axis. The PSPC was used to conduct a six-month All Sky Survey (RASS) in which $\sim$ 50,000 sources have been detected. Subsequent pointed imaging has covered several percent of the sky and resulted in the detection of another

$\sim 70,000$ sources.

The ROSAT Brightest Cluster Sample (BCS) consists of a flux-limited ($f_x[0.1 - 2.4keV] > 5.5 \times 10^{-12}$ ergs sec^{-1} cm^{-2}) sample of northern ($\delta > 20°$), high Galactic latitude ($|b| > 20°$) galaxy clusters, most of which were identified by their association with previously known (i.e., optically identified) clusters. Ebeling *et. al.* (1996) constructed an XLF from these clusters and fit a Schechter function, finding $L_X^* = 2.2 \pm 0.4h^{-2} \times 10^{44}$ ergs sec^{-1} and $\alpha = -1.78 \pm 0.09$, in agreement with Edge *et. al.* (1990). However, they find that their larger sample is consistent with no evolution in the XLF to $z < 0.3$. It appears that the Edge *et. al.* result was probably the result of a statistical "fluke" de-populating the high-redshift portion of their sample. However, the Ebeling *et. al.* result is not in confict with the evolution found in the EMSS at $z > 0.3$.

In fact, samples of clusters from the deeper RASS field around the North Ecliptic Pole, which extend to lower flux levels and higher redshifts, do appear to show negative X-ray luminosity evolution at $z > 0.3$ (J. P. Henry, private communication). There has been a proliferation of projects to identify galaxy clusters in PSPC pointed images, which have flux limits an order of magnitude deeper than the RASS (Castander *et al.* 1994; Rosati *et al.* 1995). The samples are still small and conclusive results from these efforts are still awaited.

This is to be contrasted with the picture at optical wavelengths of little or no evolution in the co-moving number density of clusters to much higher redshifts. This raises the "correspondence" question; are the objects seen in X-rays the same as those in the optical? At low redshifts there is evidence that this is true. Ebeling (1993) and Ebeling *et. al.* (1993) have constructed catalogs of rich Abell clusters detected in the *Rosat* All Sky Survey and in the process have found that nearly all rich clusters have bright X-ray counterparts to $z \sim 0.15$. There are a number of serendiptiously observed X-ray cluster, particularly nearby clusters, that fail to appear in the optically-selected catalogs. At the moment there is no substantial published evidence that the two populations are significantly different. Tucker (1995) searched for "failed" clusters of galaxies using 17 unidentified sources in *Einstein* IPC images, 10 of which showed significant source extent. Of these ten objects, nine were found to be associated with "significant" clustering on POSS photographic plates and a ninth was identified as a star. [This author independently obtained CCD imaging of the remaining object which showed it to be a distant rich galaxy cluster.] They concluded that

failed galaxy clusters do not consistute a significant fraction of the over-all cluster total.

Thus the disparity between the X-ray- and optically-selected samples is either a real affect, or a redshift-dependent systematic of one (or both) of the catalogs. The pitfalls of optically-selected cluster samples were discussed above; I next discuss the problems associated with the X-ray surveys.

3.4 Limitations of X-ray Surveys

Our view of the X-ray evolution of clusters is affected by the biases and selection effects inherent in surveys. One such bias is the energy range of the X-ray detection, which will bias the results towards clusters with characteristic temperatures hotter than the energy range. The effect is small for the Einstein IPC and ROSAT PSPC telescope/detector combinations with significant sensitivity in the 0.5-4 and 0.2-2 keV ranges, respectively. A more significant bias which I address here is the surface brightness of the X-ray emission. Clusters with a given total flux which are resolved by imaging detectors can be more difficult to detect. The improvement in X-ray optics has brought a succession of telescopes with better angular resolution: However this skews detection towards sources which appear equally more compact on the sky. If clusters evolve rapidly with redshift, then surface brightness selection effects may be important in X-ray surveys. A sample of X-ray samples will also be biased by the particular machinery used to detect the objects in X-ray images. Traditional X-ray source detection techniques have employed a '"sliding box" or window of fixed size which is moved over the image to find locations of significant excess count rate with respect to the background. The detection process will be biased towards those objects with surface brightness profiles similar to that for which the detection window geometry was optimized, e.g., point sources. The production of the EMSS catalog employed such a point-source detection algorithm and as a consequence, the sample of galaxy clusters in the EMSS is biased towards clusters with a high central surface brightness. More extended sources with integrated fluxes above the survey threshold levels may have been excluded due to their lack of concentrated emission. Henry *et. al.* (1992) used isothermal β models with β, the ratio of gas temperature to velocity disperions equal to two-thirds, and found that between 50% and 93% of the cluster emission falls outside the 2.4' $\times$ 2.4' detection cell of the EMSS survey.

Many clusters exhibit a centrally peak X-ray surface brightness distribution which has been linked to the development of a "cooling flow", a process where the gas in the dense inner core of a cluster attains a cooling time shorter than its dynamical time and continuously cools as it moves towards the bottom of the potential well (Fabian *et al.* 1991). The peak in the surface brightness may contribute only a small fraction ($\sim$ 10%) of the total flux from the cluster, but may increase the central surface brightness by an order of magnitude. Pesce *et. al.* (1990) have analyzed this effect and determined that 80% of the Lahav *et. al.* (1989) sample of 53 bright X-ray clusters contain cooling flows. They extrapolate this to the Medium Sensity Survey (MSS) clusters and, noting that the MSS detection was tuned to objects with peaked surface brightness profiles, conclude that the MSS sample is reduced by a factor of *four* if the estimated contributions by the cooling flows are removed.

Samples of very bright, nearby clusters which are constructed in a manner that is not biased with surface brightness would be at the very least instructive about what one might find in fainter, more distant samples. The *Rosat* Brightest Cluster Sample (BCS) consists of 172 clusters with $f_x > 5.5 \times 10^{-12}$ ergs sec^{-1} cm^{-2} [0.1-2.4 keV] and $|b| > 20°$ detected in the *Rosat* All Sky Survey (Ebeling *et al.* 1996). The original sample of 164 X-ray clusters were detected at the locations of known clusters using the Standard analysis Software System (SASS), (Voges 1992). However, when the fluxes of these clusters were calculated using the V_TP algorithm (Ebeling 1993) in 2×2 degree-fields, an additional 8 clusters were serendipitously discovered. [Ebehling (1994) developed the Veroni Tesselation Program (V_TP) to detect low surface brightness objects of arbitrary shape in ROSAT PSPC images and has used this to great effect in the X-ray photometry of galaxy clusters. V_TP computes a local density around each detected X-ray photon and links photons in high density areas together to construct objects.] Multiplying by the ratio of the relative areas covered ($\sim$ 6.3), this number suggests there would be a total of about 50 serendiptious clusters in the survey.

A correction to this estimate must be made to account for the correlation of clusters of galaxies as projected on the sky; The number of serendipitous detections near other clusters will be somewhat higher than in random fields. The spatial correlation function of the BCS is

$$\xi(\theta) \sim \left(\frac{r}{13.7 h^{-1} Mpc} \right)^{-1.8}. \tag{3.8}$$

(Bahcall & Cen 1994). The depth of the survey, i.e., the median cluster distance, is approximately 210 h^{-1} Mpc; The survey is extemely dilute due to its large depth. The angular correlation function is then approximately (Peebles 1993),

$$w(\theta) \sim \left(\frac{13.7}{210}\right)^{1.8} \theta^{1-1.8} \tag{3.9}$$

where θ is in radians. Thus w reaches unity at a θ of only 7.4 arc-minutes. I integrate over a circular field with a 4 square degree area to find an excess probablity of 28% of finding an X-ray cluster in a field centered on another X-ray cluster with respect to random fields. Based on this, the expected number of X-ray clusters missed by the SASS anaysis would be ~ 39, or 24%. However, the 95% confidence limits on this incompleteness are 11% and 32%.

The archiving of X-ray imaging data from recent and current telescope missions and the exponentiation of computational power has permitted more careful analyses and re-analyses that are able to detect X-ray objects in a manner less biased with surface brightness. Besides Ebeling's VTP algorithm, Rosati *et. al.* (1995) have used wavelet analysis to search for extended objects as cluster candidates in deep pointed ROSAT PSPC images. In the next Chapter I describe a flux-limited catalog of objects constructed from the entire collection of Einstein IPC images. While the Einstein IPC has been superseded by the ROSAT PSPC in sensitivity and angular resolution, the systematics of the former have been better characterized and direct comparisons can be made to previous catalogs such as the EMSS with no need to correct for changes in the energy range of detection. The detection machinery used to find objects is less biased in surface brightness and thus the catalog can generate a more complete survey of galaxy clusters. In addition, the new catalog retains some surface brightness profile information about each object. Information like this may be useful in quantifying the morphologies of X-ray clusters.

Chapter 4

An Archival EINSTEIN IPC X-ray Cluster Survey

The archiving of the entire *Einstein* IPC database, and the improved understanding of the telescope and detector systematics has led to re-analyses of the data aimed at pushing the limits of source detection. Hamilton & Helfand (1993) performed a fluctuation analysis of several IPC deep fields to constrain the number counts of sources immediately below the detection limit of the images. Moran *et. al.* (1996) have pushed this much further, constructing a catalog of nearly 5×10^4 2σ source candidates in 2520 high Galactic latitude fields.

Here I describe sources detected in *Einstein* IPC images in much the same fashion, except that the objective is to construct a catalog that is optimized for the detection of X-ray clusters in that it is much less biased with surface brightness than previous IPC source catalogs. An improved characterization of the XRT/detector response reduces sysematic errors and permits the significance of sources to be assessed over larger solid angles. Thus sources of a given flux but greater angular extent and lower surface brightness are less likely to be rejected. In §4.1 I describe the construction of the catalog, source identifications, and follow-up observations in §4.2. I then make several cuts of the catalog in an effort to identify promising galaxy cluster candidates (§4.3).

4.1 The Source Catalog

4.1.1 *Einstein* IPC

The Imaging Proportional Counter (IPC) was one of the primary instruments on the High Energy Astrophysical Observatory (HEAO)-2 *Einstein* satellite which operated for two and a half years from November 1978. The IPC was a gas scintillation imaging detector and the X-ray telescope/detector combination was sensitive to photons in the energy range 0.5 to 4.0 keV with an effective area of about 100 cm^2. The field of view was 76 arc-minutes on a side with an on-axis resolution of 1.5 arc-minutes. During its operation, the IPC obtained nearly 4100 images with exposure times ranging from 100-56,000 seconds. The celestial coordinates of every photon detected in IPC images are recorded in optical disk archives at the Columbia University Center for Astrophysics.

4.1.2 Source Detection

The raw source catalog was provided by D. Helfand and B. Oppenheimer (Columbia University). The source detection algorithm was based on previous work (Hamilton *et al.* 1991) for analysis of IPC Deep Survey fields. Details of the algorithm and its application to the construction of a 2σ source candidate catalog is described in Moran *et. al.* (1996). Briefly, a cumulative event list and a corresponding exposure map was constructed for each spacecraft orbit using all IPC events from the unobstructed 38 $\times$ 38 arc-minute center field of view, with additional restrictions on the energy channels used and the allowable telescope-Sun angle during the observations. Individual flat fields are constructed for each orbit and account for energy-dependent vignetting and spatial variations in the detector response. The computed count rates for all orbits are then summed into cumulative count and count-rate maps.

The maps are binned into 32 or 64 arc-second square pixels and scanned with a series of four circular apertures with different diameters: 2.5, 4.7, 8.4, and 12.2 arc-minutes. The smallest aperture is the optimal size for the detection of point sources and the largest aperture is limited by considerations of the field of view. The background was estimated in a circular annullus surrounding each aperture; the width of each annulus is proportional to the diameter of the aperture to maintain a constant ratio (about 14.5:1) of background

area to detection area. The background contribution in the aperture is calculated as the background level multiplied by the ratio of areas and the noise was estimated by adding the Poisson noise from the counts in the aperture and the expected background contribution in quadrature. A detection and its location were recorded if the counts in an aperture exceeded the background by the noise multiplied by a threshhold factor, and if there was an acceptable percentage of reliable pixels in the aperture and background (roughly 60% and 30%, respectively). Detection proceeds iteratively over the entire sky map, with the threshhold decreasing from an intially high value. Pixels associated with sources at each iteration were masked out in successive iterations. The entire map was analyzed separatedly with each aperture (using 32 arc-second pixels for the smaller two apertures and 64 arc-second pixels for the larger two).

An initial pass was made through the IPC sky map using a 2.5σ detection criterion. This threshhold is set deliberately lower than the final detection criterion so that more count-rate information is available for the different apertures when sources are finally generated. 2.5σ was considered the lowest threshhold practical since still lower levels generate too many spurious detections for the catalog to be generated in a reasonable time (24 hours). A catalog of *sources* was constructed from the four separate lists of detections, by matching them if the center of one detection fell within the aperture of another. Each source then consisted of the multiple detections. If more than one detection in the same aperture was matched, the detection with the lower signal-to-noise was discarded. The final detection criteria were established by examining the *detector* coordinates of all sources and raising the threshhold for detection until locations of high frequency of spurious detection (e.g., near the IPC window support ribs) were eliminated. The final significance threshholds are 3σ, 4σ, 4.5σ, and 5σ in the 2.5, 4.7, 8.4, and 12.2 arc-minute apertures. The signal-to-noise must exceed this criterion in at least one aperture for there to be a detection. The increasing threhhold with aperture size reflects the need to account for larger systematic errors.

If the error in the location of a detection is dominated by Poisson noise, then it is proportional to $\sim R/\sigma$, where R is the aperture radius and σ is the signal-to-noise. The location of each source was defined to be the centroid computed as the weighted average of all the aperture centers $\vec{x_i}$;

$$\vec{X_c} = \frac{\Sigma_i \vec{x_i} (R_i/\sigma_i)^{-2}}{\Sigma_i (R_i/\sigma_i)^{-2}} \tag{4.1}$$

A total of 7419 sources were identified in this manner. To serve the purposes of this project, only sources with Galactic latitude $|b| > 15°$ were retained. Also, many nearby extragalactic objects have diffuse X-ray emission and produce spurious detections that could be identified as extended sources. Any sources within 5° of the Large Magellenic Cloud, 2.67° of the Small Magellenic Cloud, 2.67° of the Coma Cluster, or 1.6° of Messier 31 were excluded. The final IPC source list contains 6610 sources. Fig. 1 is a log N-log S (cumulative number versus limiting count rate), where the count rates are those from the 8.4 arc-minute aperture. The number counts of an idealized survey of homogeneously distributed, non-evolving sources to a uniform depth has a number-count slope of -3/2. The departure of the IPC source counts from this behavior is mostly due to the non-uniform survey depth, with the solid angle of sky imaged decreasing with count-rate limit.

4.1.3 Source Identification

The IPC source list was correlated with catalogs of known or prospective X-ray sources to identify known sources such as X-ray emitting stars and Active Galactic Nuclei (AGN), as well as previously known X-ray clusters. These are the **Einstein Online Catalog (EINLINE)**, a compilation of catalogs of identified X-ray sources detected by the *Einstein* Observatory; the **NASA Extragalactic Database (NED)**, an on-line database of extragalactic objects maintained at the Infrared Processing and Analysis Center (IPAC) ; and **SIMBAD** an on-line catalog of both Galactic and extragalactic objects maintained at the Centre des Donnees de Strasbourg (CDS).

In the case of prospective point sources, the matching criterion were established by the two-point angular correlation function for the X-ray source-candidate pairs alone. Fig. 2 plots the relative offsets between the X-ray source and the nearest EINLINE point-source match (star, AGN). There is the expected concentration of matches around the origin whose shape describes the distribution of random and systematic errors in the source position. The concentration has a circularly symmetric component plus a 'tail' of significant matches extending over 2 arc-minutes from the origin. This tail may arise from a systematic error in IPC positions, or from a pecularity in the point response function of the X-ray telescope/IPC combination. To include these matches, the area within a match is described by a circle of 1.5 arc-minute radius and an abutting square 2 arc-minutes on a side.

A source is considered 'identified' if the match is with an object that is a plausi-

ble X-ray source and unrelated to an X-ray cluster. For example, AGN, very bright stars ($m_V < 8$), emission-line or variable stars, and nearby galaxies fall into this category. Unidentified radio sources, *IRAS* (Infrared Astronomical Satellite) sources, and distant galaxies (e.g., Zwicky galaxies) could be associated with galaxy clusters and thus are retained as candidates.

The X-ray sources were correlated with the Abell (Abell 1958; Abell *et al.* 1989) and Zwicky (1958) catalogs of optically identified galaxy clusters. Determining matching criterion for optically identified clusters is more problematic, since the optical centers of these objects were determined from the centroids of the galaxy distribution on large scales (often in a subjective manner), and these may be significantly offset from the centroid of any X-ray emission. In addition, there may be multiple X-ray detections within the cluster. Fig 2(b) is a plot of the offsets between the IPC sources and Abell clusters with contour plots overlaid. There is a central concentration within 8 arc-minutes of the Abell coordinates and an extended "halo" of matches extending to about 18 arc-minutes. Some of these may be produced by multiple detections, bimodal clusters, or by the strong cluster-cluster correlation function. If one relaxes the offset criterion for matching to include these there is the danger of incurring large numbers of spurious sources as the number density of IPC sources on the sky is roughly 2 per square degree. Thus I adopt a maximum offset of 8 arc-minutes (heavy line in the figure) for Abell and Zwicky clusters.

4.1.4 Source Extent Test

The unidentified IPC sources are doubtlessly dominated by objects other than X-ray clusters, e.g. AGN and stars. In the absence of detailed X-ray spectra that can discriminate between the soft- and power-law- spectra of these objects and the ~ 6 keV thermal emission of clusters, the spatial extent of the source can be used to find promising cluster candidates. X-ray cluster exhibit a wide range of surface-brightness morphologies, but a standard model of X-ray clusters (Cavaliere & Fusco-Femiano 1976) is one where the mass distribution of the cluster is described by an isothermal sphere ($\rho \sim r^{-2}$) and the gas is in hydrostatic equilibrium with the gravitational potential. The X-ray surface brightness is then

$$\Sigma_x = \Sigma_0 \left[1 + \left(\frac{r}{r_0}\right)^2\right]^{-3\beta+1/2} \tag{4.2}$$

where the β is the ratio of the specific energy in the galaxies in the potential to that of the gas and has a canonical value of 2/3. The core radii r_0 of nearby clusters is found to range upwards from a minimum of $50h^{-1}$ kpc, with a typical value of $100h^{-1}$ kpc (Jones & Forman 1984). This subtends $\sim$ 45',' one-half of the FWHM of the *Einstein* IPC, at $z = 0.15$. Thus one might hope to discriminate between point sources and clusters to approximately this redshift.

In this catalog, the information on the spatial extent of the sources is in the form of the relative amount of flux in the four apertures. I use this information in a statistical test that returns the probabiity that a source is extended. However, three cautionary notes are in order: First, the catalog is dominated by low signal-to-noise objects for which it may be difficult to robustly separate point-like and extended objects. Second, the width of the XRT/IPC point response function is energy dependent and decreases with higher photon energy. Thus point sources with 'softer' spectra and lower-energy emission will have a more extended appearence in IPC images. Finally, any catalog of X-ray cluster candidates selected on image extent will systematically *exclude* high redshift clusters with concentrated emission since these will have remained unresolved by the IPC.

Following Helfand & Oppenheimer (private communication), source extent is evaluated by comparing the *signal-to-noise* values between apertures rather than the count-rates. For reasons that are still not clear, the distribution of point sources with signal-to-noise $R_{ij} = \sigma_i/\sigma_j$ ratio is more sharply defined than the count-rate ratio for known point-like objects. This is demonstrated in Fig. 3 and Fig. 4 where the count-rate ratio and signal-to-noise ratio distributions are shown for known point sources (stars and QSOs) with $\sigma > 10$ in the 2.5 arc-minute aperture and measurements in the three other apertures. Note there are only three independent choices among the six possible ratios, however six separate criteria are necessary since not all aperture information is available for each source. The extent criteria are established by selecting by eye the three ratios which exhibited the most marked cut-offs in the point-source distribution and calculating the other ratios from these. The former criteria are $R_{21} > 1.20$, $R_{32} > 1.14$, and $R_{43} > 1.03$; the latter are $R_{31} > 1.37$, $R_{41} > 1.41$, and $R_{42} > 1.17$. For comparison, the ratios of sources identified with Abell clusters are shown in Fig. 5. A large fraction (but not all!) of these sources satisfy one or more of the extendedness criteria. In the limit of perfect measurement, a source which satisfies any of these criteria is considered anomolously extended at the corresponding angular

scale. These criteria are optimized to eliminate as many point sources as possible, rather than to detect as many X-ray clusters as possible. There are simply far too many sources to examine many more than the most promising candidates.

In the presence of finite noise, the confidence with which a source may be considered extended depends on the significance with which the criteria are satisfied, i.e., how far an R_{ij} exceeds the threshhold value in terms of the error in R_{ij}. It is desirable to assign a quantitative estimate of this confidence to each source, allowing one to make cuts in the catalog depending on one's particular objective or degree of ambition in performing follow-up observations. Performing this task analytically is extremely difficult since one has to account for systematic detection biases (e.g., Malmquist bias) that become important near the detection limit of the catalog. Instead, I have elected to use Monte Carlo technique to test the significance of source extent. Each of the sources is simulated 10000 times, taking the measured count rates to be the "true" count rates and adding random noise. Each simulated source is passed through the detection criterion and rejected if it fails. The extended source criterion constructed using the high signal point sources are then applied to the "detected" sources. The ratio of the number of simulated sources which pass the extendedness criterion to the total number which are "detected" is an indication of how significant the source extension is.

In addition to choosing the values of the ratios in signal-to-noise for the extendedness criteria, one must also set the number of aperture pairs for which the criteria must be satified. The Monte Carlo results were used as a guide for setting this requirement. I found by experimentation that requiring only one signal-to-noise ratio be significantly large did not sufficiently discriminate against known point sources. Too few sources met the extendedness criterion for all three independent ratios (many sources are missing a measurement in an aperture due to an insufficient number of good pixels). Requiring that two ratios be extended appears to be a happy medium.

Most of the sources are near the detection limit of the Einstein IPC where the noise will be dominated by the particle background. If this is well characterized, the fractional error in the ratio of signal-to-noise between two apertures is equal to the fractional error in the ratio of count rates:

$$\frac{\sigma_{R_{ij}}}{R_{ij}} = \frac{\sigma_{(C_i/C_j)}}{C_i/C_j} \tag{4.3}$$

The count-rate measurements in each aperture are not independent since, in assembling the individual detections to construct sources, only heavily overlapping apertures are matched. In assessing the statistic significance of a ratio of count-rates this dependence must be taken into account and the count-rate ratio must be calculated in terms of independent quantities.

From a list of count rates and positions for each aperture it is not possible to reconstruct the true statistics. Here I use a simple model of a source to approximately account for this effect. I asssume that the apertures are perfectly concentric, such that the independent measurements are the difference in count-rates between successive apertures, i.e., the count-rates in concentric annuli. The relations between the aperture count-rates C_i and annuli count rates c_{ij} are:

$$C_i = C_1 + \Sigma_{j=1}^{i-1} c_{ij} \tag{4.4}$$

The associated variances in each quantity are:

$$\sigma_{C_i}^2 = \sigma_{C_1}^2 + \Sigma_{j=1}^{i-1} \sigma_{c_{ij}} \tag{4.5}$$

$$\frac{C_2}{C_1} = \frac{C_1 + c_{12}}{C_1} \tag{4.6}$$

With some math, one can show that:

$$\frac{\sigma_{R_{ij}}^2}{R_{ij}^2} = S_i^2 + S_j^{-2} \left(1 - 2\frac{C_j}{C_i}\right), \tag{4.7}$$

where S_i is the signal-to-noise in the ith aperture. Thus the variance in R_{ij} is *smaller* than the independent measurement case, as expected, but approaches the latter for $C_i \gg C_j$.

Gaussian-distributed errors are used in the Monte Carlo simulations. Each simulated source is checked for detection as well as spatial extent. I calculate two probability estimators, one for detection and the second for extent;

$$P_D = N_D / N_{MC} \tag{4.8}$$

$$P_E = N_E / N_D \tag{4.9}$$

where N_{MC} is the total number of Monte Carlo simulations, N_D is the number of detected

simulations, and N_E is the number of detected simulations that appear extended. P_D and P_E give the probability that a source with those particular statistics would be detected, and the probability that, if detected it would appear extended.

The cumulative distribution of all objects with P_E, the probability of extent, is shown in Fig. 6. Stars and AGN identified in the EINLINE catalog are plotted separately to calibrate P_E. There is a nearly linear correspondence between the threshhold P_E and the number of stars and AGN below that value, validating our error models and Monte Carlo simulations. 98.5% of stars and AGN have $P_E < 0.99$. As a population, AGN appear slightly *more* extended then stars; a result opposite to the effect expected from the energy dependence of the XRT/IPC resolution. The cumulative distribution does show, however that the tail of the P_E distribution for stars is more pronounced than for AGN.

Of particular importance in understanding the statistics and limitations of the extendedness test are identifying the tail of the tail of the point-source distribution, i.e., those known point sources which meet a conservative extendedness criteria. There are seven sources in the IPC catalog with $P_E > 0.99$ but which lie within 2 arc-minutes of X-ray sources listed in the EINLINE catalog (Table 1). This is 1.5% of the 476 EINLINE stars and AGN in the IPC catalog. One object is a white dwarf and two others are main sequence stars; their high P_E can be understood in terms of their very soft spectra: At low energies the point-response function of the X-ray telescope/IPC combination is broader and sources can appear extended. Oddly, this does not appear to be the case with the majority of stars, as I have shown. An unidentified UV-excess object may also have a soft spectrum in X-rays. The AGN mistaken for extended sources require a different explanation. Two of the three have relatively low S/N in their 2.5 arc-minute apertures and may simply be statistical flukes. Other possibilities include the scattering of X-rays from dust in the interstellar medium to produce an X-ray "halo" (Predehl & Klose 1996), or systematic errors in sources near the edges of the IPC window.

Finally, it is important to bear in mind that by selecting with P_E one is biasing the sample toward sources with signal-to-noise sufficient to discriminate between the point-like and non-point-like possibilities, and thus in favor of brighter objects.

4.1.5 The EMSS Survey Revisited

The EMSS catalog was also generated from a survey of X-ray sources in high Galactic-latitude *Einstein* IPC images (Gioia *et al.* 1990), and is nearly completely optically identified (Stocke *et al.* 1991). Of particular importance are the 104 galaxy clusters it contains, 99 of which have spectroscopic redshifts (Gioia & Luppino 1994). Thus it behooves me to correlate and compare the IPC sources catalog constructed here with the EMSS.

I matched the IPC source catalog with the EMSS catalog maintained online at the Centre de Donnees de Strasbourg (CDS). Of the 835 sources in the EMSS, 576 have an IPC source within 2 arc-minutes, and 76 of the 104 EMSS clusters have counterparts. The fraction of all EMSS sources not appearing in the IPC source list here versus signal-to-noise is shown in Fig. 6. This fraction is not a strong function of signal-to-noise. Rather, the missing sources are probably lost due to the restriction of this survey to the inner 38×38 arc. min. field of view of the IPC. The EMSS used the entire field of view minus a central 10 arc-minute diameter aperture centered on the target, and the area shadowed by the support ribs. The EMSS area per field was 0.6 deg^2 as compared to opposed to 0.4 deg^2 here. The missing field is is consistent with the fraction of missing sources found here (29%), although the latter is somewhat lower due to the decreased sensitivity in the excluded regions of the IPC.

Fig. 7 compares the corrected count-rates in the EMSS with the 2.5 arc-minute aperture rates; the agreement is very good and the scatter is within the errors (only a typical pair of error-bars is shown for clarity). The few outlying points, particularly the clusters, arise from multiple detections within extended sources. The advantage of detecting objects using the larger apertures, particularly for X-ray clusters, is shown in Fig. 7(b), where the *maximum* signal-to-noise among the four apertures is compared to the EMSS signal-to-noise.

Plotting the probability of extent P_E values of the re-detected EMSS clusters versus their redshifts proves telling (Fig. 8). Only 16% of the cluster have $P_E > 0.99$ and all are at $z < 0.25$. Only 26% of the clusters are found extended at two sigma confidence ($P_E > 0.954$) and still only 43% at one sigma confidence ($P_E > 0.683$). Only one cluster at $z > 0.3$ is extended at a the 2σ level. These results are consistent with the early estimate based on a X-ray cluster core radius of $100h^{-1}$ kpc. They also indicate that samples selected with P_E should not expect to see objects similar to EMSS clusters beyond $z \sim 0.3$.

4.2 Optical Counterparts

4.2.1 Digitize Sky Survey Imaging

Preliminary searches for galaxy cluster counterparts to some of the *Einstein* IPC sources were performed using Digitized Sky Survey (DSS) images. The DSS was created by the Space Telscope Science Institute by digitizing Schmidt photographic plates using a microdensitometer and compressing the data by a factor of about 10:1 for distribution on CD-ROMs. The Northern hemisphere plates are Palomar Observatory Sky Survey (POSS) 103a-E (red) 2400-4200 second exposures plates obtained during from 1951 to 1955. The Southern hemisphere plates are SERC J Southern Sky Survey plates with exposures of 1800-7200 seconds. The limiting magnitudes are (very) approximately $R \sim 20$ and $B_J \sim 21$. While the red colors of galaxies, particularly the early-type galaxies in clusters, favor their detection in the E plates, the J plates are of signficantly better quality.

Fifteen by fifteen arc-minute square DSS images of Abell clusters with richness class 2 at various redshifts are shown in Figs. 9 and 10. (Unfortunately some of the detail in the images is inevitably lost in the compression and manuscript reproduction). While, all details about the galaxies are lost at redshifts greater than 0.1, the clusters can still be seen as a concentration of low surface-brightness features to $z = 0.3$ in both the E and J plates, and thus it would appear that one can find any rich cluster counterparts to these sources at least to this redshift.

4.2.2 CCD Imaging of Galaxy Cluster Counterparts

Optical observations remain the touchstone for the confirmation and characterization of X-ray clusters. These observations consist both of spectroscopy to verify that there is a significant excess of galaxies exist within a narrow range of recessional velocities ($\sigma \sim 1000$ km sec^{-1}) and imaging with Charge-Coupled Devices (CCDs) or infrared arrays to measure the numbers, color, and, resolution permitting, morphologies of the cluster galaxies. An observing program to obtain CCD imaging of selected unidentified, high-galactic latitude X-ray sources discovered in Einstein IPC images was begun in 1994 using the 1.3 meter McGraw-Hill telescope at the Michigan-Dartmouth-MIT Observatory and the 60-inch Meyer Telescope at the Palomar Observatories of the California Institute of Technology. The

sources are selected based on their relatively high significance of detection and favorable location on the sky, and not necessarily on their extendedness. The primary objective of the project is to confirm that a significant spatial concentration of galaxies exists at the location of the X-ray emission.

A secondary goal is to obtain photometry of likely cluster members in two or more pass-bands and establish their apparent magnitudes and colors. Accumulating evidence describes the majority of clusters galaxies in terms of two distinctive populations. The first is a population of early-type galaxies that have undergone little change other than than the passive evolution of the old, evolved giant stars which produce most of their luminosity and appear to have originated in a single episode of star formation at large redshift . The objects in a particular cluster exhibit a remarkable degree of uniformity in color, indicating that they are coeval (Stanford *et al.* 1995). Furthermore, there seems to be little or no variation from cluster to cluster. In a color-magnitude diagram the early-type galaxies in a cluster (essentially all at the same distance from the observer) lie along a straight line called the "C-M relationship", with fainter galaxies being slightly bluer. The slope is thought to arise from a variation of metallicity with luminosity. This relationship defines an edge or "red envelope" (O'Connell 1987) the red side of which is devoid of cluster galaxies. The apparent passive evolution of the elliptical galaxies means that the secular evolution of the observer-frame colors with redshift is dominated by K-corrections arising from the redshifted galaxy spectra. In principle, the colors of these galaxies can be used to make photometric estimates of the redshift of the cluster (Molinari *et al.* 1990; Molinari *et al.* 1994).

The second population is composed of blue galaxies with spectra indicating recent or ongoing star formation and disk-like morphologies ((Butcher & Oemler 1984; Dressler & Gunn 1992; Dressler *et al.* 1994). These objects have roughly disappeared in clusters at the present epoch, but show a steadily increasing presence in clusters at $z > 0.2$, called the "Butcher-Oemler effect".

Intermediate-band Gunn-Thuan filters were selected for this work since a considerable amount of distant galaxy photometry has been done using the Gunn-Thuan photometry system, e.g., (Hoessel & Schneider 1985; Molinari *et al.* 1990). Transmission plots of *gri* filters obtained from the Kitt Peak online filter database (http://www.noao.edu/kpno/filters/filters.html) are shown in Fig. 11(a). Colors generated in this photometry system are useful for separating ellliptical and spiral galaxies. Fig. 11(b) is a plot of the predicted $g - r$ color of a

passively evolving elliptical galaxy versus redshift taken from Buzzoni (1989). The different curves respresent different ages of the galaxies at the epoch in which they are observed. Essentially, the observed colors become redder as the large Balmer break from the evolved stars moves to longer wavelengths. Initially, Gunn-Thuan g and r filters were used; an i filter has been added to avoid the potential $g - r$ degeneracy with redshift in the range $0.4 < z < 0.6$.

Two observing runs were conducted at MDM in February 1994 and April 1995, and one run took place at Palomar in December, 1995. The February 1994 imaging was taken under photometric conditions and I present some results from those observations here. A Tektronix 2048^2 CCD with 21 μm pixels was used in 2×2 binning mode for a final scale of 0.635" per pixel. The seeing ranged from 1.3 to over 2 arc-seconds. Exposures were 600 seconds through g and 900 seconds though r.

The images were processed with IRAF (Image Reduction and Analysis Facility) routines. The images were bias-subtracted using the overscan region and trimmed. Dark sky flats for each night were constructed by combining all of the images taken in a particular filter on that night, removing objects and saturated pixels by excluding a number of the highest and lowest values at each pixel. Charged particle events were removed by the COSMIC routine, in which each pixel is compared to its neighbors and replaced by the average if it exceeds a threshhold of four standard deviations above the background and 50% above the mean of the neighboring pixels. (These values were found by extensive experimentation with images).

Short-exposure images of Gunn-Thuan spectro-photometric standards were obtained. The atmospheric extinction coefficients listed in Kent (1985) were adopted; i.e., $a_g = 0.179$ and $a_r = 0.0806$. The adopted calibration magnitudes for one count per second above the atmosphere are $g = 21.8$ and $r = 22.55$. Galactic extinction in the B-band were obtained from NED and converted to g and r band extinction assuming $A_g = 0.9A_B$ and $A_r = 0.7A_B$. The 2.5σ detection isophote in the cluster candidate images is approximately $r = 25.5$ magnitudes per arc-sec^2 with the telescope at the zenith.

The Faint Object Cataloging and Analysis System (FOCAS) was used to detect objects, map limiting isophotes, and calculate various photometric and surface brightness quantitites. A detection isophote limit of 2.5σ was adopted. The r images, with their deeper detection limits, were used to define the isophotes of the objects. The g-band

images were then transformed to the pixel coordinates of the respective red images and the common isophotes used to evaluate g-magnitudes of objects. This allows for a more rigorous determination of galaxy colors since the flux is summed from the same solid angle of the sky in the different pass-bands. Fig. 12(a) compares the g magnitudes of 63 galaxies generated using the r isophotes against those using independent g isophotes. The deviation from perfect agreement with fainter magnitude is the flux lost due to the g detection isophotes shrinking. To determine whether slight offsets of the images or the effect of the finite-sized pixels might be causing a systematic error in the g magnitudes I compared the $g-r$ colors determined by common isophotes and those determined through 6.4" apertures. Fig. 12(b) demonstrates that any systematic error is negligible compared to the scatter.

As example of a typical optical counterpart to an extended IPC source and to illustrate the potential of combining X-ray and optical observations, I present an analysis of follow-up imaging to the X-ray source EX0806.3+2057. This source was detected at only 3.3σ significance in the 2.5 arc-min. aperture but 5.7σ in the 12.2 arc-min. aperture with a count rate of 0.021 sec^{-1}. It is assigned an extent probability of 93.5%. The neutral hydrogen column density in this direction is $n_H \sim 2.2 \times 10^{20}$ cm^{-2} (Stark *et al.* 1992). Assuming a 6 keV Raymond-Smith spectrum the X-ray flux in the 0.3-3.5 keV range is $5.6 \pm 1.0 \times 10^{-13}$ ergs sec^{-1} cm^{-2}.

Fig. 13(a) is a 4×4 arc-minute section of the field of the X-ray source EX0806.3+2057 centered on the X-ray emission. North is up and East is to the left. The cluster has two bright galaxies to the south and north-east of the X-ray centroid, each surrounded by a concentration of fainter objects. There is also a third disk galaxy to the south that is probably a foreground object.

A color-magnitude diagram of the galaxies within 2 arc-minutes of the X-ray center is shown in Fig. 13(b). Only galaxies brighter than $r < 22.5$ are plotted since this is roughly the corresponding detection limit of the g image. Several features of the $g-r$ color distribution of the $r < 22$ galaxies are evident. First there are a few very blue objects with $g - r < 0.4$, including the $r = 18.9$ galaxy with an obvious disk morphology. These have colors consistent with those of lower-redshift spiral field galaxies. There is a broad peak in the distribution centered at $g - r \sim 0.6$, and a narrower peak at $g - r \sim 1.1$ which includes the brightest galaxy in the 16 arc min^2 field.

The mean color of the five brightest galaxies in the red peak is $g - r = 1.10 \pm 0.02$

(assuming that uncorrelated error is responsible for the scatter of 0.05 magnitudes about this value). From (Molinari *et al.* 1990) this suggests a cluster redshift of 0.30 to 0.33 depending on whether the galaxies are as young as 8 Gyr or as old as 12 Gyr at the epoch they are observed. I compute the fraction of blue galaxies following the classical procedure (Butcher & Oemler 1984), with some modifications for the different band-passes involved. I adopt the absolute magnitude limit of $M_V = -20$ ($h = 0.5$) and $q - 0 = 0.5$. I use the photometry tranformation in (Molinari *et al.* 1990); $V - r = 0.723(B - V) - 0.468$ and assume $B - V = 1.0$ for the reddest (E/S0) and $B - V = 0.4$ for the bluest (spiral Scd and irregular) galaxies. For $z = 0.3$ K-corrections I use $K_r = 0.40$ for E/S0 galaxies (Schneider *et al.* 1983b) and 0.24 as an estimate for Scd galaxies. When the dust has settled, the cut-off has taken the form $r < 22 - 0.42(g - r - 0.4)$ and is plotted as the dashed line in 13. The vertical dashed line is the adopted color separation into red ($g - r > 1$) and blue ($g - r < 1$) galaxies. Correcting for the slope of the C-M relationship at this redshift, a total of 22 and 20 galaxies fall into the respective categories. The background is estimated from galaxies in the image outside of 5 arc-minutes (1.5 h^{-1} Mpc if $z_{cl} = 0.3$) from the X-ray center. The total background galaxy count to $r \sim 22$ is 1.3 per arc-min.^{2}, consistent with other estimates (see Chapter II). Estimated background counts in the inner 4 arc-min are 4.2 ± 1.5 red galaxies and 7.8 ± 2 blue galaxies. Thus the fraction of blue galaxies is $\sim 40\%$ but with uncertainties of 15% due to the small number of galaxies involved. The positions of the blue and red galaxies are plotted separately in Fig. 13.

The total absolute magnitude of the brightest red galaxy, assuming $z = 0.315$, $q_0 = 0.1$ and an r-band K-correction of 0.4 magnitudes (Hoessel & Schneider 1985), is $M_r = -22.37 \pm 0.03 + 5 \log h$. Postman & Lauer (Postman & Lauer 1995) found the average absolute magnitudes of Abell cluster BCGs within a 20 h^{-1} kpc diameter aperture to be $M_r = -21.27$ with a scatter of 0.32 magnitudes. To compare with this result, I assume a redshift of 0.315 and compute an angular diameter of 10.6". The corresponding aperture magnitude is $M_r = -21.86 \pm 0.03 + 5 \log h$. Thus only a few tenths of a magnitude of luminosity evolution is required to make this consistent with the low-redshift results. However, the $g - r$ color of 1.24 for the most distant BCG in the Hoessel & Schneider (1985) survey at $z = 0.2890$ is somewhat redder than what is found here. If one accepts a photometric redshift of $z \sim 0.3$, the X-ray luminosity of the cluster candidate is $\sim 7 \times 10^{43} h^{-2}$ ergs sec^{-1} [0.3-3.5 keV], respectable for a galaxy cluster. The 4 arc-minute field

represents a linear distance of 1.2 Mpc.

4.3 X-RAY CLUSTER CANDIDATES

4.3.1 BRIGHT SOURCES

As discussed in 3.4, a significant number of serendipitously-identified nearby X-ray clusters with fluxes above 5.5×10^{-12} ergs $sec^{-1}cm^{-2}$ [0.1-2.4 keV] have been detected by *Rosat* which do not appear in optical catalogs (Ebeling *et al.* 1996). An independent search for X-ray bright, non-Abell clusters using sources serendiptiously identified in the extended source analysis of *Einstein* IPC data would be useful.

The equivalent emitted flux in the *Einstein* 0.3-3.5 keV band is 6.9×10^{-12} ergs sec^{-1} cm^{-2}. To convert this into an IPC count rate, I assume the canonical cluster has a 6 keV thermal bremstrahhlung spectrum, lies at a redshift of 0.1, and is observed through a neutral hydrogen column density of 4×10^{20} cm^{-2}. I find an IPC count rate of 0.22 cts sec^{-1}. Unfortunately, the sky coverage of the AEXCS at this flux limit is roughly 1100 deg^2 (excluding cluster pointings) and thus one is hopelessly dominated by low-number statistics. The expect number of Abell and non-Abell clusters at the flux limit is ~ 5 and 3, respectively. In the serendipitous (i.e., non cluster target) IPC pointings, I find 2 Abell clusters, 1 non Abell cluster, as well as a single unidentified extended source (see below). To these I add the target clusters, their numbers weighted by the ratio of the serendipitous sky coverage to the area of the entire sky above $|b| = 15°$ (a factor of 0.036). There are 47 Abell clusters and 9 non-Abell clusters in the targeted images, leading to equivalent totals of 3.7 and 1.3. The only firm conclusion that can be drawn from this is that the extended source analysis of the IPC images does not lead to the discovery of a significant excess of bright X-ray clusters on the sky over the numbers already detected by previous *Einstein* and *Rosat* analyses.

4.4 SOURCES WITH $P_E > 0.99$

I next examine those unidentified sources which appear significantly extended in IPC images and are the most promising candidates for $z < 0.3$ clusters of galaxies. A combined SIMBAD

and NED search at the coordinates of the 121 sources in the IPC source list with $P_E > 0.99$ found 14 galaxy clusters, 8 galaxy groups, the nearby galaxy Messier 101, 2 EMMS sources identified as galaxies, and an additional 35 sources identified with nearly point-like sources such as AGN and stars, individual galaxies, and ultraviolet sources. A measurement of the random coincident match rate for these sources was conducted by shifting the input declinations by 1 degree. I found that with a 3 arc-minute matching radius, a conservative choice designed to eliminate all possible point sources from the catalog, the rate of spurious matches is 15%, or 18.

The two EMMS sources, MS1224.7+6733 and MS2357.5-6352, have offsets of 4.3 and 5.6 arc-minutes from the X-ray source centroid. Both are identified as low-redshifts AGN ($z = 0.153$ and $z = 0.136$, respectively). The optical identification of the EMSS sources appears to be unambiguous (Henry *et al.* 1992). It is possible that additional background or foreground sources are mimicing an extended source. The forty-three unidentified extended sources are listed in Table 2. DSS images of these indicates about 1/3 are possible clusters within reach of the photographic plates.

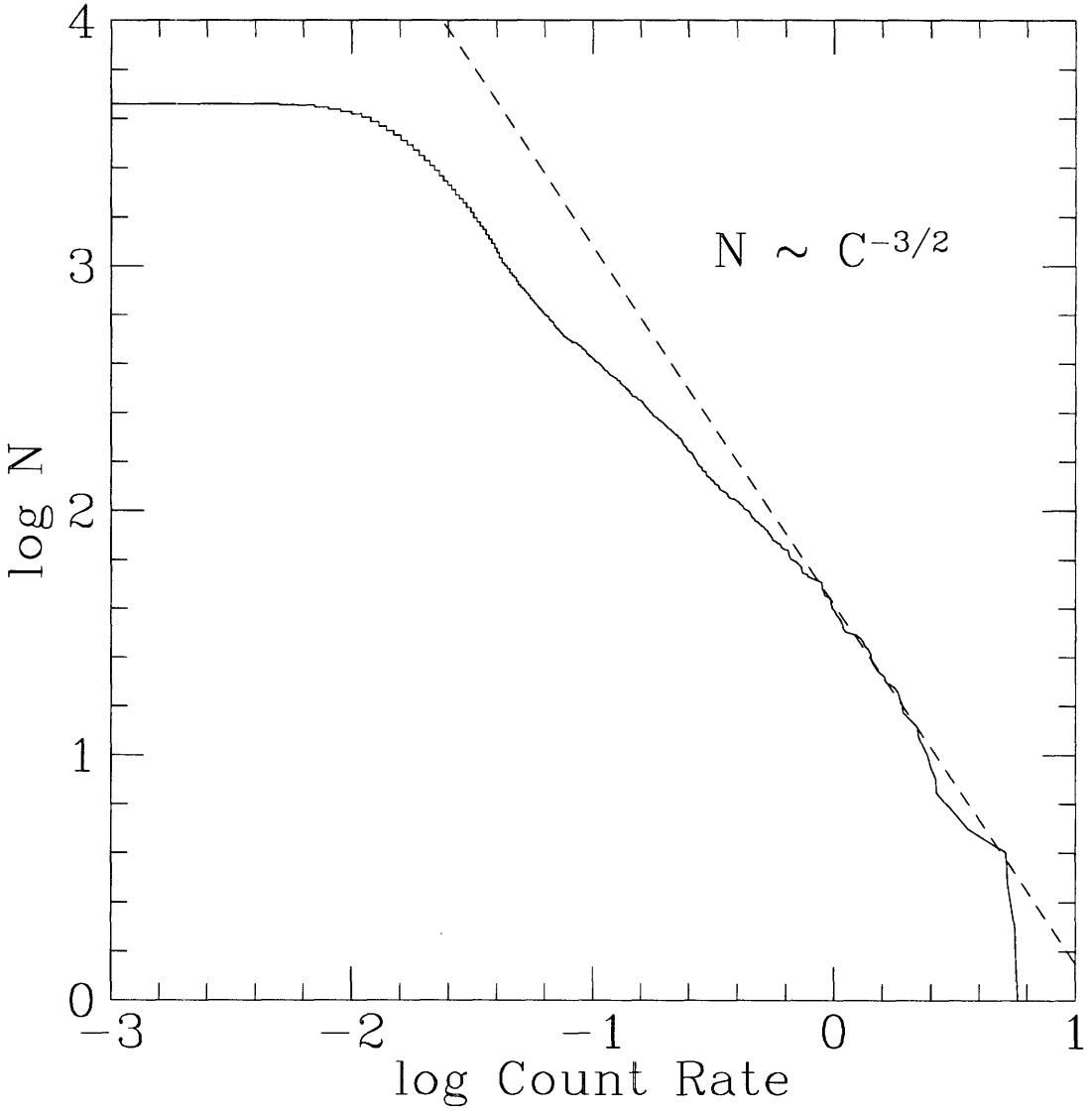

Fig. 1.— IPC Source Counts
Log N-log S plot of the high galactic latitude sources detected in IPC fields. The count rate in the 8.4′ aperture is used. The -3/2 slope for a uniform survey of homogeneously-distributed, non-evolving sources is shown for comparison.

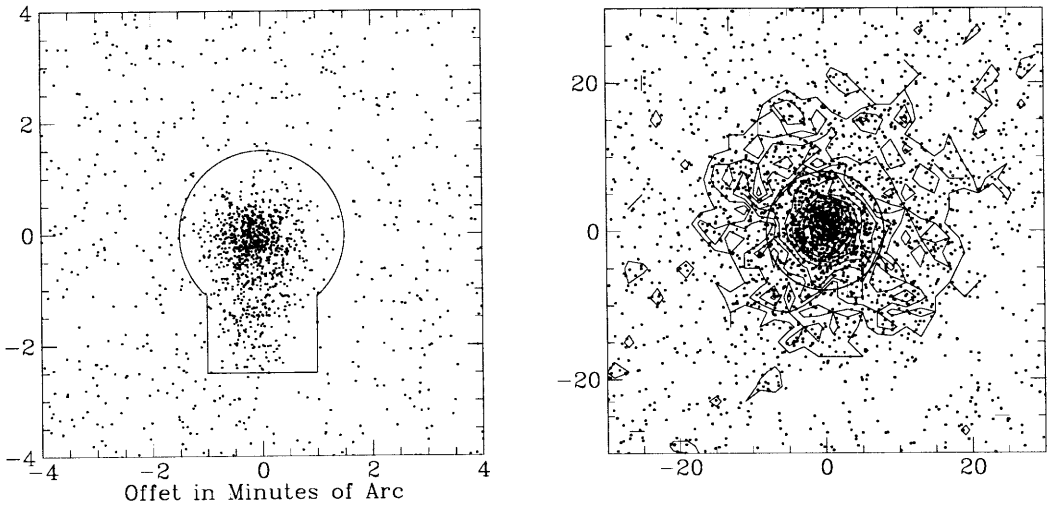

Fig. 2.— X-ray Source Identification
Left: offsets between the IPC X-ray sources and the nearest EINLINE point sources. The "keyhole" contour is the line within which a match is declared; **Right:** offsets with Abell clusters with countour lines overlaid. The heavy circle is the adopted 8 arc-minute matching radius.

Table 1: Point sources with $P_E > 0.99$

	$\sigma_{1.25}$	ID	Object	Offset [']	z	m_V
EX0346.2-0106	9.3	GD 50	White Dwarf	< 1	N.A.	13.77
EX1441.7+5209	9.0	AG+52 1002	F8 star	< 2	N.A.	8.70
EX1907.0-6404	10.1	1E1907.0-6405	K4V star	< 1	N.A.	11.79
EX0044.4-2058	6.7	KUV00445-2058	UV source	< 1	N.A.	16.30
EX0536.5-2817	8.0	1E0536.5-2818	AGN	0.4	0.270	19.00
EX1430.1+6237	5.3	QSO1430+626	AGN	0.6	0.402	18.80
EX1558.0+4124	3.5	MS1558.2+4123	AGN	1.4	1.168	17.69

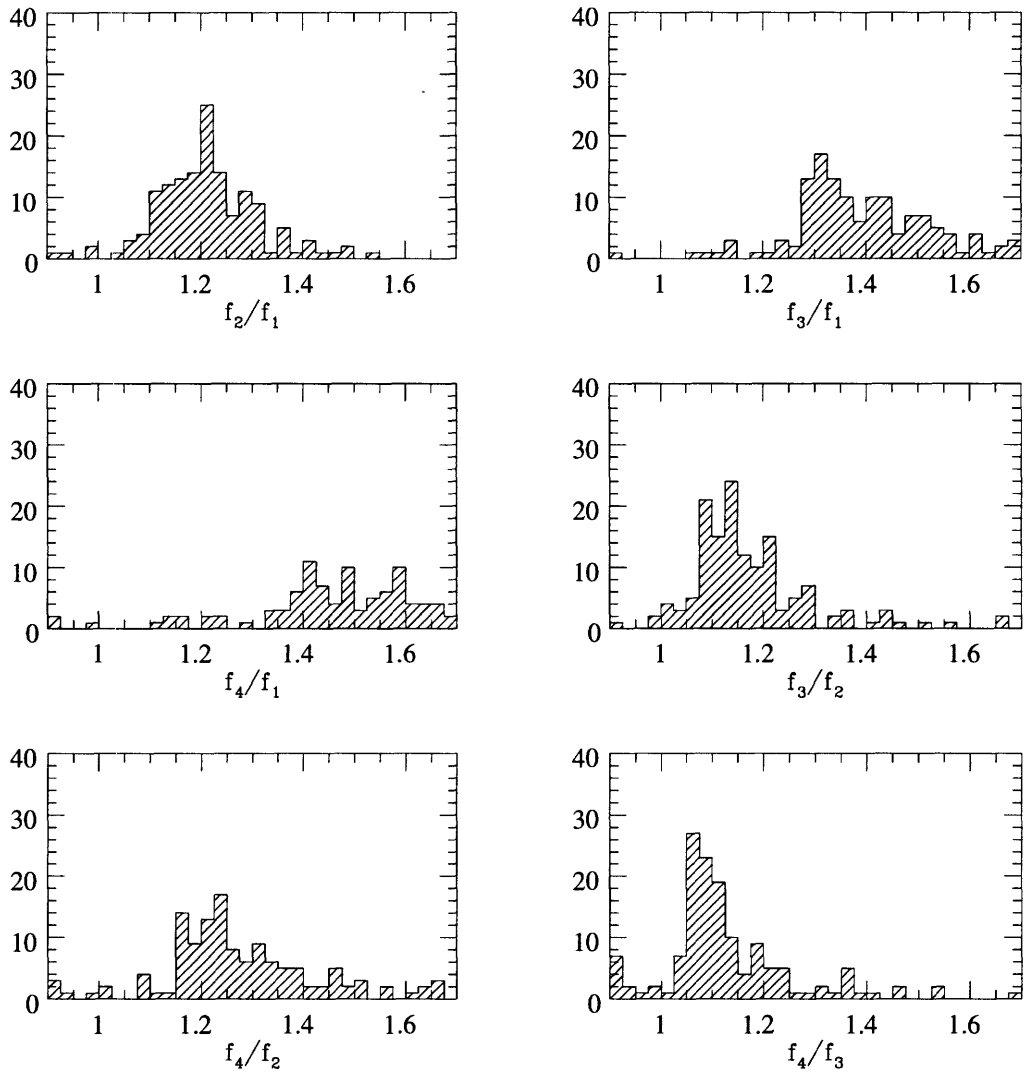

Fig. 3.— Flux ratios of point sources
Ratio of fluxes between apertures 1 (2.5'), 2 (4.7'), 3 (8.4'), and 4 (12.2') for known points sources with $\sigma_1 > 10$.

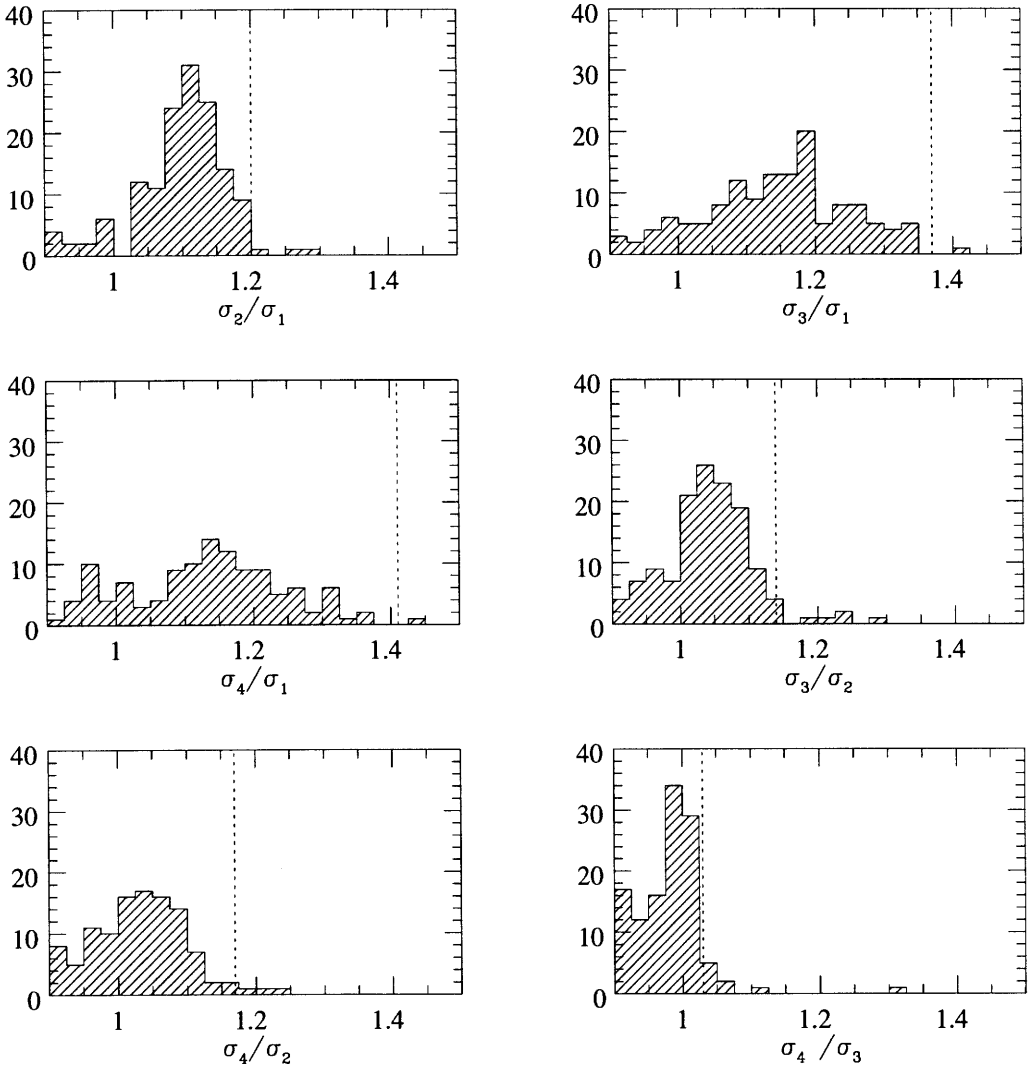

Fig. 4.— Signal-to-noise ratios of point sources
Ratio of signal-to-noise between apertures 1 (2.50'), 2 (4.7'), 3 (8.4'), and 4 (12.2') for known points sources with a $\sigma_1 > 10$. The dashed lines are the adopted extendedness criteria. Extented sources must fall to the right in two or more ratios.

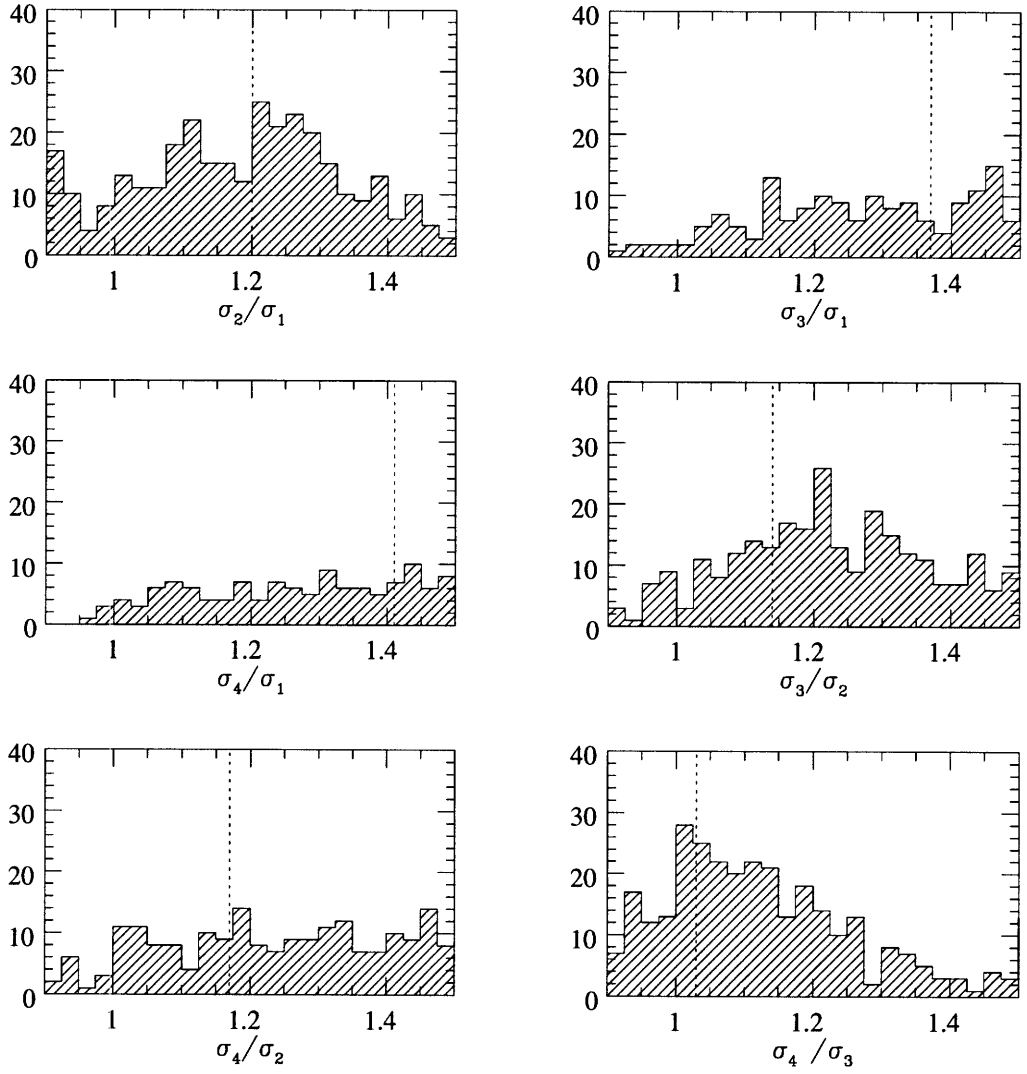

Fig. 5.— Signal-to-noise ratios of Abell clusters
Ratio of signal-to-noise between apertures 1 (2.5'), 2 (4.7'), 3 (8.4'), and 4 (12.2') for Abell clusters with count rates in all four apertures. The dotted lines are adopted cut-offs to which objects must fall to the right of to satisfy the extendedness criterion.

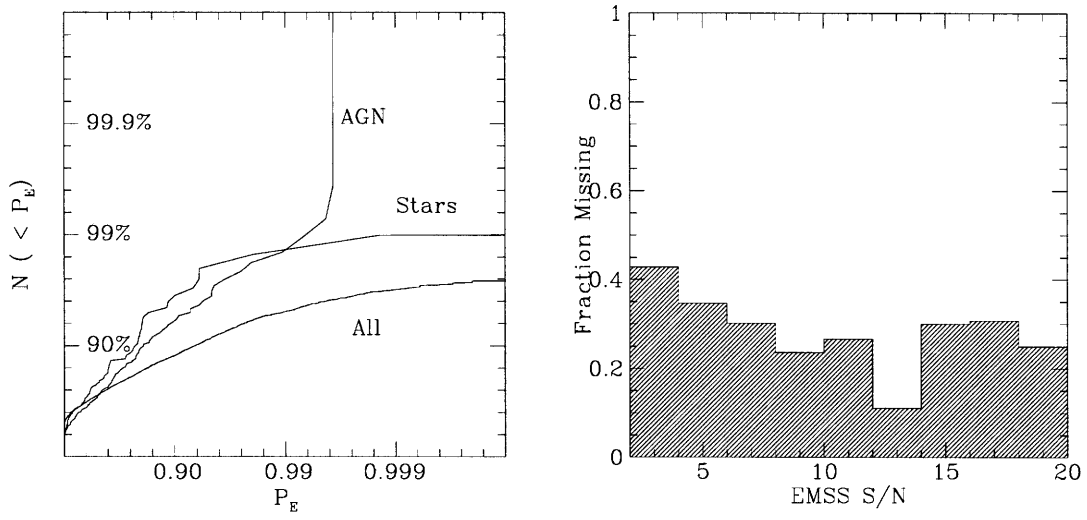

Fig. 6.— Extent Probability & EMSS Recovery
Left: Cumulative fraction of AGN, stars and all IPC sources with probability of extent $< P_E$. At a threshhold of $P_E = 0.99$, 98.5% of stars and AGN are rejected; **Right:** Fraction of EMSS sources that are not recovered in the IPC source catalog used here vs count-rate.

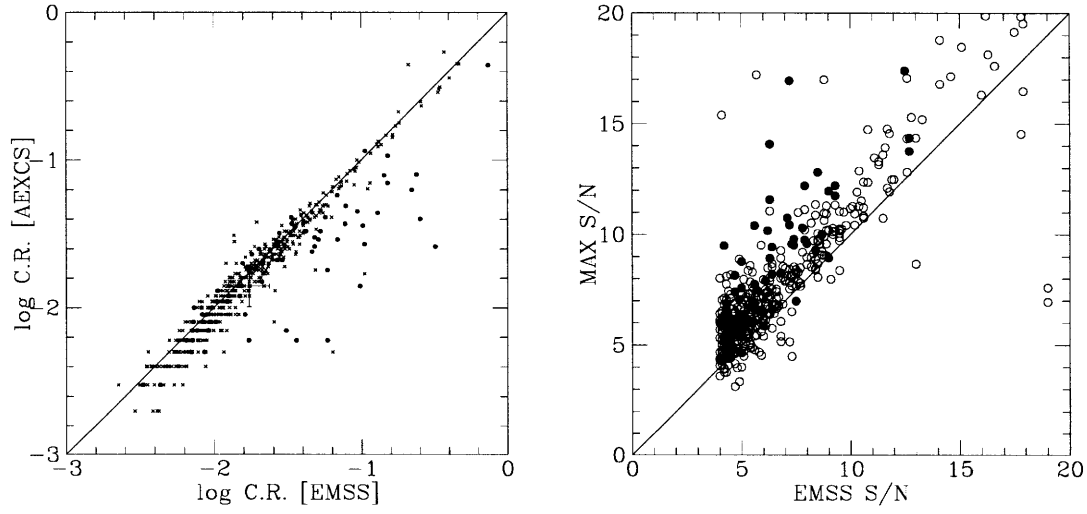

Fig. 7.— EMSS/Archival IPC comparison
Left: Comparison between the EMSS reported count rates and the measurements obtained in the archival IPC source catalog for the 2.5' aperture; **Right:** comparison of the signal-to-noise in the IPC sources versus EMSS surveys.

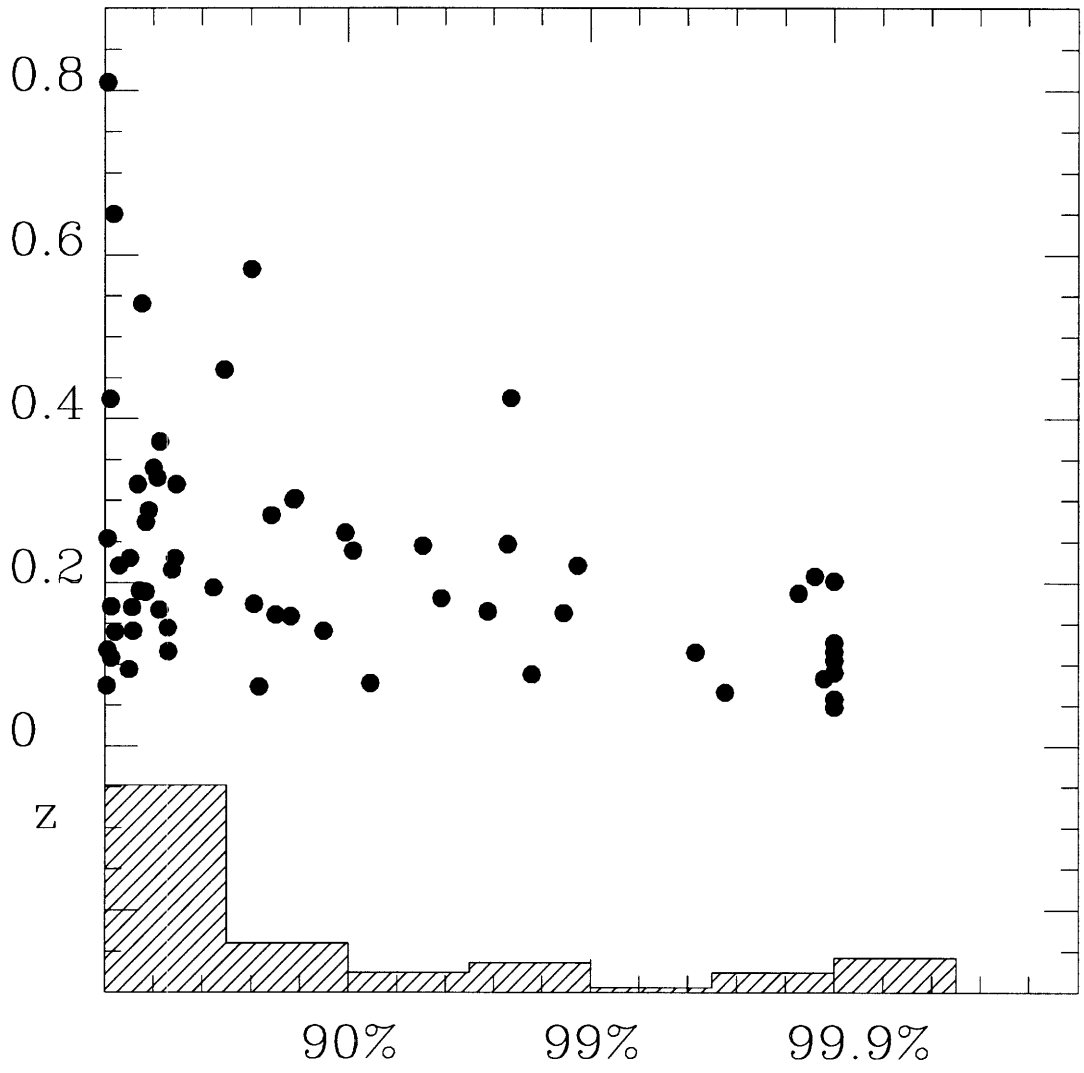

Fig. 8.— X-ray Extent of EMSS Clusters
Probability of extent of EMSS clusters versus their redshift. A histogram of the P_E values is also shown.

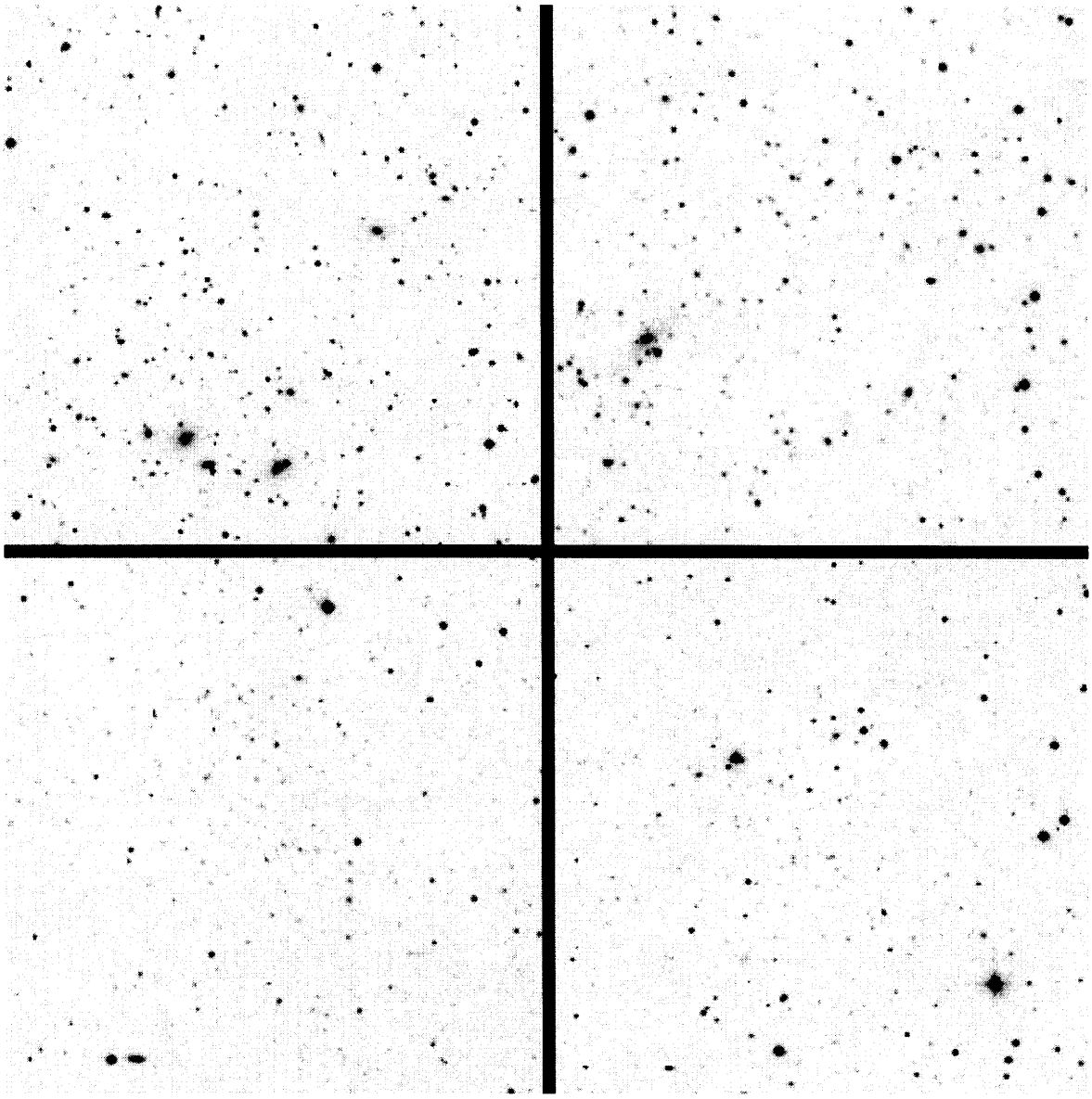

Fig. 9.— POSS E images of Abell Clusters
Digitized Sky Survey images from POSS E (red) photographic plates. These are 15×15 arc-minute fields of richness class 2 Abell clusters. Clockwise from upper left; A2256 (z = 0.058), A1235 (z = 0.104), A1094 (z = 0.200), and A1622 (z = 0.286).

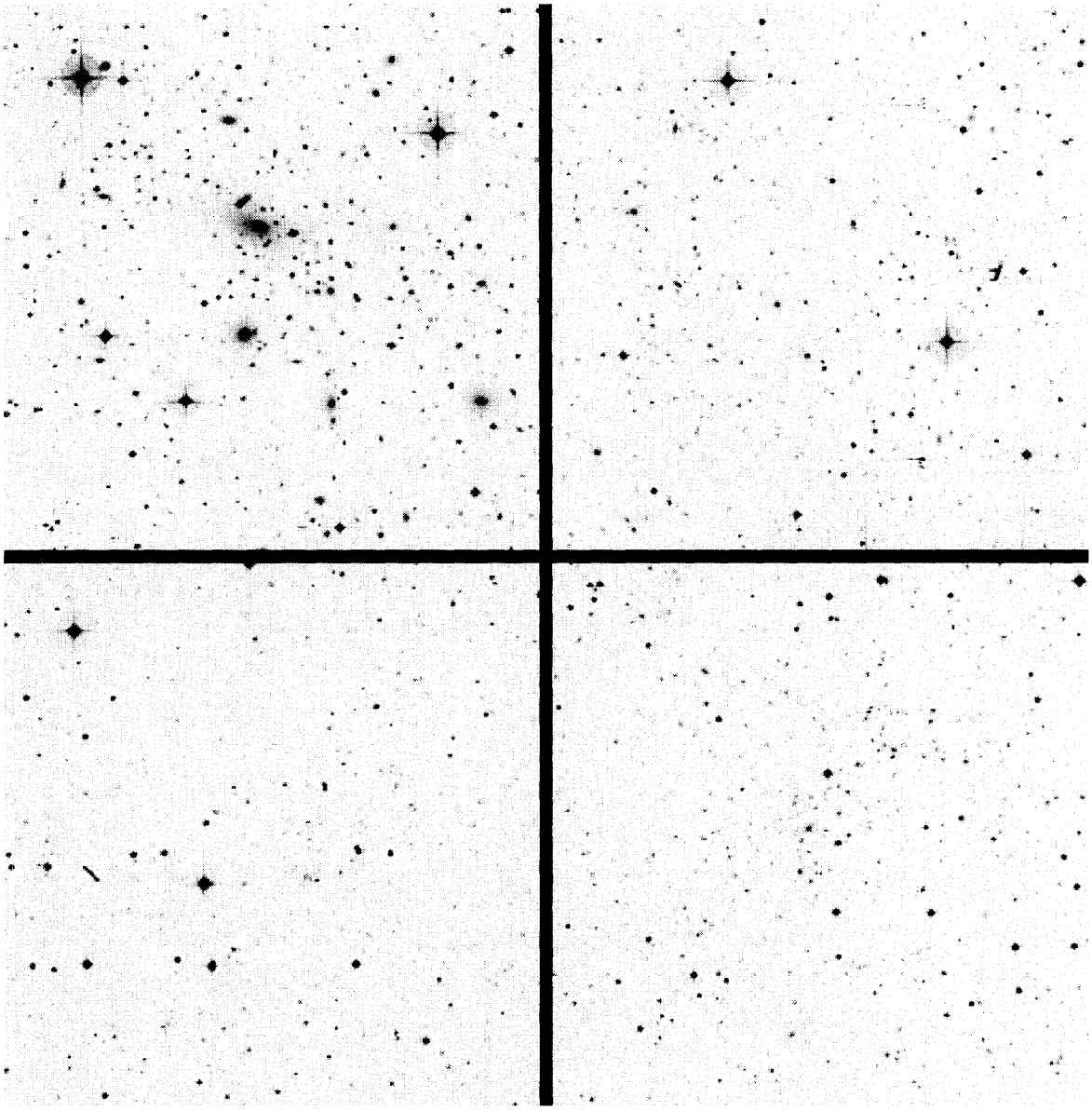

Fig. 10.— UK Schmidt J Images of Abell Clusters
Digitized Sky Survey images from UK Schmidt J (blue) photographic plates. These are 15 × 15 arc-minute fields of richness class 2 Abell clusters. Clockwise from upper left; A3266 (z = 0.059), A2541 (z = 0.108), A2534 (z = 0.198), and S1077 (z = 0.312).

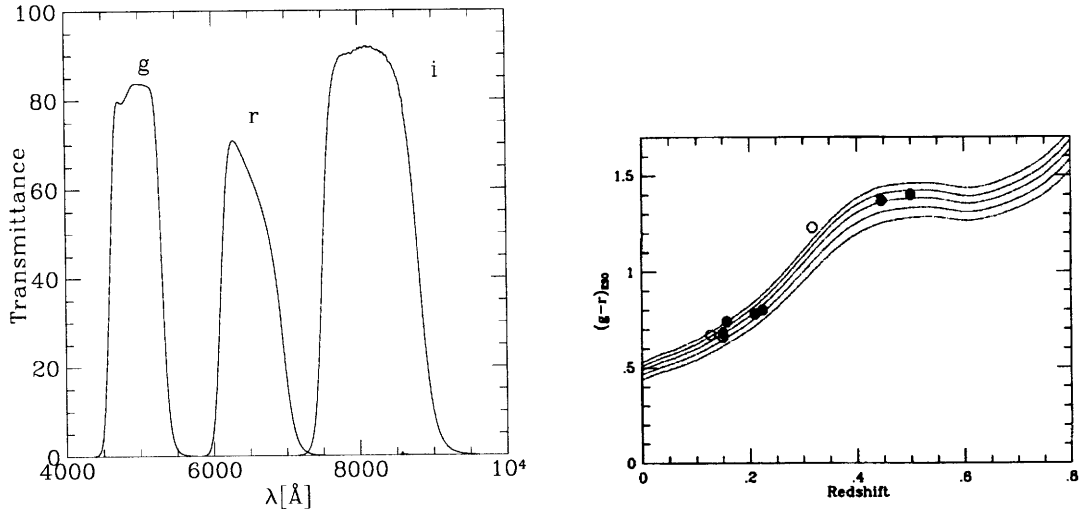

Fig. 11.— Gunn Filters and Elliptical Colors
Left: Transmittance plot of the Thuan-Gunn *gri* filter system used in the cluster galaxy photometry program; **Right:** Predicted observer-frame $g - r$ colors of passively evolving elliptical galaxies (Buzzoni 1989). the different curves correspond to ages of the galaxy when it is observed of 6, 8, 10, 12.5, and 15 Gyr (moving to redder colors). The points are unrelated observations of clusters.

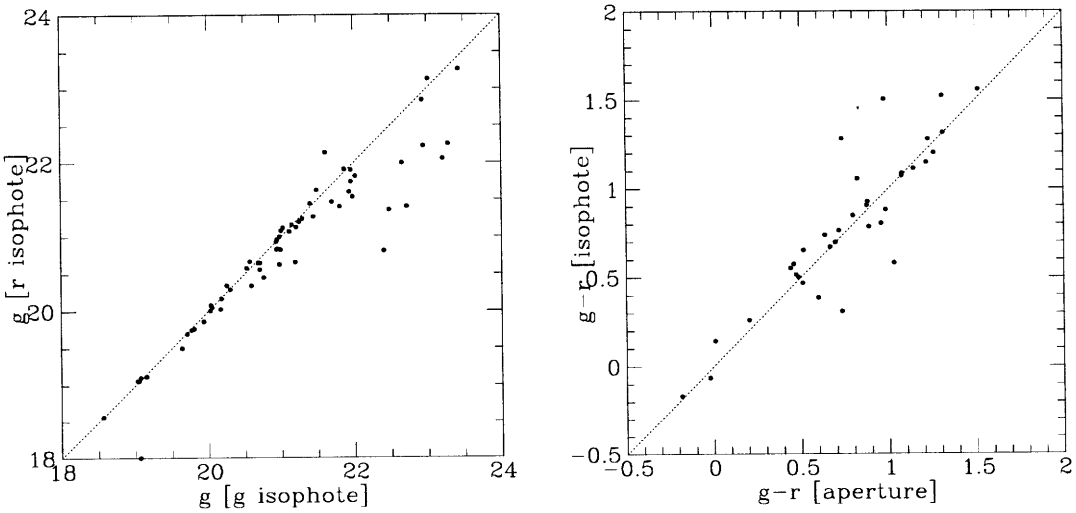

Fig. 12.— CCD Photometry Tests
Left: comparison of g photometry generated from r image isophotes to that from independent g isophotes. **Right:** comparison of g photometry obtained with r isophotes to aperture photometry.

Fig. 13.— EX0806.3+2057 Imaging

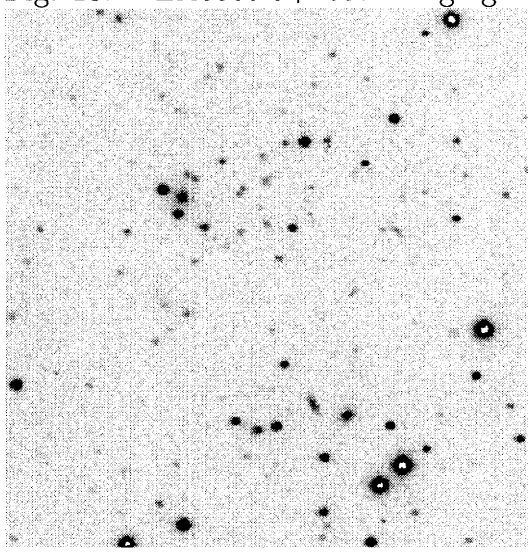

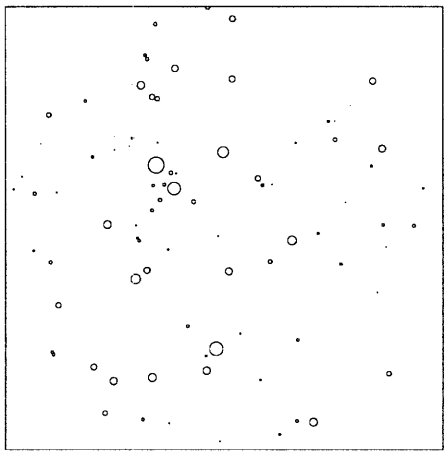

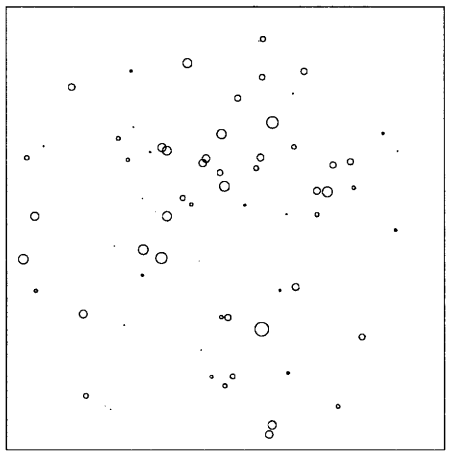

g−r > 1

g−r < 1

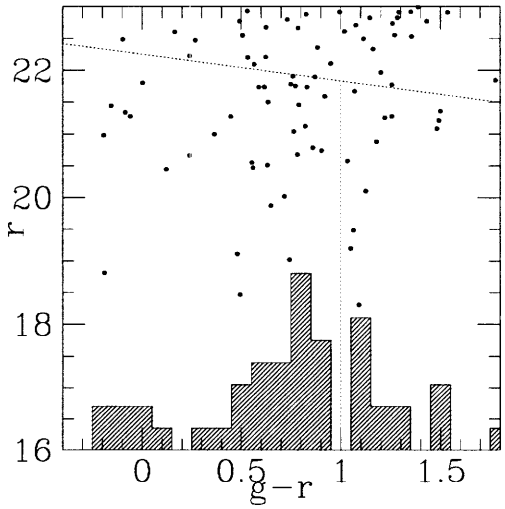

Top: 4 × 4 arc-minute section of a 900-second r-band CCD image centered on the X-ray source EX0806.3+2057 ($P_E = 0.94$); **Bottom:** color magnitude diagram of galaxies within 2' of the X-ray centroid of EX0806.3+2057. **Middle:** spatial distribution of red ($g - r > 1$) and blue $g - r < 1$) galaxies.

Table 2: Unidentified Extended X-ray Sources

R.A. [B1950]	Dec.[B1950]								
hh mm ss.ss	dd mm ss.s	$f^a_{1.25}$	$f^a_{2.35}$	$f^a_{4.20}$	$f^a_{6.10}$	$\sigma_{1.25}$	$\sigma_{2.35}$	$\sigma_{4.20}$	$\sigma_{6.10}$
0 18 07.90	- 75 06 05.7	1.848	3.080	4.312	8.316	2.75	2.89	5.78	6.35
0 55 25.77	+ 30 20 17.4	0.616	3.696	1.848	5.236	2.63	2.58	3.68	6.35
1 34 48.18	- 05 04 35.9	3.696	5.236	12.628	19.404	3.05	3.22	4.58	6.53
2 24 55.31	- 10 41 38.4	1.540	3.080	7.084	8.932	3.61	3.39	5.91	6.83
2 55 43.32	+ 20 41 55.7	0.000	4.312	4.312	10.164	0.00	3.09	3.03	5.51
4 08 58.92	- 10 21 44.1	2.772	3.696	9.856	13.860	2.97	2.59	4.68	5.76
4 10 06.18	+ 07 37 54.6	1.232	3.080	5.852	11.704	2.69	2.89	4.35	5.97
4 45 01.94	- 59 37 09.0	1.540	2.772	5.852	10.164	2.51	2.68	4.11	6.25
5 03 35.45	- 11 44 09.4	0.616	1.540	3.080	6.468	3.29	2.53	4.74	5.58
5 26 47.17	- 20 36 10.2	0.924	1.848	3.388	7.392	2.73	2.95	3.74	6.06
5 36 30.52	- 28 17 53.0	2.156	3.080	5.852	8.008	7.95	6.37	8.22	10.52
6 01 09.06	- 31 58 52.5	0.000	5.852	10.164	19.404	0.00	2.64	3.67	5.50
8 37 24.85	+ 13 12 58.2	0.924	0.924	4.928	6.160	3.46	3.11	6.22	6.68
8 42 01.67	+ 19 16 00.0	0.924	1.848	4.928	5.544	2.93	2.78	4.56	5.15
10 10 21.82	+ 49 49 03.9	3.080	4.620	4.928	13.552	3.35	3.56	3.16	6.34
10 45 52.61	+ 06 59 18.9	2.772	7.084	11.704	14.784	2.57	2.88	4.75	5.76
11 01 40.51	+ 45 32 13.3	0.616	2.156	4.620	7.700	2.68	3.53	3.31	6.67
11 21 08.64	- 08 35 48.6	1.232	3.696	7.084	10.780	3.34	3.42	4.40	6.11
11 43 18.06	- 04 25 56.0	2.772	3.696	8.316	20.020	3.53	3.72	3.32	7.49
11 56 08.83	- 27 14 25.8	1.848	3.696	5.544	12.320	2.93	2.52	4.60	6.31
12 48 37.53	- 00 56 12.7	1.232	2.464	4.928	6.776	3.11	4.33	5.91	6.97
12 49 51.48	- 01 06 58.7	0.616	2.156	3.696	7.084	3.15	2.83	3.96	5.93
12 50 59.90	+ 56 35 16.4	0.000	2.156	4.928	8.624	0.00	2.70	2.77	5.10
13 20 14.14	+ 42 40 23.3	0.924	3.696	5.852	10.164	2.73	2.95	3.21	5.57
13 22 42.43	- 10 56 21.1	2.772	4.312	63.448	16.632	2.83	3.03	19.63	4.39
13 33 27.49	+ 51 58 43.1	0.000	3.080	12.320	19.096	0.00	2.69	3.99	6.35
14 04 28.97	+ 72 33 24.3	0.000	3.388	8.316	15.708	0.00	3.25	3.72	6.62
14 30 46.31	+ 05 53 54.0	1.540	1.848	5.544	8.932	2.93	2.54	4.43	5.85
14 33 35.50	+ 19 37 04.2	0.000	4.620	7.084	16.632	0.00	2.94	3.99	5.94
14 48 41.86	+ 19 34 20.4	3.080	6.160	6.776	16.324	3.02	3.14	3.26	5.81
15 06 53.33	+ 57 13 32.1	0.000	3.696	12.936	17.864	0.00	2.62	4.90	5.99
15 25 26.52	+ 11 19 23.4	0.000	4.312	8.932	11.704	0.00	2.66	3.93	5.18
15 33 51.80	+ 23 28 27.2	0.616	3.388	4.620	4.620	2.88	4.79	6.40	6.01
15 43 59.59	+ 01 00 46.5	0.000	4.620	14.784	17.864	0.00	3.11	5.69	6.30
15 47 19.05	+ 05 52 30.6	0.000	7.700	11.396	22.792	0.00	3.18	3.41	6.27
15 48 19.89	+ 12 31 11.1	0.616	1.540	4.620	9.240	2.98	2.54	3.61	6.78
15 59 29.26	+ 08 39 10.6	1.540	2.772	7.700	17.556	3.58	3.09	5.00	6.98
16 43 18.11	- 03 21 48.1	0.924	2.464	4.620	7.700	2.87	2.55	4.63	5.47
17 02 18.39	+ 60 55 21.6	1.540	6.160	7.700	5.236	2.57	3.11	3.55	8.59
17 06 44.97	+ 49 08 20.0	3.388	4.928	12.628	18.172	2.90	3.20	4.73	6.41
17 07 55.45	+ 70 54 46.3	0.308	1.232	1.848	4.004	3.48	3.54	4.91	7.67
17 17 29.85	+ 17 39 58.5	1.232	1.232	9.548	9.240	3.28	2.76	10.39	7.30
18 52 23.25	+ 79 34 40.8	1.232	1.540	4.620	7.700	3.03	3.25	3.53	7.09

Note. — (a) preliminary fluxes calculated assuming a bremstrahllung specctrum, $T_e = 6keV$, $z = 0.25$, and $N_H = 3 \times 10^{20}$.

Chapter 5

Look-Back Time

5.1 A Picture-Puzzle of Galaxies and Clusters

Near a small village in the south-west of France there are the beautiful structures of a partially-rebuilt Roman villa approximately 1700 years old. The prize heirloom of the site is a spectacular floor consisting of many tens of thousands of individual color tiles. Along with the villa ruins the floor, I was told, had lain buried in a farmer's field, and had to be painstakingly reconstructed after the effects of many years of tilling. May the cosmologists have it so easy....

However, the results presented in this thesis join a host of other evidence that do encourage hope for the future decription of the formation and evolution of galaxies. First of all, it seems clear that the luminosity function of bright galaxies in clusters *is* described in basic form by a Schechter function with $\alpha \sim -1$ that is very much like that observed in the field (Loveday *et al.* 1992; Marzke *et al.* 1994; Lin *et al.* 1996). There is no evidence for a steep faint-end slope except perhaps at absolute magnitudes where deeper imaging and a more careful completeness correction is needed. The flat faint-end slope found in the cumulative LF, and the large size and more-or-less random selection of the cluster sample provide strong evidence that a steep up-turn in the numbers of galaxies brighter than than $M_R < -16.5$ (about $M^* + 4$) is very rare in clusters, at least in cluster cores.

It is not altogether surprising that there is an absence of dwarf galaxies in the cores of clusters, even if they are/were abundant in the field, given that some theories predict a hostile environment in the former. Dwarf galaxies might be expected to be depleted of gas or

destroyed from the effects of stripping or tidal disruption. De Propis *et. al.* (1995) suggest that dwarf galaxies *remain* abundant in clusters because the dense intracluster medium inhibits the escape of gas from their shallow potential wells; presumably an analogous population in the field have suffered such a fate. This seems implausible given that the velocity dispersion of the cluster is so much higher than the escape velocity from the shallow potential wells of these objects. Another possibility is that the dwarfs have been cannibalized or tidally disrupted by bright galaxies in the field, but have escaped this fate in the cluster due to the relatively high velocity dispersion. Finally, dwarf galaxies might be *produced* in clusters from the debris of galaxy-galaxy collisions (Moore *et al.* 1996). My results do not appear to look favorably on these models.

In addition, although the cores of clusters may be depleted in dwarf galaxies due to gas stripping or tidal disruption, I note that one is observing the total projection onto the sky, which includes the outer parts of a cluster as well (a $1 - 2/\pi$ or 36% contribution, in the spherical cluster model). Thus the data seems to rule out any bright upturn in the outer parts of the cluster as well.

What is disturbing about the entire situation is the fact that for imaging of clusters at $z = 0.1 - 0.2$ the background field counts become the dominant component right at the absolute magnitude $M_R \sim -19$ where the purported upturn appears. As I have discussed, systematic errors in field counts can have devastating consequences for the accuracy of the LF at fainter magnitudes. Unfortunately, no clusters in my sample have been observed and analyzed by other researchers, so a direct test case cannot be done. Thus, to re-phrase a famous astronomer, "the luminosity function wars continue", only now with a little more ammunition.

The flat luminosity functions found both in the field and in clusters strongly support the theory that galaxy formation was regulated by the pre-heating of the inter-galactic medium at some earlier epoch [see §1.1 and Appendix A]. The upturn at faint magnitudes, if it exists, may be a distinct population of objects whose formation was controlled by other processes (such as SN heating of the gas).

The small dispersion of the asymptotic magnitudes of brightest cluster galaxies about a secular evolution with redshift is particularly interesting in light of the emphasis of their use as "standard candles". This data supports the view that the BCGs evolve with the cluster and once objects of this magnitude form, they evolve only passively with the intrinsic

stellar evolution. The correlation between the morphology/core density of clusters and the magnitude of the brightest galaxy (at least in the CCD imaging) is very good evidence that these creatures form during and after a cluster forms. Why there is a gap of about 0.5 magnitude between the first and second-ranked galaxies in clusters is not certain, but a clue might be found in the case of Abell 2142, a "bimodal" cluster with two giant elliptical galaxies of nearly equal luminosity. The photometry of Abell 2142 is not secure and so was not included with the data, but if one plots the absolute magnitudes of the twin BCGs they fall neatly into the gap. The final evolutionary state of most BCGs may be the coallescing of two roughly equal systems. The gap indicates a paucity in the number of binary systems, which assuming that there is no hidden bias in my sample, would indicate that this process happens in a small fraction of a Hubble time. In my sample there are 4 clusters with binary Rood-Sastry types and 50 cluster with less-evolved Rood-Sastry types, suggesting that the mergin time is les than a tenth of a Hubble time ($\sim$ 1 Gyr). The relative luminosity of the brightest galaxy fainter than the gap seems to be a good evolutionary "clock" for the cluster. The appearence of the BCG at $M_R \sim -23.7$, however, signifies that the clock has stopped (and in fact is slowly ticking backwards).

My observation of an increase in the number of disk-like systems in clusters with redshifts does agree with the expected Butcher-Oemler effect and does suggest evolution of galaxy *morphology* in clusters, where disks are being turned into earlier types. Finer discrimination using colors and a larger sample to a higher redshift is needed to determine if the effect does indeed parallel that of Butcher & Oemler (1984), and whether spirals are being turned into S0 galaxies or ellipticals. This last issue is a very important distinction, since if disks are turned into S0s in clusters (as seems plausible), the formation of elliptical galaxies must have been a separate, more primordial process. Perhaps both "nature" and "nurture" are responsible for these types of galaxies.

Finally, my search of the archival Einstein IPC database has turned up a large number of cluster candidates, some of which, like EX0806.3+2057, which appear to be distant clusters in follow-up multicolor CCD imaging. What I do not find is any evidence for a large number of bright, nearby X-ray clusters much in excess of the Abell catalog. Thus the discrepancy between the normalization and evolution in optically-selected and X-ray selected clusters remains a mystery.

5.2 Lessons Learned from My Field Work

Although interesting results have been obtained from this data, a considerably great deal more could be learned by a more careful and systematic effort that uses some of the lessons learned from the many mistakes made here.

In terms of luminosity function construction, the choice of cluster sample certainly deserves more careful attention so that a uniform sample is created that covers the full range of some parameter of interest, such as the dynamical age of the clusters. In particular, observing clusters in some narrow range range of redshifts (perhaps $z \sim 0.15$) now seems like a very good idea. Selecting clusters from the *Rosat* Brightest Cluster Sample (Ebeling *et al.* 1996), or Brightest Abell Cluster Sample (Jones *et al.* 1996) (which were not available at the beginning of this project) is an obvious thing to do. Another possibility are the nearby, bright X-ray clusters for which *Rosat* pointed imaging with long integration times is available. The X-ray surface brightness morphologies can be used as an indication of the dynamical state of the cluster, and hence its age (Buote & Tsai 1996). An alternative scheme would be to select clusters with photometry of the first-ranked galaxies and use the hypothesis, supported by the results of this thesis, that these objects grow to be the Brightest Cluster Galaxies (or "Asymptotic Cluster Galaxies"), and until reaching that limit serve as a "clock" for the host cluster.

In a more technical vein, the plethora of possible systematic errors in background subtraction, many of which were discovered as the project progressed, strongly suggest the use of a differential background subtraction rather than unassociated fields. Perhaps the optimal strategy would be to image in a strip running from the cluster core out to a distance of about 3 Mpc where the cluster density has fallen to a very low value. The "drift scan" mode of CCD operation in which the telescope is fixed and the CCD clocked to match the sidereal rotation rate of the Earth, comes to mind. For cluster out to $z \sim 0.2$ one should exploid the Digitized Sky Survey to center the imaging and avoid the pitfall of the erroneous Abell coordinates. The use of filters in common with the large sky surveys to avoid the uncertainties associated with transforming from one photometry system to another is very important: It seems clear that to compare with the Las Campanas Redshift Survey and the upcoming Sloan Digital Sky Survey, the Gunn system filters are the pass-bands of choice. Finally, the amount of additional science that can be obtained with the use of an

additional filter to construct colors is well worth the extra observing time required. The color information is also necessary for more accurate estimates of the K correction!

5.3 Looking Forwards

One of the more interesting and timely topics explored in this thesis has been the development of the "Q" parameter for the morphological classification of galaxies. It seems to separate disk systems and spheroidal systems with accuracy and has been demonstrated to be a quantity that is quite robust to large variations in seeing and signal-to-noise. A potentially powerful technique would be to combine it with a measurement of the mean surface brightness and a single color to attempt to resolve out differences in morphologies, stellar populations, and star-formation rates in distant galaxies. Application of this classification to Hubble Space Telescope images of moderate depth will be useful. Another application is to the low signal-to-noise images generated in obtaining CCD photometry for redshift surveys such as the Las Campanas Redshift Survey.

The other topic of great interest is the passive evolution of the elliptical population in clusters. Mounting evidence, e.g., (Stanford *et al.* 1995) points to absolutely very little going on with these objects other than the normal evolution of a stellar population that formed at very high redshift. Multi-color photometry of these objects, combined with the latest stellar evolution and spectral synthesis codes, can begin to place some interesting limits on the redshift of formation (Rakos & Schombert 1995). This problem ties in *directly* with the now well-known conflict between the best estimates of the Hubble constant (60-75 km $\sec^{-1}$ Mpc^{-1}) and the estimated ages of globular clusters ($\sim$ 14 Gyr). It would be as if, as paleontologiests, we discovered fossils that were older than the Earth! These values cannot be reconciled in standard cosmologies without resorting to the Faustian bargain of invoking a cosmological constant. Brave souls have already begun to explore the possibility of testing cosmological models at more than one epoch (i.e., now) by using the color evolution of cluster ellipticals (Buzzoni *et al.* 1993). More fundamental (and less controversial) tests of world models have also been done (Pahre *et al.* 1996) and the possiblity of using the basic properties of elliptical galaxies as yardsticks to measure the decelleration parameter has been proposed. Of course, much of this is entangled with our knowledge of stellar evolution and the formation of stars in those ancient starbursts, but the size, homogeneity

and well defined behavior of the sample does lead one to dare hope to know the cosmological parameters at last.

Will we see a time when the formation of galaxies and subsequent evolution of galaxies is well understood, with studies confined to the exceptions rather than the rule? It may seem a ridiculous possibility but, staring at the image of the Hubble Deep Field (Williams *et al.* 1995) which probably sees through the entirety of the optically observable universe, the question does not seem so silly. Will the day arrive when tests using distant objects like elliptical galaxies, among other tests, finally converge to some irrefutable cosmological model whose parameters, be they Ω, Λ, or whatever, are quickly measured to an accuracy sufficient for astronomers, and, much more slowly, to a precision acceptable to atomic physicists; set to take their place alongside the speed of light and Planck's constant in the "CRC"? On a personal note, this author hopes the answer is no: May there always be that fainter, more distant object to see, that piece of the puzzle that does not fit, that artifact that does not make sense, that bone that does not belong, and always one more Mask that hides the Face.

Appendix A

Eine Kleine Theory: Galaxy Formation

In the succeeding discussion I will often assume $\Omega = 1$. Although there is a body of observational evidence suggesting that $\Omega_m < 1$, perhaps taking a value ~ 0.2) (Coles & Ellis 1994), there is also substantial evidence that the bulk of the galaxy formation occured at a redshifts of 3 or higher (Steidel *et al.* 1994; Steidel *et al.* 1996) where Ω_m would have been much closer to unity . In a matter-dominated cosmology with zero cosmological constant the evolution of Ω_m is approximated as $1 - (1 - \Omega_0)(1 + z)^{-1}$. Ω_m is even closer to unity in a universe with non-zero vacuum energy (cosmological constant).

Modern observational cosmology is based on the premise that the object observed on galactic scales and larger are the products of the evolution of primordial perturbations in an otherwise extremely homogenous early universe (Peebles 1993). The first ingredient in any galaxy formation recipe is the description of these fluctuations in mass density. They are usually assumed to be random and Gaussian-distributed with a power-spectrum described by a power-law over the range of mass scales of interest. After the mass and radiation fields decouple at a redshift of $z\sim1400$ density enhancements begin to grow under the influence of the corresponding gravitational potential.

A second ingredient is a model of the growth of these fluctuations: For the mass scales of interest here this evolution has extended well into the non-linear regime: galaxies and clusters of galaxies are $\sim 10^4$ and $\sim 10^2$ times denser than the mean matter background. An analytic treatment of the evolution of non-linear, gravitationally bound objects was attempted by Press & Schechter (Press & Schechter 1974), who introduced an ingenious description of the mass distribution of gravitationally-bound objects as they evolve to larger

and larger scales from an intitial mass perturbation spectrum. The fractional root-mean-square fluctuations in the mean matter density on the mass scale M are assumed to obey the scaling law

$$\left\langle \left(\frac{\delta M}{M} \right)^2 \right\rangle^{1/2} \sim M^{-\alpha}, \tag{A.1}$$

where the value of α is related to the index of the power spectrum of the initial density perturbations by $\alpha = (3+n)/6$. They found the number distribution of bound masses at a particular epoch to obey the law

$$n(M) = n_0 \left(\frac{M}{M^*} \right)^{-(2-\alpha)} e^{-\frac{1}{2}(M/M^*)^{2\alpha}} \tag{A.2}$$

[note that the α defined here is $1 - \alpha$ in Press & Schechter (1974)]. This distribution is essentially a power-law which is exponentially truncated at a characteristic mass M^*. In an Einstein-de Sitter universe with the matter density equal to the critical value ($\Omega_m = 1$) the value of M^* evolves with redshift as

$$M^* = M_0^*(1+z)^{1/\alpha} \tag{A.3}$$

The Press-Schechter description has been compared with more sophisticated analytical descriptions (Bond *et al.* 1991) and numerical n-body simulations and has held up remarkably well (Navarro *et al.* 1996).

The simplest model for an individual collapsed object is the spherical collapse model for dissipationless matter. The objects collapses and virializes until its mean density is a factor of $178\Omega^{-0.6}$ times the mean density at formation (for a flat universe) or $178\Omega^{-1}$ for an open universe. If $\Omega_m \sim 1$ and structure formation proceeds hierachically then objects will survive only on the order of a dynamical time before becoming part of a larger object and the mean density at formation is the density at that particular epoch, i.e. there are no "old" halos. The internal structure of the halo is taken to be an isothermal sphere with density profile $\rho \sim r^{-2}$. With these assumptions the relation between the circular velocity and mass of the halo is (White & Narayan 1987)

$$M \sim \frac{v_c^3}{9GH} \tag{A.4}$$

where H is the Hubble constant at the formation epoch. A primordial gas component (76% H and 24% He) in hydrostatic equilibrium with this potential well will have a temperature (nearly independent of Ω) of

$$T_{halo} \sim 4.4 \times 10^6 h^{2/3} (1+z) \left(\frac{M}{4 \times 10^{12} M_\odot} \right)^{2/3} K. \tag{A.5}$$

The dynamical time (also roughly the crossing time or collapse time) of a homogeneous sphere of density ρ is (Binney & Tremaine 1987),

$$t_d = \sqrt{\frac{3\pi}{16 G \rho}} \tag{A.6}$$

With the previous assumptions, the dynamical time in Gyr is

$$t_d \sim 0.18 \Omega^{-1/2} h^{-1} (1+z)^{-3/2} \tag{A.7}$$

The final ingredient to galaxy formation is the introduction of gas into the evolving potential wells such that it can eventually contract to a dense state and form stars. The physical processes associated with the gas will also introduce length scales into an otherwise nearly scale-free model. It was suggested that the particular mass scales of objects (globular clusters, galaxies, clusters) might arise from just such physics (Press & Schechter 1974). It was first pointed out by Peebles & Dicke (1968) that the typical mass of globular clusters, some of which appear to be the oldest objects in the universe, is close to the Jeans instability mass at the temperature at the epoch of decoupling ($\sim 10^{4 o}$K) where the matter was first able to move independently of the radiation field.

Several researchers (Binney 1977; Rees & Ostriker 1977; Silk 1977) independently developed as a basic criterion for galaxy formation the requirement that the cooling time scale of the gas must be shorter than the dynamical time of the object, allowing the gas to cool faster than the collapse of objects can heat it to the virial temperature. Its entropy reduced, the gas collapses to a dense state which promotes efficient star formation and a galaxy is born. White & Rees (1978) combined all three ingredients, proposing that a "dark" dissipationless matter component dominated the evolving gravitational potential on the mass scales of galaxies and collapsed into bound objects from an initially perturbed state. The dissipative (gas) component falls into the potential wells and is also influenced

by external (ionizing flux) and internal (star formation) heating sources while it is also able to radiate away energy. Galaxies form when the gas is able to radiate away a large amount of the gravitational energy and collapse to a very dense state to form stars. The resulting objects have undergone significant dissipation and are thus much less susceptible to further evolution by merging. This process essentially "freezes out" the structure at a particular epoch and makes it visible as the distribution of galaxies observed today, malgre some mild evolutionary effects. Subsequent work has been refinement of this basic picture.

The formation of luminous objects is first allowed after recombination at a redshift of $z \sim 1200$, although any non-baryonic "dark" matter ingredient could start forming structure earlier. Even at somewhat later epochs any ionized portion of the gas is strongly coupled to the cosmic radiation background and transfers a drag force to the bulk of the gas and prevents it from freely collapsing into the gravitational potentials of bound objects. The "Compton drag" force per unit volume on a gas with ion density ρ_i moving at velocity $\vec{v}$ is

$$\vec{F_T} = -\frac{16\rho_i \sigma_T \sigma_B T^4 \vec{v}}{3 m_p c^2}, \tag{A.8}$$

where the black-body temperature of the radiation field is $T = 2.731(1+z)$. The gravitational volume force experienced by the gas falling into a dark-matter halo is roughly,

$$\vec{F_T} = \rho v_c / t_d \tag{A.9}$$

where v_c is the circular velocity of the halo (which will be the mean free-fall speed of the gas) and t_d is the dynamical time. Equating these two expressions leads to an expression for the maximum redshift at which Compton drag permits baryonic matter to collapse into form collapse objects:

$$1 + z_c \sim 366 \Omega_B^{1/5} h^{2/5} f_i^{-1} \tag{A.10}$$

where f_i is the ionization fraction of the gas.

Once Compton drag disappears, the gas must be able to radiate away a significant amount of its binding energy in the dark-matter halo. The primary mechanisms by which gas cooled in the early universe are cooling by ions scattering cosmic background radiation photons (Compton cooling), ion-ion scattering (bremstrahllung), and recomination radiation. The ratio of self-radiation to Compton cooling for collapsed objects while $\Omega_m \sim 1$

is $3300(1+z)^{-1}\Omega_B h^2 T_6^{-1}$. For $\Omega_B = 0.05$ and $h = 0.7$ radiation cooling dominates below $z \sim 80$ in the formation of galaxy-sized objects.

In the temperature range of primary interest (10^4 to 10^5 K) the dominant cooling mechanism of primordial gas (76% H and 24% He) is radiation from collisionally excited partially ionized atoms (HI and HeII) (Fall & Rees 1985). Below 15000 K the cooling efficiency drops off precipitously as the gas rapidly becomes neutral. Thus luminous objects may not form unless the equivalent temperature of dark-matter halos exceeds $1.5 \times 10^{4\circ}$ K. The temperature of a dark-matter halo, independent of cosmology, is given by

$$T = 2.3 \times 10^6 (1+z) \left(\frac{L}{10^{10} L_\odot} \right)^{2/3} \tag{A.11}$$

where for convenience I have substituted luminosity L for mass, assuming a constant mass-to-light ratio of 50. Thus the smallest objects which can form at the end of the Compton drag-inhibited epoch have $L \sim 1000 L_\odot$.

If we live in an $\Omega = 1$ universe with spectral index n and if objects of luminosity $4 \times 10^{11} h^{-2} L_\odot$ are now reaching the non-linear phase of collapse then collapsing objects at redshift z will have luminosity

$$L = 4 \times 10^{11} (1+z)^{-6/(n+3)} \tag{A.12}$$

For $n \leq -1$ all objects forming after Compton drag becomes negligible have temperatures above $1.5 \times 10^{4\circ}$ K and are thus able to cool efficiently.

The ratio of the cooling time to the dynamical time for $T \sim 10^6$K is

$$\frac{t_c}{t_d} \sim 0.9 h^{-1/3} \Omega_B^{-1} \Omega^{1/2} (1+z)^{-1/2} \left(\frac{M}{4 \times 10^{12}} \right)^{2/3} \tag{A.13}$$

Equating this to unity, the maximum mass of a galaxy forming at redshift z is

$$M \sim 5 \times 10^{12} h^{1/2} \Omega_B \Omega^{-1/2} (1+z)^{3/4} M_\odot \tag{A.14}$$

which, for the usual choice of parameters and a formation redshift of 3, gives $1.3 \times 10^{12} M_\odot$. Thus only objects less massive than M_c will form galaxies, with

$$M_c \sim 3 \times 10^{11} (1+z)^{3/4} M_\odot \tag{A.15}$$

The critical halo temperature below which luminous objects can form is

$$T_* \sim 4.8 \times 10^6 \Omega_B \Omega^{-1/2} h (1+z)^{3/2} K \tag{A.16}$$

For $\Omega_B = 0.05$, $\Omega = 0.2$, and $h = 0.7$, bright galaxies $T \sim 2 \times 10^6$ K can form only to $z \sim 2$.

Galaxy formation is more efficient at higher redshift because of the higher densities leading to greater cooling. The objects forming at the present epoch (clusters of galaxies) have cooling times much larger than their dynamical times, and in most cases, comparable to the Hubble time.

Perhaps the simplest method of constructing a theoretical galaxy luminosity function while retaining some basic physics is one which combines the evolution of dark matter halos described by the Press-Schechter formalism with the requirement that $t_c < t_d$. Although the dark matter halos continue to grow in mass, the luminous components of the galaxies that form are assumed to resist further merging due to their more compact dynamical states. However, the ability of low mass objects to cool efficiently at high redshift would mean that most of the gas would reside in very low-mass objects forming as soon as Compton drag became small. This would mean that the characteristic mass would be of order $10^6 - 10^7 M_\odot$; i.e., objects intermediate those of globular clusters and galaxies. The characteristic sizes of galaxies at the present epoch are three to five orders of magnitude larger. This is sometimes called the "Cooling Catastrophe".

Four possible ways to save this simple picture of galaxy formation are (1) adopt a power spectrum index that is much steeper than the CDM value of -1 to form more massive halos at higher redshift; (2) allow the luminous material continued to merge within the dark matter halos under the influence of dynamical friction; (3) include the feedback effects of star formation on the gas such that gas is lost from the shallow potential wells of dwarf galaxies and they form inefficiently; or (4) that injection of entropy from an initial generation of stars prevented the gas from collapsing and cooling until the halos grew to a critical mass. I next address each of these avenues in order:

To form L_* objects at a redshift of 100, even in an open universe, would require a spectral index of at least $n = 3$, absolutely inconsistent with the available data on these scales; (White 1993) and references therein.

It is straight-forward to show that merging of luminous material would not have

been able to form $L*$ galaxies. The orbital decay time of globular clusters within the isothermal sphere ($\rho \sim r^{-2}$) potential of an idealized dark matter halo has been worked out by Tremaine (1976):

$$t_d \sim 0.9 \times 10^{10} \left(\frac{r_i}{2kpc}\right)^{3/2} \left(\frac{M}{10^{10} M_\odot}\right) \left(\frac{m}{10^6 M_\odot}\right)^{-1} yr, \tag{A.17}$$

where M is the mass of the galaxy, and m and r_i are the mass and initial orbital radius of the globular cluster. The merging time or dynamical time for the halo can be written in the same style:

$$t_m \sim 2.1 \times 10^7 \left(\frac{r_i}{2kpc}\right)^{3/2} \left(\frac{M}{10^{10} M_\odot}\right)^{-1/2} yr \tag{A.18}$$

For an $\Omega = 1$ CDM universe the redshift dependence of the dynamical friction time-scale is $(1+z)^{-9/2}$, while that of the halo merging time scale is $(1+z)^{-3/2}$. Thus at an early epoch globular cluster-mass objects could coallesce at a rate faster than the merging of halos could disrupt them, but eventually dynamical friction became very inefficient and galaxy formation by this mechanism halted. The halo mass scale at which this occurs is found by simply equation t_d and t_m to find

$$M_{crit} \sim 1.8 \times 10^8 M_\odot \left(\frac{m}{10^6 M_\odot}\right)^{2/3}. \tag{A.19}$$

Note that tidal stripping of the globular cluster will increase the orbital decay time and thus decrease the derived value of the critical mass.

White & Rees (1978) developed a model which includes the self-regulating effect of supernovae energy input during galaxy formation and supposes that the mass of gas turned into stars is proportional to the specific binding energy of the galaxy, which in turn is proportional to the circular velocity squared. With an appropriate adjustment of parameters, the mass of a typical galaxy can be produced by this model although the faint-end slope is found to be $(n-13)/(n+7)$, or -2 for CDM, steeper than observed.

An alternative model, developed by Blanchard *et. al.* (1992), which invokes similar physics postulates an injection of entropy into the IGM sufficient to prevent formation of luminous objects until the gas has cooled and dark matter halos grown large enough to gravitational trap it. Such an episode of "reheating" is consistent with the high level of ionization required to avoid the Gunn-Peterson effect and may have been produced by an

initial generation of stars (Population III). The gas would not fall into a potential well and form a galaxy until the condition $T_g < T_h$ was satisfied.

The ratio of Compton to radiation cooling in a uniform IGM at temperatures above $10^{6\circ}$K (where free-free emission dominates) is given by $0.2(1+z)h-2\Omega_B^{-1}\left(\frac{T_g}{4.4\times10^{6\circ}K}\right)^{1/2}$ and thus for reasonable values of the cosmological parameters, Compton cooling dominates to the present epoch. In a flat, $\Lambda = 0$ cosmology the ratio of the Compton cooling time to the Hubble time (at redshift z) is $120h(1+z)^{-5/2}$ and the IGM above a redshift of ~ 6 cools by Comptonization of CBR photons, while below this redshift it cools adiabatically. The redshift evolution of the temperature in the latter case (the only one of interest here as I shall show) is $\sim (1+z)^2$.

The velocity dispersion, expressed in terms of temperature scales as

$$T_c \sim (1+z)M^{2/3} \tag{A.20}$$

independent of the cosmology. Since the temperature of the IGM scales as $(1+z)^2$, the critical halo mass for galaxy formation would scale as $(1+z)^{3/2}$ At the epoch that galaxies can form in halos of mass M, the characteristic mass is $M_*(0)M^{-4/(n+3)}$. Convolving this with the result of Press & Schechter (1974), the result is mass distribution of the form;

$$n(M)dM \sim (M/M_*)M^{\frac{n-5}{6}}e^{-(M/M_*)^{\frac{n+7}{3}}} \tag{A.21}$$

Interestingly, an $n = -1$ choice of spectral index reproduces the flat luminosity function observed in field surveys. Furthermore, this model predicts that the most massive galaxies formed first. These would have the lowest specific angular momentum and would thus tend to be early-type, as is observed.

Sufficiently sensitive measurements of the spectrum of the cosmic microwave background (CMB) can be used to test the early heating theory (the late heating theory is more difficult to test since the gas is clumped and occupies a much smaller net solid angle.) The distortion of the CMB away from a perfect thermal spectrum by a hot IGM is given by the y parameter;

$$y = \int \frac{\sigma_T n_e c k T_e}{m_e c^2} dt. \tag{A.22}$$

If the IGM is heated to some initial temperature T_i at redshift z_i and cools adiabatically

thereafter until recombination at z_r then, for an Einstein-de Sitter Cosmology,

$$y \sim 3.4 \times 10^{-6} \Omega_B h \frac{T_i}{10^{6\circ} K} (1 + z_i)^{3/2} . \tag{A.23}$$

If L_* galaxies (with $T \sim 5 \times 10^{6\circ} K$) were able to form at a redshift z^* then, for the current limit of $y < 2.5 \times 10^{-5}$ (Wright *et al.* 1994), we have

$$1 + z_i < 1.1(1 + z^*)^{4/7} (\Omega_B h)^{-2/7}. \tag{A.24}$$

For $z^* = 3$, $\Omega_B = 0.05$, and $h = 0.7$, $z_i < 5.3$.

The most massive galaxies have an X-ray temperature of $\sim$ 1 keV. These could not have formed before a redshift of 5. The stringent limits placed on formation epochs in this scenario means that more precise measurements of the y parameter will prove to be a decisive test of the model.

Important here, there are two observational tests of these formation theories having to do with the galaxy luminosity function. The first is to measure the slope of the faint end of the luminosity function. A steep slope (e.g. $\alpha = -2$) would support the picture that dwarf galaxies formed first (albeit inefficiently) while a flat slope ($\alpha = -1$) would support a bright galaxy-first scenario. A second test would measure the dependence of the characteristic value of M^* on the local matter density. If bright galaxies formed later they would be systematically brighter in areas of high overdensity such as clusters of galaxies. Any correlation would be much weaker in a picture where the bright galaxies formed first.

Appendix B

Cluster Luminosity Functions

B.1 Photometric Luminosity Functions

Luminosity functions constructed from photometric observations of 24 Abell clusters. Points are completeness-corrected data binned in 1-magnitude bins. The curves are the best-fit Schechter functions with both M^* and α allowed to vary. Error bars are the Poisson noise.

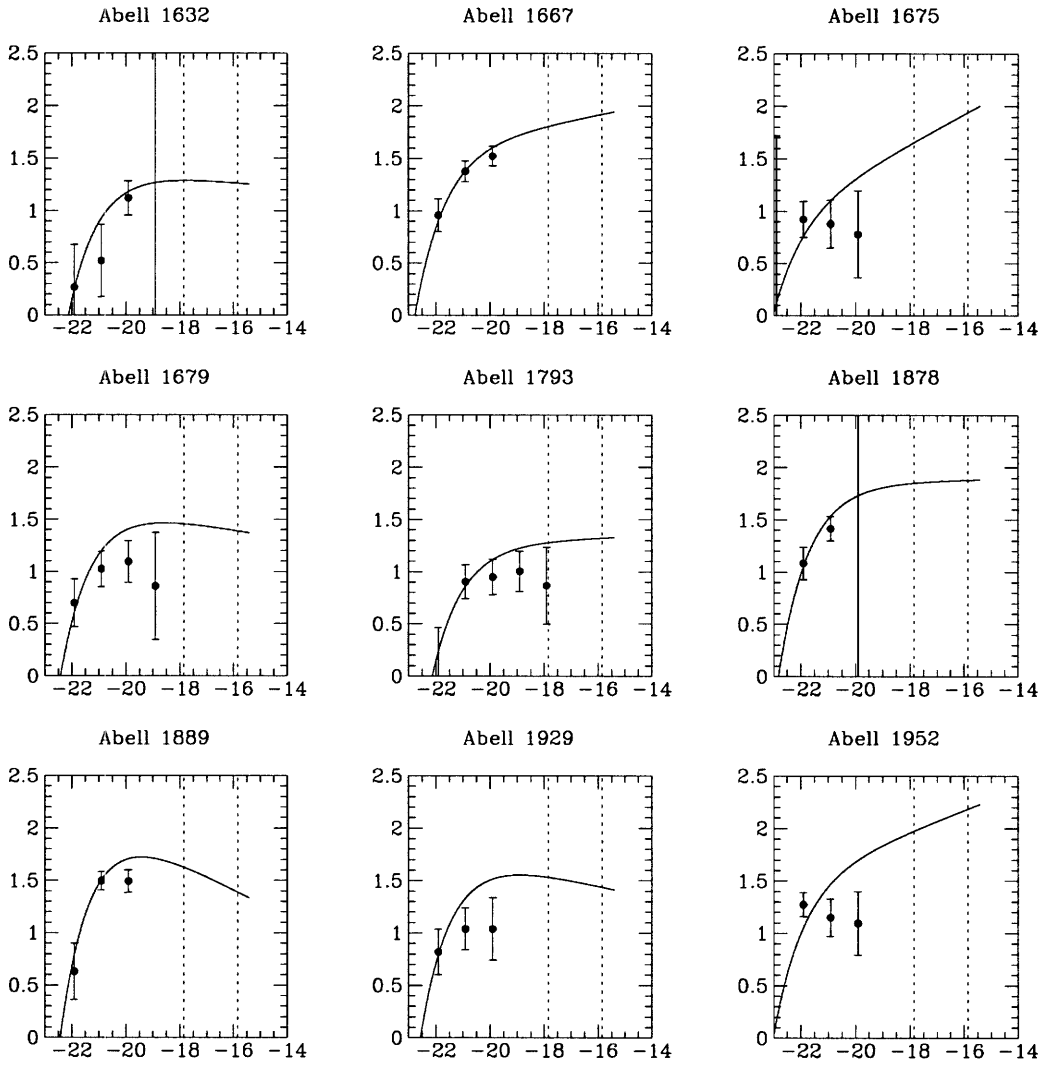
Abell 1632
Abell 1667
Abell 1675
Abell 1679
Abell 1793
Abell 1878
Abell 1889
Abell 1929
Abell 1952
2.5
2
1.5
1
0.5
0
−22 −20 −18 −16 −14

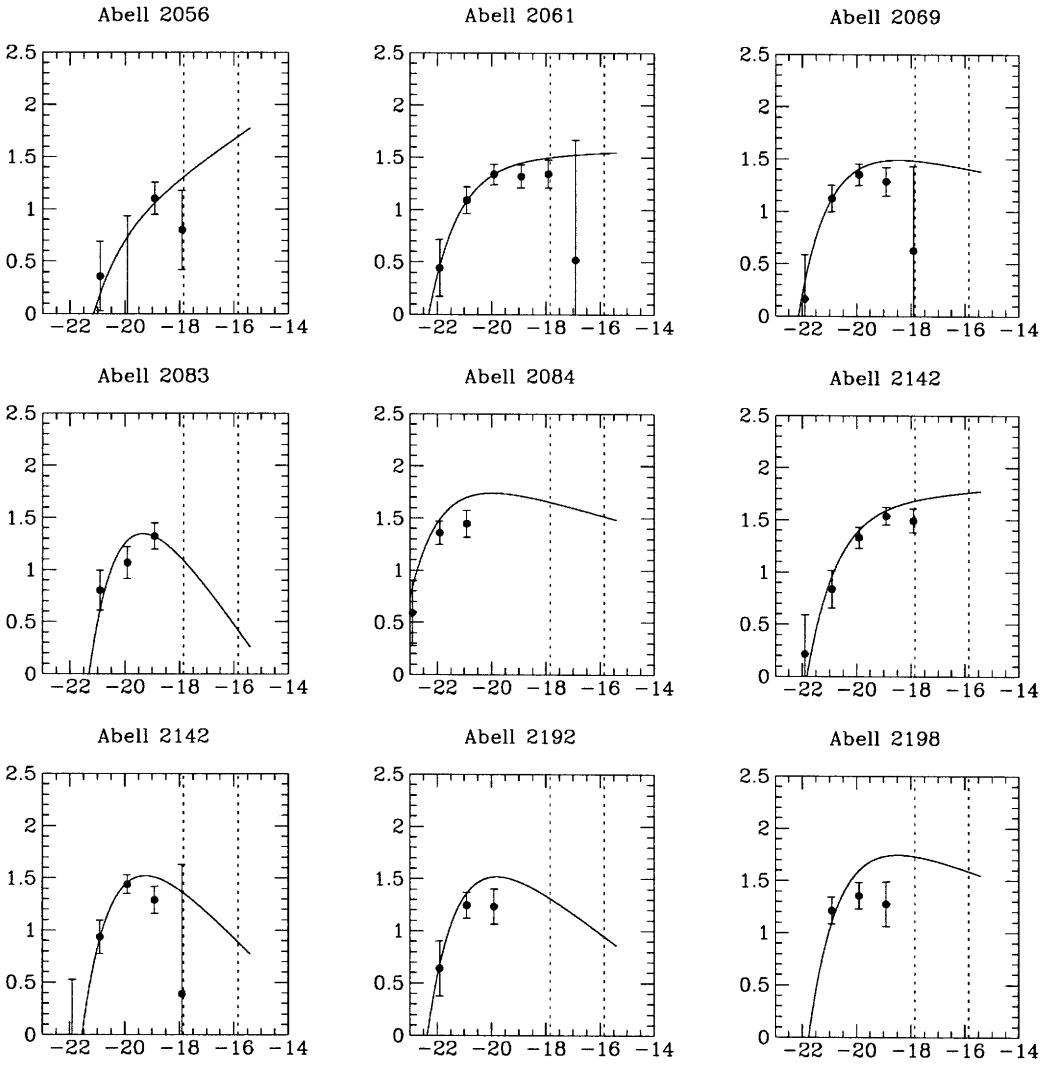
Abell 2056
Abell 2061
Abell 2069
Abell 2083
Abell 2084
Abell 2142
Abell 2142
Abell 2192
Abell 2198
2.5
2
1.5
1
0.5
0
−22 −20 −18 −16 −14

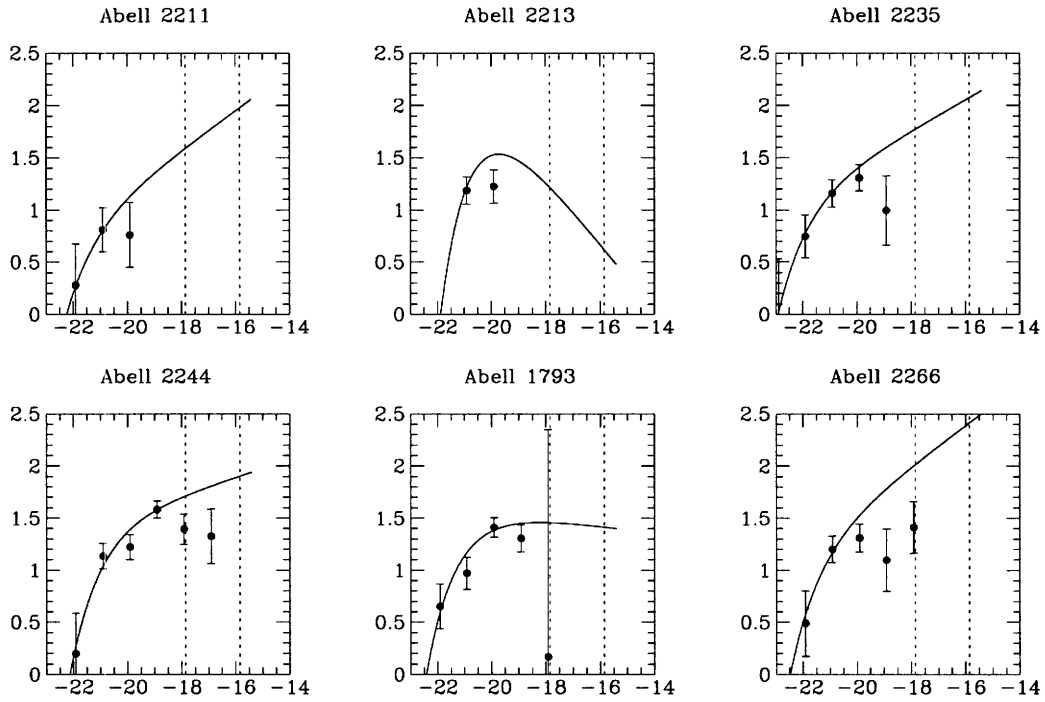
Abell 2211
Abell 2213
Abell 2235
Abell 2244
Abell 1793
Abell 2266
2.5
2
1.5
1
0.5
0
−22 −20 −18 −16 −14

B.2 Non-Photometric Luminosity Functions

Luminosity function of the 43 Abell clusters observed under non-photometric conitions. The histograms are the LFs constructed by separating galaxies inside and outside an aperture centered on the peak of the cluster surface brightness distribution. If the cluster is sufficiently distant, a radius of 0.5 h^{-1} Mpc is used; otherwise, the radius is decreased by 10% increments until the solid angle outside of the aperture is at least 1/3 of the solid angle inside.

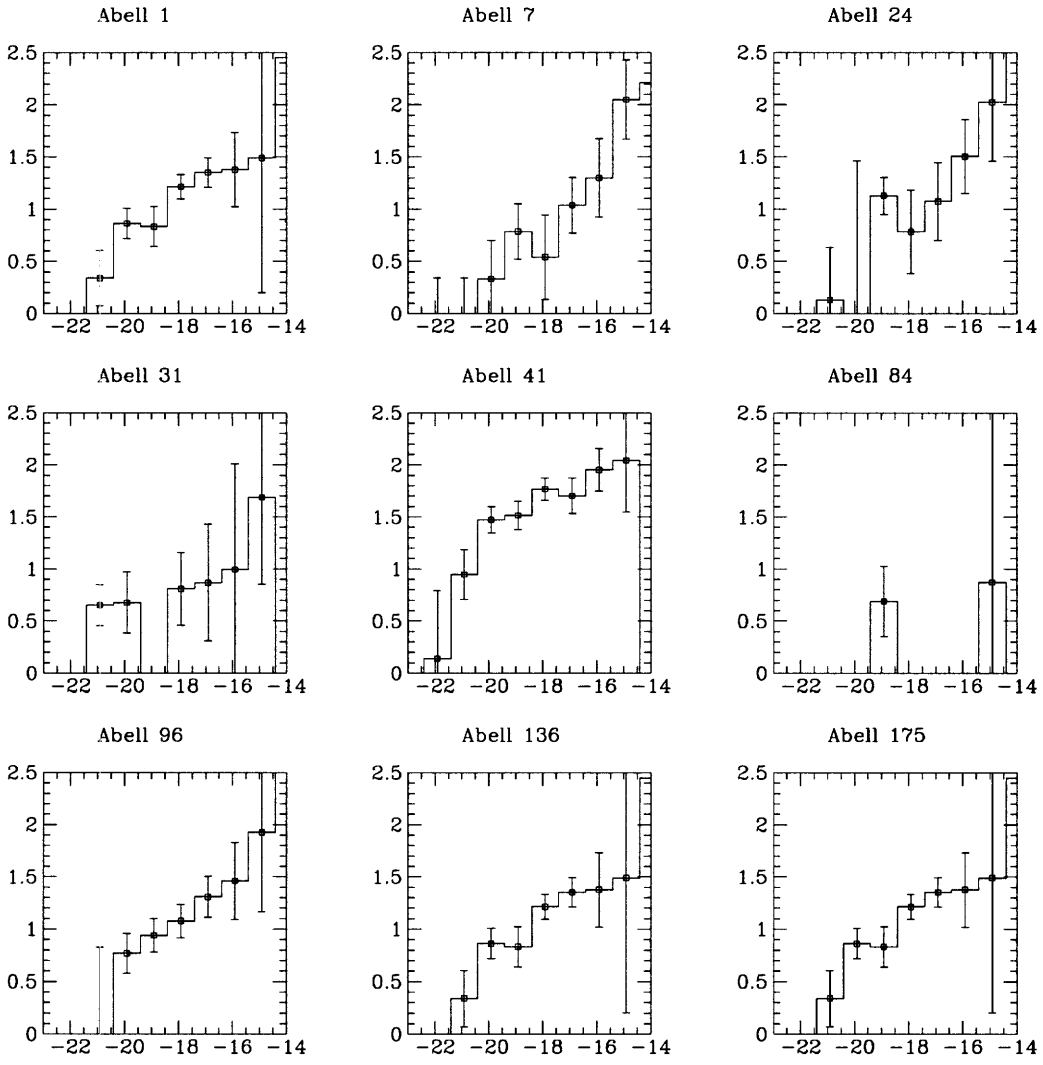
Abell 1
Abell 7
Abell 24
Abell 31
Abell 41
Abell 84
Abell 96
Abell 136
Abell 175
2.5
2
1.5
1
0.5
0
−22 −20 −18 −16 −14

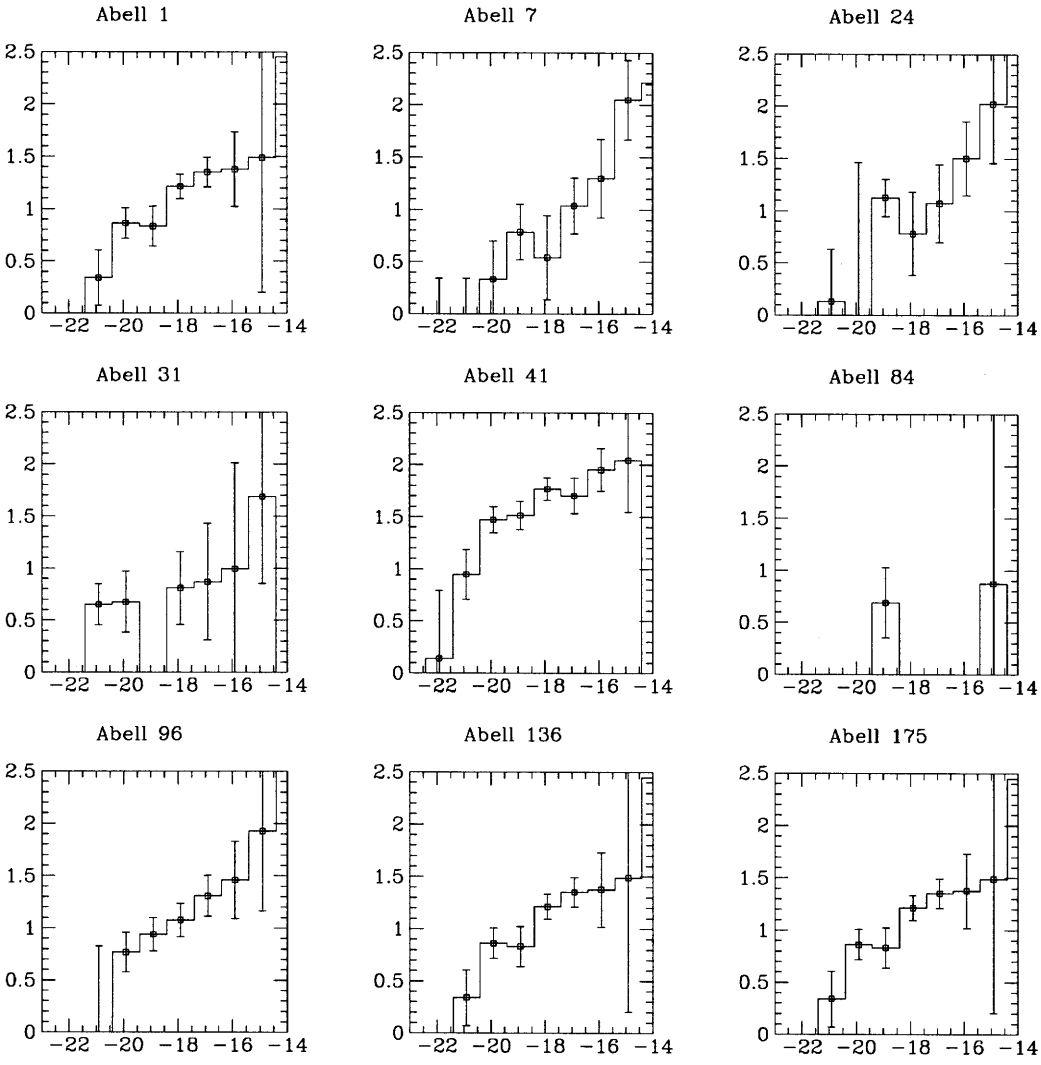
Abell 1
Abell 7
Abell 24
Abell 31
Abell 41
Abell 84
Abell 96
Abell 136
Abell 175
2.5
2
1.5
1
0.5
0
−22 −20 −18 −16 −14

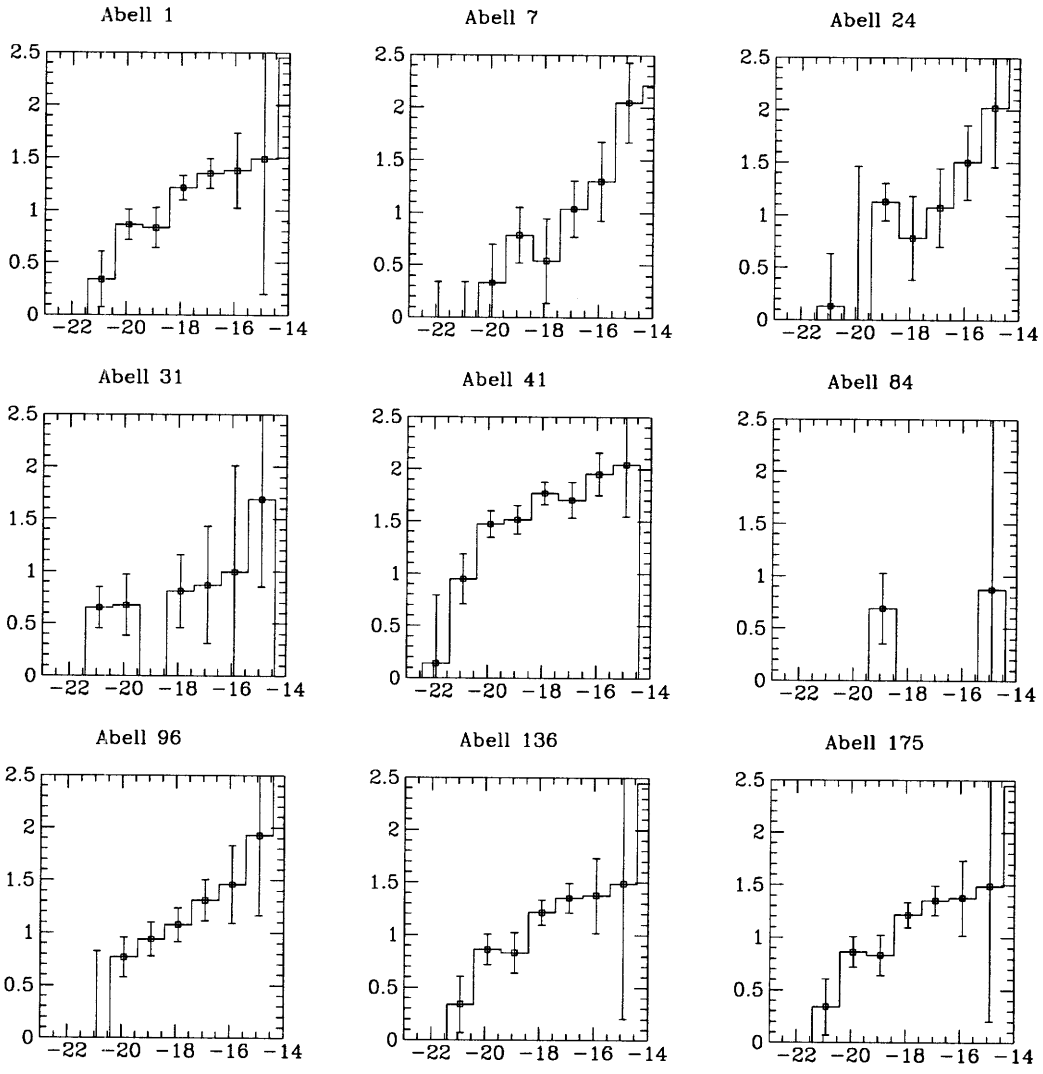
Abell 1
Abell 7
Abell 24
Abell 31
Abell 41
Abell 84
Abell 96
Abell 136
Abell 175
2.5
2
1.5
1
0.5
0
-22 -20 -18 -16 -14

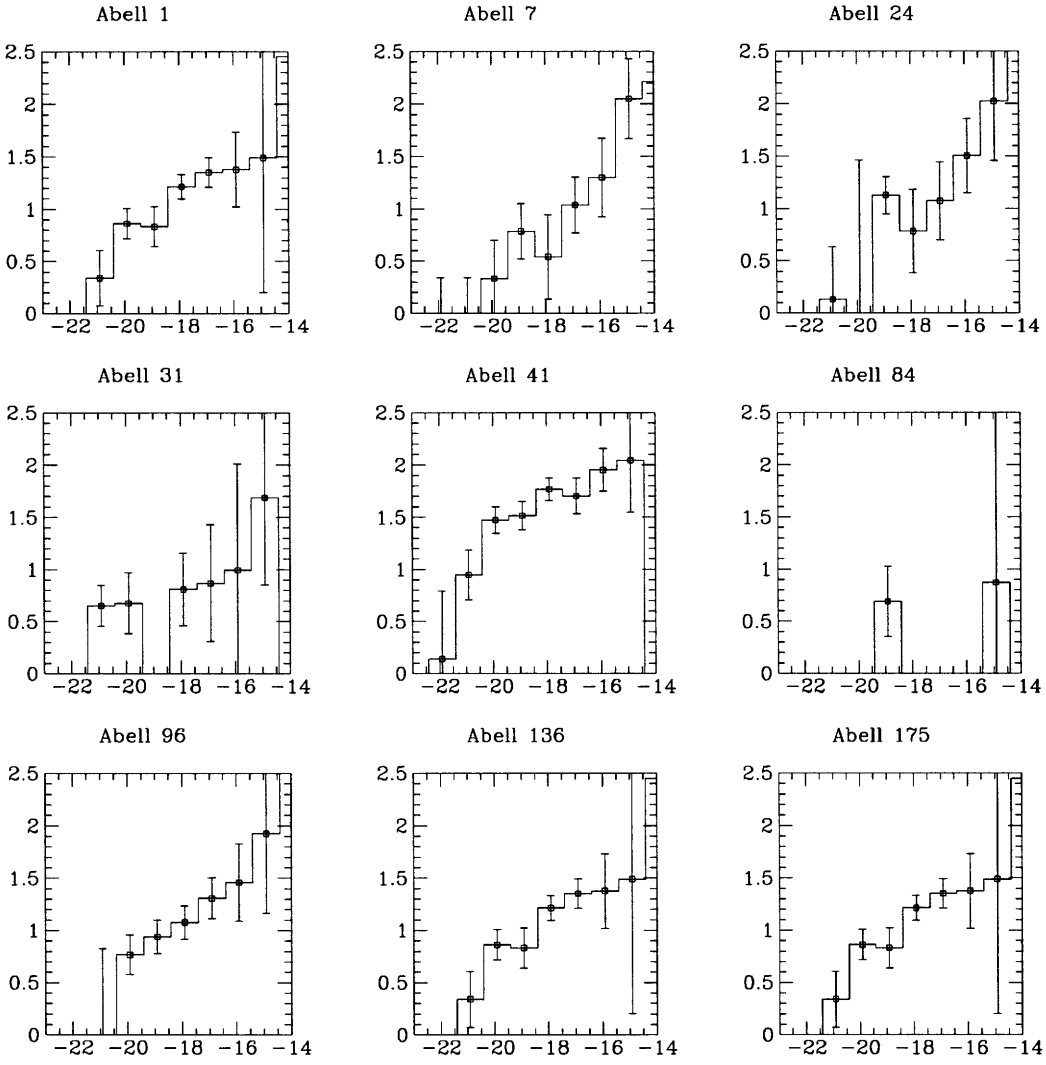
Abell 1
Abell 7
Abell 24
Abell 31
Abell 41
Abell 84
Abell 96
Abell 136
Abell 175
2.5
2
1.5
1
0.5
0
−22 −20 −18 −16 −14

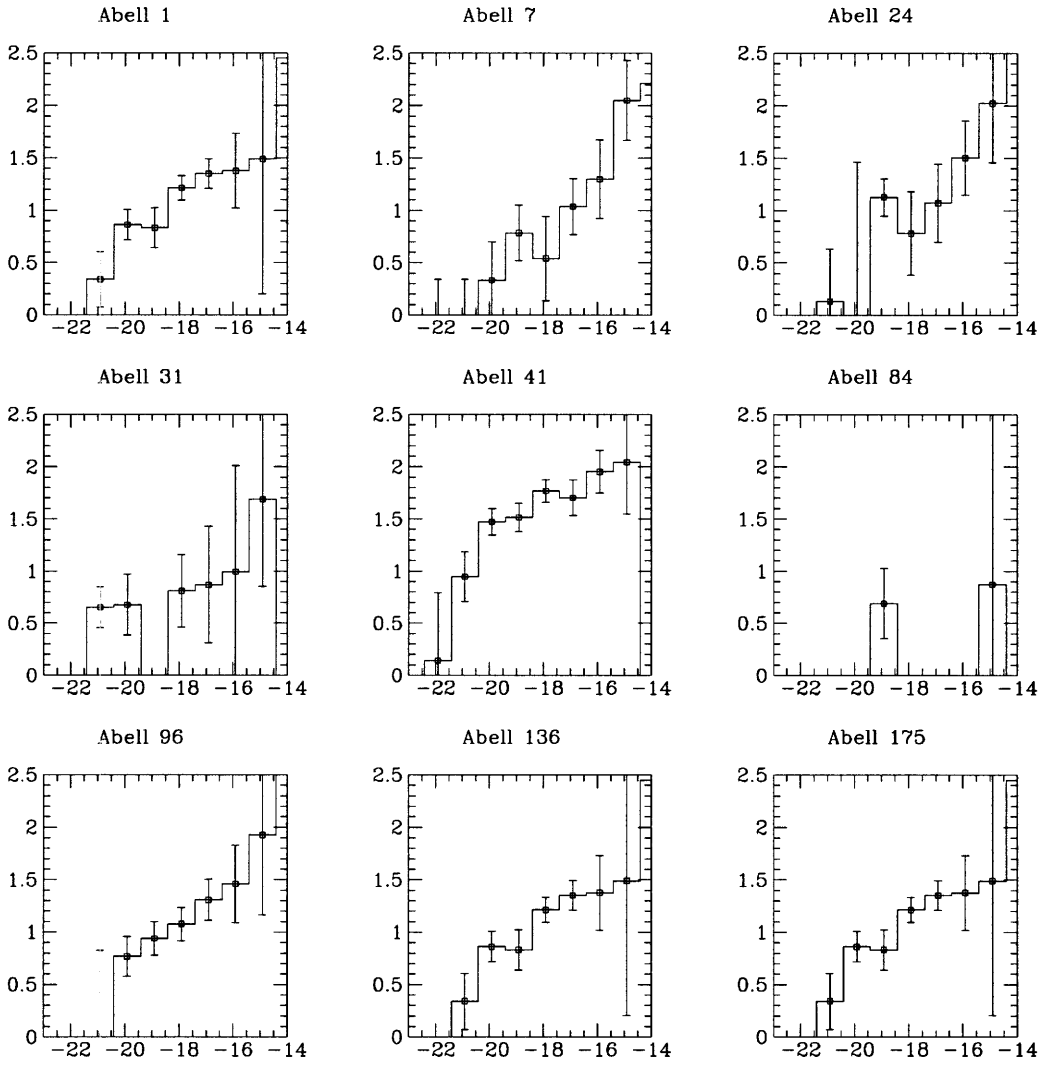
Abell 1
Abell 7
Abell 24
Abell 31
Abell 41
Abell 84
Abell 96
Abell 136
Abell 175
2.5
2
1.5
1
0.5
0
−22 −20 −18 −16 −14

Bibliography

Abell, G. O., 1958, *ApJS*, **3**, 211

Abell, G. O., 1962, in C. G. McVittie (ed.), *Problems in Extragalactic Research*, pp 232+, New York: MacMillan

Abell, G. O., Corwin, Harold G., J., & Olowin, R. P., 1989, *ApJS*, **70**, 1

Abraham, R. G., Valdes, F., Yee, H. K. C., & Van Den Bergh, S., 1994, *ApJ*, **432**, 75

Bahcall, J. N. & Soneira, R. M., 1981, *ApJS*, **47**, 357

Bahcall, N. A. & Cen, R., 1994, *ApJLett*, **426**, L15

Bardeen, J. M., Bond, J. R., Kaiser, N., & Szalay, A. S., 1986, *ApJ*, **304**, 15

Bautz, L. P. & Morgan, W. W., 1970, *ApJ*, **162**, L149

Beers, T. C. & Tonry, J. L., 1986, *ApJ*, **300**, 557

Bernstein, G. M., Nichol, R. C., Tyson, J. A., Ulmer, M. P., & Wittman, D., 1995, *AJ*, **110**, 1507+

Binney, J., 1977, *ApJ*, **215**, 483

Binney, J. & Tremaine, S., 1987, *Galactic Dynamics*, Princeton University Press

Biviano, A., Durret, F., Gerbal, D., Le Fevre, O., Lobo, C., Mazure, A., & Slezak, E., 1995, A&A **297**, 610+

Blanchard, A., Valls-Gabaud, D., & Mamon, G. A., 1992, A&A **264**, 365

Bolte, M., 1992, *PASP*,} **104**, 794

Bond, J. R., Kaiser, N., Cole, S., & Efstathiou, G., 1991, *ApJ*, **379**, 440

Buote, D. A. & Canizares, C. R., 1994, *ApJ*, **427**, 86

Buote, D. A. & Tsai, J. C., 1995, *ApJ*, **452**, 522+

Buote, D. A. & Tsai, J. C., 1996, *ApJ*, **458**, 27+

Burstein, D. & Heiles, C., 1982, *AJ*, **87**, 1165

Burstein, D. & Heiles, C., 1984, *ApJS*, **54**, 33

Butcher, H. & Oemler, A., J., 1984, *ApJ*, **285**, 426

Buzzoni, A., 1989, *ApJS*, **71**, 817

Buzzoni, A., 1995, *ApJS*, **98**, 69+

Buzzoni, A., Chincarini, G., & Molinari, E., 1993, *ApJ*, **410**, 499

Canizares, C. R., 1990, *Advances in Space Research* **10**, 261

Casertano, S., Ratnatunga, K. U., Griffiths, R. E., Im, M., Neuschaefer, L. W., Ostrander, E. J., & Windhorst, R. A., 1995, *ApJ*, **453**, 599+

Castander, F. J., Ellis, R. S., Frenk, C. S., Dressler, A., & Gunn, J. E., 1994, *ApJLett*, **424**, L79

Cavaliere, A. & Fusco-Femiano, R., 1976, A&A **49**, 137

Chiboucas, K., Mateo, M., & Schombert, J. M., 1995, *BAAS*, **187**, 1111+

Christian, C. A., Adams, M., Barnes, J. V., Hayes, D. S., Siegel, M., Butcher, H., & Mould, J. R., 1985, *PASP*,} **97**, 363

Coles, P. & Ellis, G., 1994, *Nature* **370**, 609

Colless, M., Ellis, R. S., Taylor, K., & Hook, R. N., 1990, *MNRAS*, **244**, 408

Da Costa, L. N., Geller, M. J., Pellegrini, P. S., Latham, D. W., Fairall, A. P., Marzke, R. O., Willmer, C. N. A., Huchra, J. P., Calderon, J. H., Ramella, M., & Kurtz, M. J., 1994, *ApJLett*, **424**, L1

Dalton, G. B., Efstathiou, G., Maddox, S. J., & Sutherland, W. J., 1994, *MNRAS*, **269**, 151

De Lapparent, V., Geller, M. J., & Huchra, J. P., 1991, *ApJ*, **369**, 273

De Propris, R., Pritchet, C. J., Harris, W. E., & McClure, R. D., 1995, *ApJ*, **450**, 534+

Dekel, A., Bertschinger, E., Yahil, A., Strauss, M. A., Davis, M., & Huchra, J. P., 1993, *ApJ*, **412**, 1

Doi, M., Fukugita, M., & Okamura, S., 1993, *MNRAS*, **264**, 832

Doi, M., Fukugita, M., & Okamura, S., 1995, *ApJS*, **97**, 59

Dressler, A., 1978a, *ApJ*, **222**, 23

Dressler, A., 1978b, *ApJ*, **223**, 765

Dressler, A., 1980, *ApJ*, **236**, 351

Dressler, A. & Gunn, J. E., 1983, *ApJ*, **270**, 7

Dressler, A. & Gunn, J. E., 1992, *ApJS*, **78**, 1

Dressler, A., Gunn, J. E., & Schneider, D. P., 1985, *ApJ*, **294**, 70

Dressler, A., Oemler, Augustus, J., Butcher, H. R., & Gunn, J. E., 1994, *ApJ*, **430**, 107

Driver, S. P. & Phillips, S., 1996, *XXX preprint astro-ph/9603113*

Driver, S. P., Phillips, S., Davies, J. I., Morgan, I., & Disney, M. J., 1994, *MNRAS*, **268**, 393

Eales, S., 1993, *ApJ*, **404**, 51

Ebeling, H., 1993, *Ph.D. thesis*, Ludwig-Maximilians-Universitat-Munchen

Ebeling, H., Allen, S. W., Crawford, C. S., C., E. A., Fabian, A. C., Bohringer, H., Voges, W., & P., H. J., 1996, *XXX preprint astro-ph/9512104*

Ebeling, H., Mendes De Oliveira, C., & White, D. A., 1995, *MNRAS*, **277**, 1006

Ebeling, H., Voges, W., Bohringer, H., & Edge, A. C., 1993, *Astronomy & Astrophysics* **275**, 360

Edge, A. C., Stewart, G. C., Fabian, A. C., & Arnaud, K. A., 1990, *MNRAS*, **245**, 559+

Efstathiou, G., Bernstein, G., Tyson, J. A., Katz, N., & Guhathakurta, P., 1991, *ApJLett*, **380**, L47

Efstathiou, G., Ellis, R. S., & Peterson, B. A., 1988, *MNRAS*, **232**, 431

Eke, V. R., Cole, S., & Frenk, C. S., 1996, *MNRAS*, , *submitted*

Ellis, R. S., Colless, M., Broadhurt, T., Heyl, J., & Glazebrook, K., 1995, *XXX Preprint astro-ph/9512057*

Evrard, A. E. & Henry, J. P., 1991, *ApJ*, **383**, 95

Faber, S. M. & Jackson, R. E., 1976, *ApJ*, **204**, 668

Fabian, A. C., Nulsen, P. E. J., & Canizares, C. R., 1991, A&A Rev. **2**, 191

Fall, S. M. & Rees, M. J., 1985, *ApJ*, **298**, 18

Ferguson, H. C. & Binggeli, B., 1994, A&A Rev. **6**, 67

Ferguson, H. C. & Sandage, A., 1988, *AJ*, **96**, 1520

Freeman, K. C., 1970, *ApJLett*, **160**, 811+

Giavalisco, M., Steidel, C. C., & Szalay, A. S., 1994, *ApJLett*, **425**, L5

Gioia, I. M. & Luppino, G. A., 1994, *ApJS*, **94**, 583

Gioia, I. M., Maccacaro, T., Schild, R. E., Wolter, A., Stocke, J. T., Morris, S. L., & Henry, J. P., 1990, *ApJS*, **72**, 567

Glazebrook, K., Ellis, R., Colless, M., Broadhurst, T., Allington-Smith, J., & Tanvir, N., 1995, *MNRAS*, **273**, 157

Gronwall, C. & Koo, D. C., 1995, *ApJLett*, **440**, L1

Gunn, J. E., Hoessel, J. G., & Oke, J. B., 1986, *ApJ*, **306**, 30

Gunn, J. E. & Tinsley, B. M., 1976, *ApJ*, **210**, 1

Guth, A. H. & Pi, S. Y., 1982, *Physical Review Letters* **49**, 1110

Hamilton, T. T. & Helfand, D. J., 1993, *ApJ*, **418**, 55+

Hamilton, T. T., Helfand, D. J., & Wu, X., 1991, *ApJ*, **379**, 576

Han, M., 1995, *ApJ*, **442**, 504

Hausman, M. A. & Ostriker, J. P., 1978, *ApJ*, **224**, 320

Henry, J. P., Briel, U., Gunn, J. E., & Soltan, A., 1982, *ApJ*, **262**, 1

Henry, J. P., Gioia, I. M., Maccacaro, T., Morris, S. L., Stocke, J. T., & Wolter, A., 1992, *ApJ*, **386**, 408

Hickson, P., Auman, J. R., & Kindl, E., 1989, *ApJS*, **70**, 687

Hoessel, J. G. & Schneider, D. P., 1985, *AJ*, **90**, 1648

Hubble, E., 1936, *ApJ*, **84**, 158

Humason, M. L., Mayall, N. U., & Sandage, A. R., 1956, *AJ*, **61**, 97

Jedrzejewski, R. I., 1987, *MNRAS*, **226**, 747

Jones, C. & Forman, W., 1984, *ApJ*, **276**, 38

Jones, L. R., Fong, R., Shanks, T., Ellis, R. S., & Peterson, B. A., 1991, *MNRAS*, **249**, 481

Jones, L. R., Scharf, C. A., Perlman, E., Ebeling, H., Wegner, G., & Malkan, M., 1996, *XXX preprint astro-ph/9512041*

Jorgensen, I., 1994, *PASP*,} **106**, 967

Kaiser, N., 1991, *ApJ*, **383**, 104

Kashikawa, N., Shimasaku, K., Yagi, M., Yasuda, N., Doi, M., Okamura, S., & Sekiguchi, M., 1995, *ApJLett*, **452**, L99

Kellogg, E. M., 1973, in H. Bradt & R. Giacconi (eds.), *X- and Gamma-Ray Astronomy*, No. 55 in IAU, pp 171–183, D. Rediel Publishing Co., Dordrecht

Kent, S. M., 1985, *PASP*,} **97**, 165

Kirshner, R. P., Oemler, A., J., & Schechter, P. L., 1979, *AJ*, **84**, 951

Koo, D. C., Gronwall, C., & Bruzual A., G., 1993, *ApJLett*, **415**, L21

Koo, D. C. & Kron, R. G., 1992, ARA&A **30**, 613

Lahav, O., Fabian, A. C., Edge, A. C., & Putney, A., 1989, *MNRAS*, **238**, 881

Lang, K. R., 1980, *Astrophysical Formulae*, Springer-Verlag

Lauer, T. R. & Postman, M., 1994, *ApJ*, **425**, 418

Le Fevre, O., Crampton, D., Hammer, F., Lilly, S. J., & Tresse, L., 1994, *ApJLett*, **423**, L89

Lin, H., Kirshner, R. P., Shectman, S. A., D., L. S., Oemler, A., Tucker, D. L., & Schechter, P. L., 1996, *accepted by ApJ*, 464

Little, B. & Tremaine, S., 1987, *ApJ*, **320**, 493

Loveday, J., Peterson, B. A., Efstathiou, G., & Maddox, S. J., 1992, *ApJ*, **390**, 338

Lugger, P. M., 1986, *ApJ*, **303**, 535

Lumsden, S. L., Nichol, R. C., Collins, C. A., & Guzzo, L., 1992, *MNRAS*, **258**, 1

Malumuth, E. M. & Richstone, D. O., 1984, *ApJ*, **276**, 413

Marzke, R. O., Huchra, J. P., & Geller, M. J., 1994, *ApJ*, **428**, 43

Mathieu, R. D. & Spinrad, H., 1981, *ApJ*, **251**, 485

McGaugh, S. S., Bothun, G. D., & Schombert, J. M., 1995, *AJ*, **110**, 573+

Meekins, J. F., Fritz, G., Chubb, T. A., Friedman, H., & Henry, R. C., 1971, *Nature* **231(5298)**, 107

Merritt, D., 1985, *ApJ*, **289**, 18

Metcalfe, N., Shanks, T., Fong, R., & Jones, L. R., 1991, *MNRAS*, **249**, 498

Mihalas, D. & Binney, J., 1981, in *San Francisco, CA, W. H. Freeman and Co., 1981. 608 p.*

Mohr, J., Geller, M., Fabricant, D., Wegner, G., Thorstensen, J., & Richston, D., 1996, *XXX preprint astro-ph/9604169*

Mohr, J. J., Evrard, A. E., Fabricant, D. G., & Geller, M. J., 1995, *ApJ*, **447**, 8+

Molinari, E., Banzi, M., Buzzoni, A., Chincarini, G., & Pedrana, M. D., 1994, *Astronomy and Astrophysics Supplement Series* **103**, 245

Molinari, E., Buzzoni, A., & Chincarini, G., 1990, *MNRAS*, **246**, 576+

Moore, B., Katz, N., Lake, G., Dressler, A., & Oemler, A., J., 1996, *Nat*, **379**, 613

Moran, E. C., Helfand, D. J., Becker, R. H., & White, R. L., 1996, *ApJ*, **461**, 127+

Mottmann, J. & Abell, G. O., 1977, *ApJ*, **218**, 53

Navarro, J. F., Frenk, C. S., & White, S. D. M., 1996, *ApJ*, **462**, 563+

O'Connell, R. W., 1987, in *Starbursts and galaxy evolution; Proceedings of the Twenty-second Moriond Astrophysics Meeting, Les Arcs, France, Mar. 8-15, 1987 (A89-10001 01-90). Gif-sur-Yvette, France, Editions Frontieres, 1987, p. 367-379.*, pp 367–379

Odewahn, S. C., 1995, *PASP,}* **107**, 770+

Oegerle, W. R. & Hoessel, J. G., 1989, *AJ*, **98**, 1523

Oemler, A., 1974, *ApJ*, **194**, 1

Okamura, S., Kodaira, K., & Watanabe, M., 1984, *ApJ*, **280**, 7

Ostriker, J. P. & Hausman, M. A., 1977, *ApJLett*, **217**, L125

Ostriker, J. P., Peebles, P. J. E., & Yahil, A., 1974, *ApJLett*, **193**, L1

Pahre, M. A., Djorgovski, S. G., & De Carvalho, R. R., 1996, *ApJLett*, **456**, L79

Peebles, P. & Dicke, R., 1968, *ApJ*, **154**, 891

Peebles, P. J. E., 1993, *Principles of Physical Cosmology*, Princeton University Press

Pesce, J. E., Fabian, A. C., Edge, A. C., & Johnstone, R. M., 1990, *MNRAS*, **244**, 58

Peterson, B. A., Ellis, R. S., Kibblewhite, E. J., Bridgeland, M. T., Hooley, T., & Horne, D., 1979, *ApJLett*, **233**, L109

Peterson, B. A., Ellis, R. S., Shanks, T., Bean, A. J., & Efstathiou, G., 1986, *MNRAS*, **221**, 233

Pinkney, J., Roettiger, K., Burns, J. O., & Bird, C. M., 1996, *ApJS*, **104**, 1

Plionis, M., Barrow, J. D., & Frenk, C. S., 1991, *MNRAS*, **249**, 662

Postman, M. & Lauer, T. R., 1995, *ApJ*, **440**, 28

Postman, M., Lubin, L. M., Gunn, J. E., Oke, J. B., Hoessel, J. G., Schneider, D. P., & Christensen, J. A., 1996, *AJ*, **111**, 615+

Predehl, P. & Klose, S., 1996, A&A **306**, 283+

Press, W. J. & Schechter, P. L., 1974, *ApJ*, **187**, 425

Rakos, K. D. & Schombert, J. M., 1995, *ApJ*, **439**, 47

Rees, M. J. & Ostriker, J. P., 1977, *MNRAS*, **179**, 541

Rhee, G., Van Haarlem, M., & Katgert, P., 1992, *AJ*, **103**, 1721

Richstone, D., Loeb, A., & Turner, E. L., 1992, *ApJ*, **393**, 477

Rood, J. R. & Sastry, G. N., 1971, *PASP,}* **83**, 313

Rosati, P., Della Ceca, R., Burg, R., Norman, C., & Giacconi, R., 1995, *ApJLett*, **445**, L11

Rubin, V. C., Thonnard, N., & Ford, W. K., J., 1978, *ApJLett*, **225**, L107

Sandage, A., Tammann, G. A., & Yahil, A., 1979, *ApJ*, **232**, 352

Santiago, B. X., Strauss, M. A., Lahav, O., Davis, M., Dressler, A., & Huchra, J. P., 1996, *ApJ*, **461**, 38+

Schechter, P., 1976, *ApJ*, **203**, 297

Schechter, P. L. & Dressler, A., 1987, *AJ*, **94**, 563

Schneider, D. P., Hoessel, J. G., & Gunn, J. E., 1983a, *ApJ*, **264**, 337

Schneider, D. P., Hoessel, J. G., & Schneider, D. P., 1983b, *ApJ*, **268**, 476

Schombert, J. M., 1984, *Ph.D. thesis*, Yale Univ., New Haven, CT.

Schombert, J. M., 1988, *ApJ*, **328**, 475

Schombert, J. M. & Bothun, G. D., 1987, *AJ*, **93**, 60

Scully, S. T. & Olive, K. A., 1995, *ApJ*, **446**, 272+

Shectman, S. A., 1985, *ApJS*, **57**, 77

Silk, J., 1977, *ApJ*, **211**, 638

Smail, I., Hogg, D. W., Yan, L., & Cohen, J. G., 1995, *ApJLett*, **449**, L105

Soltan, A. & Henry, J. P., 1983, *ApJ*, **271**, 442

Stanford, S. A., Eisenhardt, P. R. M., & Dickinson, M., 1995, *ApJ*, **450**, 512+

Stark, A. A., Gammie, C. F., Wilson, R. W., Bally, J., Linke, R. A., Heiles, C., & Hurwitz, M., 1992, *ApJS*, **79**, 77

Steidel, C. C., Dickinson, M., & Persson, S. E., 1994, *ApJLett*, **437**, L75

Steidel, C. C., Giavalisco, M., Pettini, M., Dickinson, M., & Adelberger, K. L., 1996, *ApJLett*, **462**, L17

Steidel, C. C. & Hamilton, D., 1993, *AJ*, **105**, 2017

Steidel, C. C. & Sargent, W. L. W., 1990, *AJ*, **99**, 1693

Stocke, J. T., Morris, S. L., Gioia, I. M., Maccacaro, T., Schild, R., Wolter, A., Fleming, T. A., & Henry, J. P., 1991, *ApJS*, **76**, 813

Struble, M. F. & Rood, H. J., 1991, *ApJS*, **77**, 363

Thronson, Harley A., J. & Shull, J. M., 1992

Tinsley, B. M. & Gunn, J. E., 1976, *ApJ*, **203**, 52

Tonry, J. L., 1987, *IAU Symposium* **127**, 89

Tremaine, S. D., 1976, *ApJ*, **203**, 345

Trevese, D., Crimele, G., & Appodia, B., 1996, *XXX preprint astro-ph/9603102*

Treyer, M. A. & Silk, J., 1994, *ApJLett*, **436**, L143

Trimble, V., 1987, ARA&A **25**, 425

Tucker, W. H., Tananbaum, H., & Remillard, R. A., 1995, *ApJ*, **444**, 532

Tully, R. B., 1988, *AJ*, **96**, 73

Tully, R. B. & Fisher, J. R., 1977, A&A **54**, 661

Tyson, J. A., 1988, *AJ*, **96**, 1

Voges, W., 1992, in *ESA, Space Sciences with Particular Emphasis on High-Energy Astrophysics p 9-19 (SEE N93-23878 08-88)*, pp 9–19

Watanabe, M., Kodaira, K., & Okamura, S., 1985, *ApJ*, **292**, 72

Weir, N., Djorgovski, S., & Fayyad, U. M., 1995, *AJ*, **110**, 1+

West, M. J., Jones, C., & Forman, W., 1995, *ApJLett*, **451**, L5

White, S. D. M., 1993, in *Les Houches Summer School in Astrophysics*

White, S. D. M. & Narayan, R., 1987, *MNRAS*, **229**, 103

White, S. D. M. & Rees, M. J., 1978, *MNRAS*, **183**, 341

Whitmore, B. C., Gilmore, D. M., & Jones, C., 1993, *ApJ*, **407**, 489

Williams, R., Dickinson, M., Giavalisco, M., Gilliland, R., Ferguson, H., Fruchter, A., McElroy, D., Lucas, R., Petro, L., & Postman, M., 1995, *BAAS*, **187**, 0903+

Wright, E. L., Mather, J. C., Fixsen, D. J., Kogut, A., Shafer, R. A., Bennett, C. L., Boggess, N. W., Cheng, E. S., Silverberg, R. F., Smoot, G. F., & Weiss, R., 1994, *ApJ*, **420**, 450

Zwicky, F., 1933, *Helv. Physc. Act.* **6**, 110+